Edwards, Graeme (2013) *Computational framework for fracture in heterogeneous materials.* PhD thesis.

http://theses.gla.ac.uk/4690/

Copyright and moral rights for this thesis are retained by the author

A copy can be downloaded for personal non-commercial research or study, without prior permission or charge

This thesis cannot be reproduced or quoted extensively from without first obtaining permission in writing from the Author

The content must not be changed in any way or sold commercially in any format or medium without the formal permission of the Author

When referring to this work, full bibliographic details including the author, title, awarding institution and date of the thesis must be given

Glasgow Theses Service
http://theses.gla.ac.uk/
theses@gla.ac.uk

Computational Framework for Fracture in Heterogeneous Materials

Graeme Edwards
MEng

Infrastructure & Environment Research Division
School of Engineering

University of Glasgow

Submitted in fulfilment of the requirements for the Degree of Doctor of Philosophy

August 2013

Declaration

I declare that this thesis is a record of the original work carried out by myself under the supervision of Professor Chris Pearce and Doctor Lukasz Kaczmarczyk in the Infrastructure & Environment Division of the School of Engineering at the University of Glasgow, United Kingdom. This research was undertaken during the period of October 2009 to August 2013. The copyright of this thesis belongs to the author under the terms of the United Kingdom Copyright acts. Due acknowledgment must always be made of the use of any material contained in, or derived from, this thesis. The thesis has not been presented elsewhere in consideration for a higher degree.

Graeme Edwards

Abstract

There has always been an ambition from Structural Engineers to design structures which are as efficient as possible, yet meet current design requirements. In the modern era, this process has relied heavily on the use of computational packages to carry out detailed analyses. However, for the design requirements to be met, the materials being used must be accurately understood and their behaviour must be accurately captured. In materials such as concrete, this understanding can be obtained by carrying out detailed analyses of the material at the mesoscale. At this scale, capturing the behaviour of concrete can be accomplished by recognising three distinct phases. First, the heterogeneities themselves, which are stiff particles usually made of crushed rock; second, we have the cement matrix which surrounds the heterogeneities and third, we have the weak interfacial transition zone (ITZ) between the two. By accurately describing the behaviour and interaction of these three phases, the complex behaviour of concrete can be captured.

This thesis brings together several novel contributions in order to create a computational modelling framework for modelling fracture in concrete at the mesoscale in three dimensions. All cracks are discrete in nature and restricted to element interfaces. As fracture can generally be considered to be a stress driven problem, an accurate description of the stress state in the model is essential. To achieve this, hybrid-Trefftz stress elements are used for the bulk elements in the mesh. The hybrid-Trefftz stress elements are characterised by their separate approximations of the stresses over the element domain and the displacements over the element boundary, allowing for a much higher order of approximation for the stresses to be utilised. The discrete cracks are modelled using continuous interface elements to allow the non-linear behaviour of concrete to be captured. The initiation and evolution of cracks was modelled using a plasticity model for the interface elements. This model followed the work of Winnicki and its implementation is presented in this thesis.

Unlike the conventional method of using interface elements, where they are present in the

mesh from the start of the analysis, in this work, interface elements are inserted dynamically as and when the material yield criterion is violated. A crack insertion methodology is presented for the inclusion of discrete cracks along element boundaries in 3D. The procedure takes advantage of properties of the hybrid-Trefftz stress elements to aid in its implementation. In particular, due to displacement continuity being enforced in the weak sense, faces of the same tetrahedron can be considered to be independent from each other but still produce statically admissible results. Results are presented showing that this methodology works well for different topological scenarios.

To generate an accurate geometric representation of the mesostructure, a method called the Maximum Level Set method was developed. For a given geometry, this method generated the mesostructure by placing aggregates within the domain at a maximum distance from both the boundary of the specimen and existing particles in a sequential manner. A Level Set function is used to calculate these distances and is updated as each sequential particle was added. This procedure is compared to the standard Random Sequential Addition method, used throughout the literature, and shows favourable results both in terms of computational cost and the suitability of the geometry for use in the creation of finite element meshes.

Finally, the application of the overall framework to realistic problems is presented. The procedure for carrying out an entire load step using a standard Newton-Rhapson procedure is outlined and the determination of the parameters used in the constitutive law is presented. Preliminary results are that demonstrated the performance of the overall framework. In these results, the softening of concrete due to fracture was captured.

Acknowledgements

First, I must thank my supervisors Professor Chris Pearce and Dr Lukasz Kaczmarczyk for their guidance and continued support. The help Chris has given me in the preparation of this thesis has been greatly appreciated and has allowed me to achieve a standard of work I am proud of. Lukasz's help, throughout my PhD, has been invaluable and he has been a constant source of guidance and encouragement. His patience with me, and his helpfulness, cannot be understated.

Next, I must thank all my friends and colleagues who I have had the pleasure to meet throughout the course of the PhD. Marnie (and Jay), Elisa (and Seb), Ross (and Jay), Sarah (and Martin), Alan, Dimitris, Ignatius, Caroline and James thanks for all the chats and fun. A special mention to Doug (and Hayley), without whom the last four years wouldn't have been the same and certainly would not have been nearly as enjoyable.

Thanks to my Mum and Sister (and the rest of our family), whose constant support and encouragement has really helped through the dark days of this process. I don't say it enough, but I couldn't have done this without you and thank you so much for your help!

Finally, I must thank my fiancée Kirsten. I started this endeavor with her unfaltering support and every single day she has made me happier than I can possibly express. She has been an unbelievable help throughout my PhD and I owe her a huge debt of gratitude. I will continue to repay this and I dedicate this work to her. Thank you Kirsten, I certainly wouldn't be here without you.

Contents

List of Figures

List of Tables

List of Algorithms

List of Symbols

B_0	ultimate shear strength of the material
$B(\kappa)$	shear strength at current damage value κ
B_u	residual shear strength of the material
$\mathbf{C}$	material compliance matrix
C_0	ultimate tensile strength of material
$C(\kappa)$	tensile strength at current damage value κ
C_u	residual tensile strength of the material
$\mathbf{D^{ep}}$	algorithmic stiffness
E	Young's Modulus
E^{int}	elastic modulus of the interface element
F	yield surface
$\mathbf{g}$	relative displacement vector
$\mathbf{g_e}$	elastic relative displacement
$\mathbf{g_p}$	plastic relative displacement
g_f	fracture energy
$\mathbf{I}$	identity matrix
$\mathbf{D^e}$	elastic stiffness matrix of the interface
$\mathbf{K_{cr}}$	stiffness matrix for interface element

$\mathbf{L}$ differential operator

$\mathbf{m}$ differential of plastic potential with respect to $\mathbf{t_{loc}}$

$\mathbf{N}$ matrix containing outward normal to the surface

$\mathbf{n}$ normal to the element face

$\mathbf{q}$ generalised displacement degrees of freedom on the boundary of the element

Q plastic potential

$\mathbf{S_v}$ matrix containing designed Trefftz functions

$\mathbf{s_1}$ first tangential direction to the element face

$\mathbf{s_2}$ second tangential direction to the element face

$\bar{\mathbf{t}}$ prescribed traction vector

t_n traction normal to interface

t_{s_1} traction tangential to the interface in direction s_1

t_{s_2} traction tangential to the interface in direction s_2

T transpose of a matrix

$\bar{\mathbf{u}}$ prescribed displacement vector

$\mathbf{u}$ displacement vector

$\mathbf{U}_\Gamma$ approximation matrix for boundary containing isoparametric shape functions

$\mathbf{u}_\Gamma$ displacements on the boundary of the element

$\mathbf{v}$ generalised stress degrees of freedom

VF Volume Fraction for Particle Packing

$\mathbf{w}_1$ weighting function for enforcement of statics

$\mathbf{w}_2$ weighting function for enforcement of kinematics

Greek Symbols

α tensile response variable for constitutive law

β shear response variable for constitutive law

ε strain vector

Γ element boundary

Γ_{cr} crack surface

γ_1 tensile response variable for constitutive law

γ_2 shear response variable for constitutive law

κ damage parameter

λ Lamé coefficient

$\dot{\lambda}$ plastic multiplier

μ Lamé coefficient or Shear Modulus

ν Poisson's Ratio

Ω element domain

σ Cauchy stress vector

Chapter 1

Introduction

1.1 Aims and Scope of the Study

With the modern day preference for light-weight, robust and durable structures, it is important that computational strategies are developed which will allow the behaviour of the materials being used to be captured. If the behaviour of the material at smaller scales can be accurately described, then the response of important structural elements will be more easily predicted. For heterogeneous materials, such as concrete, the mechanical behaviour is rooted in the behaviour of its heterogeneous microstructure. The work presented in this thesis will focus on capturing the crack evolution and propagation in concrete at small scales, allowing for a better understanding of its behaviour to be realised. In recent history, the increase in computational power has allowed researchers to develop methodologies where the heterogeneous mesostructure is explicitly resolved by the finite element mesh. This allows the behaviour of concrete in three distinct zones to be analysed; the aggregate particles themselves, the surrounding cement matrix and the weak interfacial transition zone between the two. As such, the work presented takes place at the mesoscale of concrete.

Cracking is driven by the stress state in the material, and so it is important to be able to approximate the stress state in an accurate fashion. This is achieved by using hybrid-Trefftz stress elements for the bulk elements in the analyses. When modelling crack evolution and propagation in concrete, there are various methods which have been utilised. Here, the discrete crack model has been used to explicitly model displacement discontinuities, which appear in a material when a crack appears. This was achieved by using continuous interface elements to capture the material non-linearity. These elements relate the tractions across

the discrete crack with the width of the crack. In this work, it has been assumed that the discrete cracks are limited to element boundaries. However, deviating from convention, there are no predefined areas in the mesh where cracks will appear. To ensure this was possible, a dynamic crack insertion algorithm was developed, which inserted cracks into a 3D mesh as required. When carrying out analyses where the heterogeneous mesostructure is explicitly resolved by the mesh, it is vital to ensure a geometry is created which allows the computational framework to perform well. Therefore, a particle packing methodology was developed, called the Maximum Level Set method, which allows geometries to be created in an efficient manner whilst producing good quality finite element meshes.

The overall objective for the work in this thesis was to develop a robust computational framework, which encompasses all the required aspects of capturing crack evolution and propagation in heterogeneous materials such as concrete. To achieve this, there are three distinct novel aspects to the work presented. First, the use of hybrid-Trefftz stress elements to accurately model the complex stress state needed to capture crack initiation and overcome the issue of traction oscillations when using interface elements. Second, the development of the new crack insertion methodology, which utilises properties of the hybrid-Trefftz finite elements. Finally, the development of the Maximum Level Set method for generation of the mesostructure.

1.2 Outline of the Thesis

The thesis has been split into various Chapters, each of which can be read individually with little cross referencing. The exception being Chapter 7, which uses the work presented in the preceding Chapters to illustrate the overall computational framework. The focus of each chapter is as follows:

– **CHAPTER 2** - A literature review is presented for different methodologies which have been used to capture failure in concrete. Throughout the Chapter there is discussion on the suitability of each method for use in the project being carried out in this thesis. A discussion on the historical development of hybrid type finite elements is presented along with a comparison of their benefits and limitations when compared to both boundary elements and classical finite elements.

– **CHAPTER 3** - A full derivation of the hybrid-Trefftz stress element is presented starting from the linear momentum balance equation. The formulation of the Trefftz functions which satisfy equilibrium *a priori* is discussed and simple numerical tests are presented which demonstrate the elements' performance for elastic problems.

– **CHAPTER 4** - The formulation of the continuous interface element is presented. Its integration into a mesh with bulk elements consisting of hybrid-Trefftz stress elements is discussed, with apparent benefits being highlighted. A plasticity-based constitutive law, called the Winnicki law, is presented and its numerical implementation is demonstrated, including a stress return algorithm. Simple 3D numerical tests are presented to demonstrate its effectiveness at capturing Mode I and Mode II fracture.

– **CHAPTER 5** - A computational strategy for inserting discrete cracks along existing element boundaries in 3D is presented. The methodology ensures that the yield criterion is obeyed at all times and it is demonstrated how the use of hybrid-Trefftz stress elements has aided its implementation. Numerical results showing the insertion algorithm in action are presented.

– **CHAPTER 6** - A method known as the Maximum Level Set method for creation of the heterogeneous mesostructure of concrete is presented. It is compared to the conventional method used in the literature, known as Random Sequential Addition. The benefits of the method are discussed and the computational implementation of the Maximum Level Set method is shown, along with results, to demonstrate its effectiveness.

– **CHAPTER 7** - This Chapter brings the work outlined in the preceding Chapters together into an holistic framework to solve problems where heterogeneities have been resolved explicitly by the mesh.

– **CHAPTER 8** - Concluding remarks on the work presented are given.

1.3 Notation

Throughout this thesis, matrix-vector notation will be used. In this notation, all matrices and vectors will be distinguished by bold-faced characters. A list of symbols is included for any symbols which are referred to more than once. Voigt notation has been used for the stress and strain vectors where appropriate.

Chapter 2

State of the Art Review

The behaviour of concrete has been widely investigated in recent history to allow a better understanding and description of its overall response to be obtained. Generally, the approach taken in the analysis of concrete can be split into two distinct groups. There are macroscale models, where concrete is often considered to be homogeneous, and mesoscale models, where heterogeneities in the concrete are explicitly considered. In this Chapter, a review will be undertaken to investigate the different methodologies which have been used to capture the quasi-brittle behaviour at both scales. The physical mechanisms which occur in concrete when it fails will be outlined and various methodologies to capture this behaviour will be discussed. Finally, due to the use of hybrid-Trefftz stress elements throughout this thesis, a review of the historical development of these elements will be undertaken to demonstrate their advantages when compared to different types of finite elements.

2.1 Failure Mechanisms in Concrete

In certain brittle engineering materials, linear elastic fracture mechanics can be used to predict crack growth and propagation. The stresses present near the crack front in 3D, or crack tip in 2D, are a function of the stress intensity factor, distance to the crack and the crack size, while the propagation of a crack is governed by the energy release rate of the material. However, these properties are not able to be determined exactly for a heterogeneous material such as concrete, where the structural makeup of the material due to aggregates, air voids and microcracks influences them. When evaluating concrete at a smaller scale, three distinct phases can be identified. First, there are the aggregates themselves, which are usually made

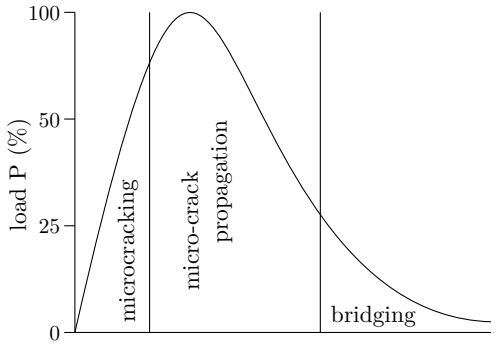

Figure 2.1: Simplified Softening Curve for Concrete Specimen in Tension[102]

up of crushed rock or gravel, second there is the matrix which is made up of the cement paste and third, there is the weak interfacial transition zone (ITZ) between the matrix and the aggregate. The relative stiffness of the first two phases causes stress concentrations to appear around the aggregate in the ITZ, which results in a non-uniform stress distribution. This phenomenon, and the relative weakness of the ITZ due its high porosity [102], results in microcracking initially occurring in this location. It has been found that the localised strains in the ITZ can be as high as 4.5 times the average strain in the specimen and the corresponding stresses were roughly twice as high, which explains why the initial cracking in concrete at the mesoscale appears in this area [25]. The heterogeneous structure results in quasi-brittle damage of the material, and the investigations carried out in this thesis will develop a computational methodology to find an accurate method to capture this behaviour.

In tension, concrete reaches a peak load before its ability to carry load is reduced by crack evolution, propagation and nucleation. An example graph of the applied load vs (average) crack opening over the cracked region of a simple notched beam subject to tension is shown in Figure 2.1. As can be seen, there is a period within concrete where microcracks form in the ITZ but the overall response is still almost linear. The ability of the specimen to carry tensile forces only reduces when these microcracks coalesce to form larger macrocracks. In fact, while cracking in concrete at the macroscale can be seen to be a fairly localised form of failure, the failure at the mesoscale occurs in a much less localized sense [102]. It has been found that when a macrocrack appears in concrete, the material still has the ability to transfer load due to the interlocking of crack faces and due to crack face bridges. Crack face bridges are essentially areas of the macrocrack where there is still a connection to the other side because the crack is not continuous, usually due to an aggregate particle, and this results in the tail of the graph in Figure 2.1. The detailed mechanism behind crack bridging is demonstrated in Figure 2.2. Interlocking of crack faces is caused by the friction between the two opposing crack faces not being smooth and trying to shear relative to each other.

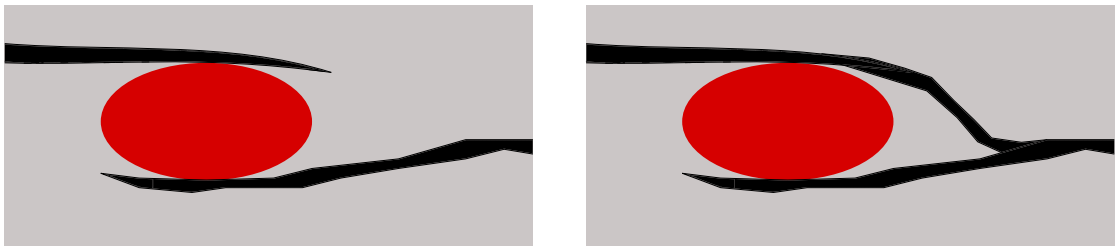

(a) Crack Bridging Around Stiff Aggregate (b) Crack Fully Connected Around Aggregate

Figure 2.2: Idealised demonstration of crack bridging[100]

Both Mode I and Mode II cracking are a combination of these two forms. Crack face bridges contribute almost exclusively to the residual load capacity of a specimen subjected to Mode I fracture, while interlocking does so for Mode II cracking [100].

The microstructure of concrete plays an important part in the overall behaviour of the material, from the initial loading to its post peak response. Van Mier [100] suggests that fracturing in concrete under tensile loading is a 3 stage process; firstly, there is nucleation of microcracks near large aggregates to create macrocracks; secondly, this macrocrack continues to grow while the crack bridging phenomena appears until finally, the crack bridge fails and there is complete failure of the material. Clearly, in all these stages, the heterogeneities in the material play an important part in the overall behaviour, regardless of the scale of the analysis. As such, the correct method of capturing the interaction with the heterogeneities is crucial. One way to do this is to explicitly resolve the heterogeneities in the material using the finite element mesh. This would then allow the behaviour in the ITZ to be accurately captured, giving an accurate solution in the macroscale. This method will also allow the critical issue of crack bridging to be captured. When analysing concrete to capture these phenomena, the macroscale approaches do not do this explicitly but capture them in a more holistic and average sense by treating concrete as a homogeneous material. On the other hand, there are approaches which have been used carry out detailed analyses of these phenomena where the heterogeneities are explicitly accounted for. Details of both approaches will now be discussed to present the preferred option for analysing the failure mechanisms present in the heterogeneous structure of concrete.

2.2 Computational Methodologies for Modelling Concrete Fracture

There has been a wide and varied investigation for many years into the numerical modelling of failure in heterogeneous materials, such as concrete, that began with the seminal papers of Rashid [76] and Ngo and Scordelis [64], which introduced the smeared and discrete crack models. A smeared crack model, in the most basic sense, modifies the stress-strain relationship within a finite element to represent a discontinuity in the continuum, while the discrete crack model inserts a strong discontinuity into the continuum and uses a traction-crack displacement relationship to represent the material behaviour. Both approaches were investigated and this section will discuss the evolution of both, as well as other relevant methods. A strong discontinuity, mentioned above, represents a jump in the displacement field within

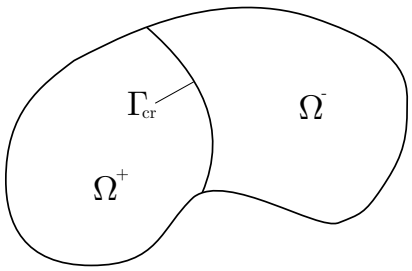

Figure 2.3: Body split by a discontinuity Γ_{cr}

the finite element mesh. A representation of this can be seen in Figure 2.3 where the surface, Γ_{cr}, splits the body into two distinct regions Ω^+ and Ω^-.When a strong discontinuity occurs the strains, locally, can be considered to tend to infinity. However, weak discontinuities and diffuse discontinuities also exist. Weak discontinuities occur when there is only C^0 continuity (i.e. there is a fracture zone of finite thickness and a jump in the strains in Ω takes place [65]). This is the essential idea behind the smeared crack model which will be discussed later. Finally, diffuse discontinuities occur when strains have extremely strong gradients [105]. For this case, the fractured zone is finite but the exact definition of the zone is established *a posteriori* from numerical results. A graphical representation of each type of discontinuity, with respect to the displacement and strain distributions, can be seen in Figure 2.4 for a case of uniaxial tension.

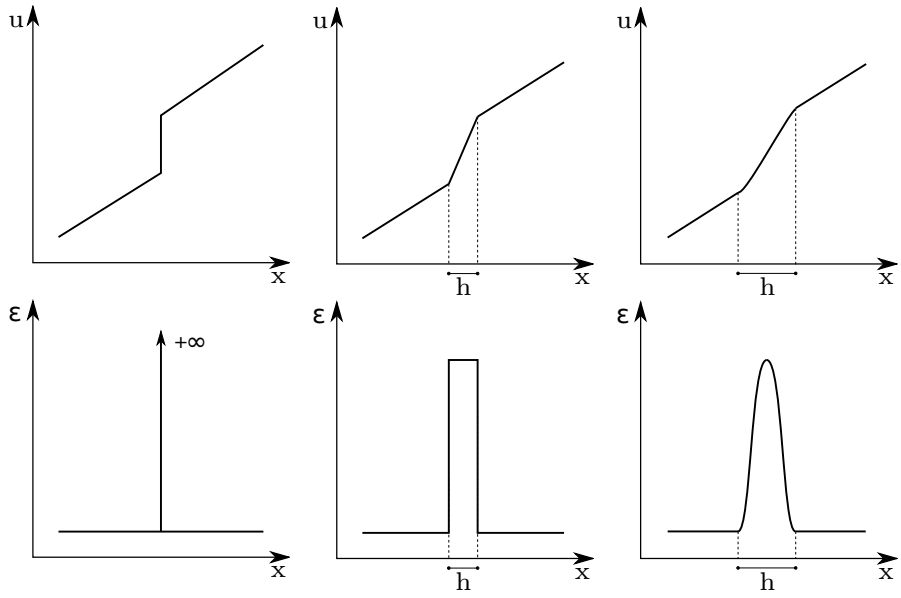

(a) Strong Discontinuity (b) Weak Discontinuity (c) Diffuse Discontinuity

Figure 2.4: Displacement and strain distributions for different discontinuities

2.2.1 Smeared Crack Model

After the proposal of smeared cracking by Rashid, various studies were carried out to improve the accuracy of the initial computational results. The introduction of a shear retention factor [88] allowed results to more closely match those obtained from experiments as the model could now capture aggregate interlock. In early investigations, it was assumed that the finite elements lost all stiffness in the direction of the principal stress to capture the softening behaviour of concrete and the shear retention factor was a scalar value which allowed the user to define a percentage of shear stiffness that was retained. However, the simple inclusion of this factor caused the principal stresses to rotate at an integration point on a crack when the loading was increased [28]. In the initial investigations into concrete, it was assumed that it was a perfectly brittle Griffiths material, which is not the case in reality. Concrete retains some level of cohesion when a crack develops, due to unbroken tendons across a crack and crack bridging, and as such tension-softening models were introduced to capture this phenomena. The introduction of this softening model, in conjunction with the shear retention factor, lead to a physically impossible situation where the major tensile stress could easily exceed the tensile strength in a different direction not perpendicular to the initial crack [27]. Another major problem discovered when using a smeared cracking approach with the simple inclusion of a tension-softening law, was an unrealistic and non-physical mesh sensitivity in the results [10]. To demonstrate this phenomena a simple 1D numerical model, shown in Figure 2.5, was evaluated. In this model, a single marginally weaker element was

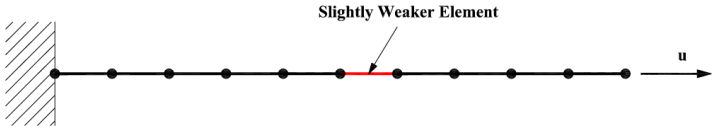

Figure 2.5: 1D problem to test mesh sensitivity

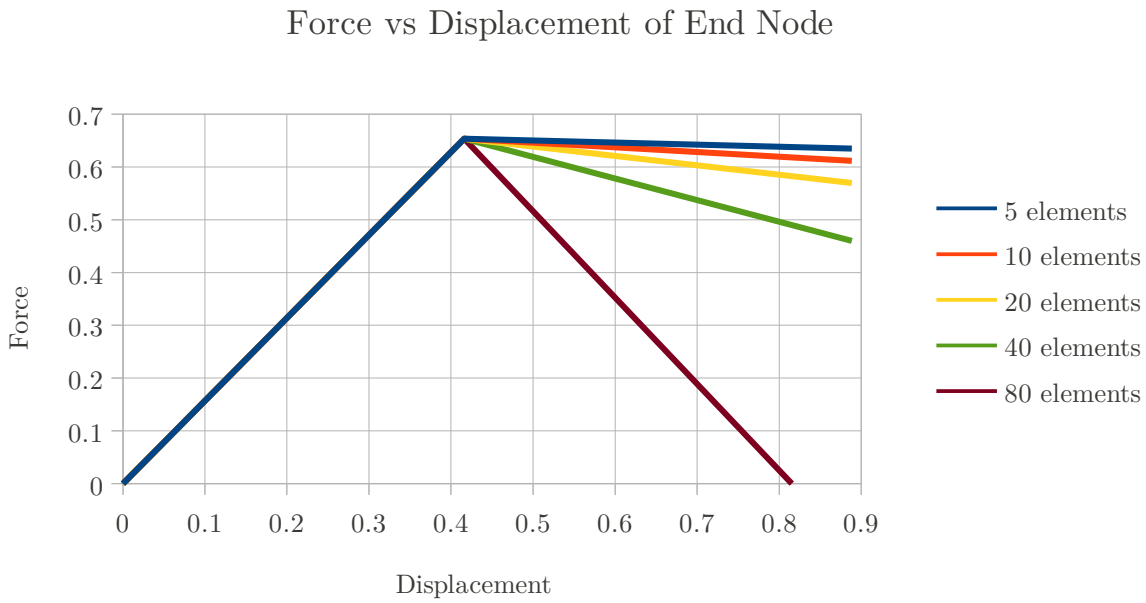

Figure 2.6: Load vs displacement graph for different element lengths

incorporated to ensure the location of the strain softening was known *a priori*. Representative values were used for material properties, a linear post-peak softening law was adopted and analyses were carried out for different levels of discretisation. The results in Figure 2.6 clearly show severe mesh dependence in the problem. In terms of energy dissipation, as the elements are reduced in size, the damage localises into a zone of smaller volume and this phenomena can reach a stage where, with infinitesimally small elements, there is failure with no energy dissipation [72].

2.2.2 Fracture Energy and the Fictitious Crack Model

Various methods to overcome the inherent problem of mesh sensitivity have been adopted. One of these was the introduction of fracture energy. In reality, concrete is a quasi-brittle material and displays some ductility after reaching its strength limit. This ductility appears in a small zone in front of the crack tip where microcracks begin and further develop. This area is called the Fracture Process Zone [28]. When the Fracture Process Zone is small enough in

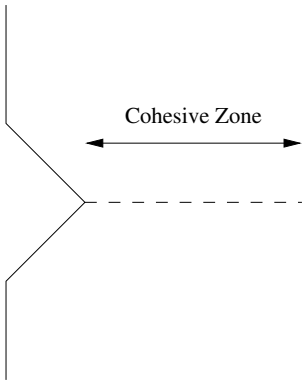

Figure 2.7: Cohesive Zone Model

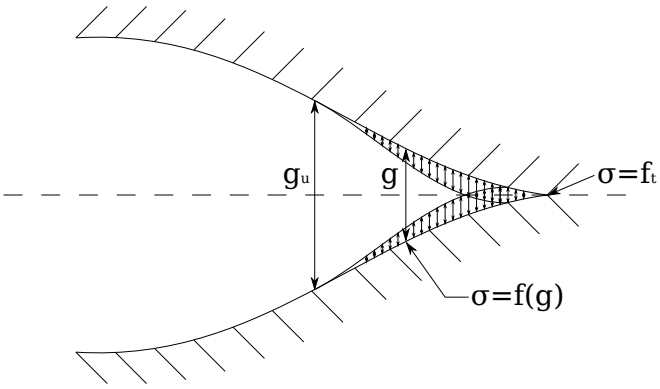

Figure 2.8: Fictitious Crack Model [41]

relation to the overall dimensions of the model being investigated it can be assumed linear-elastic behaviour is being observed. This can be seen in Figure 2.1, where cracks can be considered to be developing in the mesoscale even in the early loading portion of the graph. However, if large cracks begin to develop, and the Fracture Process Zone grows in size, there is a cohesive zone in the material which must be taken into consideration. The first application of the cohesive zone to quasi-brittle materials was the Fictitious Crack Model proposed by Hillerborg [41]. In a cohesive zone, all the microcracks that occur are lumped into a discrete line, shown in Figure 2.7, and it is assumed that there is a constitutive relationship which governs the stress reduction across the crack as the width increases. The model tries to capture the phenomena where stress transfer across the microcrack is still possible due to the presence of intact tendons in the material until eventually, this ability to transfer stress diminishes. A graphical representation can be seen in Figure 2.8, where g_u is the value of gap width where no tractions are transferable and g is the gap width at a given location. The energy required to overcome the residual tendons in the material is known as the fracture energy, g_f, which can be expressed as:

$$g_f = \int \sigma \mathrm{d}\mathbf{u} \tag{2.1}$$

where σ and $\mathbf{u}$ are the stresses and displacements across the Fracture Process Zone. The fracture energy is a material parameter which can be obtained experimentally [24, 59, 106], is dependent on both the material type and the size of the specimen being tested and has the dimension J/m^2. It also represents the area under the stress-displacement curve once the stress has reached the maximum tensile stress, f_t, as is shown in Figure 2.9 for a simple linear softening law. Here, g_u represents the relative displacement value at which a full crack has formed.

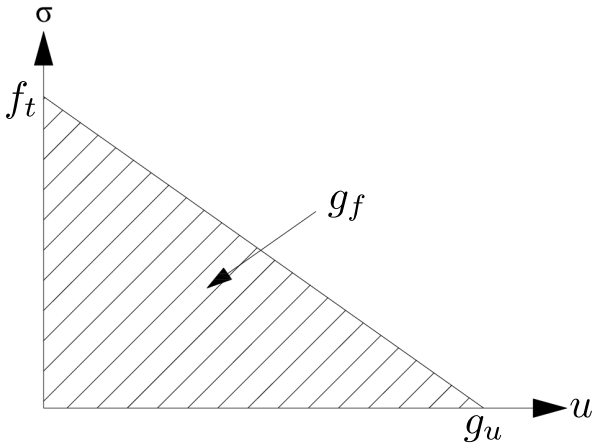

Figure 2.9: Linear softening law demonstrating fracture energy

The Fictitious Crack Model was originally applied to discrete cracking problems, but was adapted to be used in a smeared context by Bažant and Oh [14]. This application of the theory, to remove the mesh dependence in the formulation in 1D, is presented extremely effectively by de Borst [28]. It is also demonstrated that the adaptation of the formulation has introduced the element size into the equations to allow the mesh independent softening branch to be captured. However, this change to the model does not completely remove the mesh dependence in two and three dimensions and this difficulty had to be overcome. In fact, it has been suggested that the cracks should localise into a crack band of a given size, which is dependent on different element variables such as length and shape of the element. While the introduction of fracture energy into the smeared crack model alleviated some problems, there were still issues surrounding convergence due to the mesh refinement, the inherent length scale in the formulation because the element size cannot be smaller than the width of the crack band without further modification which introduces further complexity, mesh dependency of crack patterns and element types affecting crack patterns [55].

2.2.3 Nonlocal Approach

The nonlocal approach was proposed to overcome the mesh dependence problem identified above. In contrast to the local approach, here the stress state at a point depends on the strain in the vicinity of that point. The volume is defined in many different ways, but according to Bažant [12] the characteristic length, ℓ, which defines the volume can be considered to be roughly the same size as the size of the Fracture Process Zone. In 2D cases, ℓ can be either the diameter of a circle or the side of a square, with the stresses being calculated at the

centre point. Bažant also noted that the characteristic length can be related to the maximum aggregate size in concrete, or the maximum grain size in rocks or ice, by some multiple [12], but the evidence to support this conclusion is somewhat circumstantial. However, with the introduction of this characteristic length the nonlocal model is able to capture energy dissipation in the specimen being analysed. By ensuring there is a volume in the formulation, the nonlocal approach ensures that the strain-softening cannot localise into a region of vanishing volume and as such energy dissipation must occur. Finally, it was suggested that the nonlocal approach should only be applied to material variables which could be subjected to strain softening, while the rest of the variable should remain local [13]. This point was of specific importance to the elastic strain, which could develop substantial errors if calculated using the nonlocal method. Nonlocal models can broadly be split into two distinct groups; integral-type models and gradient-type models [7]. The difference between them is the integral-type models use a constitutive relationship which relates the stresses to the strains by carrying out some weighted averaging procedure, while gradient-type models enrich the constitutive relationship around the point in question with the gradient of a variable in the model. For instance, in calculating the stress at the point using the gradient-type method, the standard local stress-strain relationship is altered by the Laplacian of the strain. However, both types are considered to be nonlocal models as they contain the concept of a characteristic length and depend on the values surrounding the point in question rather than just the point itself [46].

There are both advantages and disadvantages to the nonlocal method. An advantage of the nonlocal method for curing mesh dependence over the fracture energy approach, is that all the inelastic deformations do not localise into one element. This localisation zone is therefore independent of the size of the element. Also, the plastic deformations in the model are not restricted to one element but restricted to the characteristic length, ℓ, which can be somewhat approximated using experimental data. The characteristic length presents problems because, although there is guidance on how it should be calculated, the actual values cannot be exactly related to a single material parameter. However, there is evidence to suggest the characteristic length can be related to material parameters in concrete relatively accurately. If the characteristic length is very small in comparison to the dimensions of the problem being investigated, this can results in very detailed analyses, with very fine meshes, having to be run to ensure correct results.

Throughout the brief overview of the smeared crack model presented, it can be seen that

there are computational difficulties associated with trying to approach the strain-softening phenomena in the continuum setting. Regardless of the method used, remedying the mesh dependence present in the initial work has been achieved by the introduction of a length scale. This may take the form of either a crack band in the model or a characteristic length scale. Both of these issues present their own unique problems which are still being overcome. However, the reason the non-local method cannot be used for the problems being investigated here is its unsuitability to accurately explicitly capture the exact crack paths or effects such as crack bridging as the crack is not modelled by the finite element mesh.

2.2.4 Discrete Crack Model

The method where a strong discontinuity in inserted into a finite element mesh is known as discrete cracking. This method involves modifying the mesh, and changing the connectivity of the elements, to introduce new degrees of freedom into the system so that a crack is present. It has been suggested, by Rots [78], that there are two major problems with this type of approach. First, the change of nodal connectivity is seen to go against the nature of the finite element displacement method and, second, the results are largely dependent on the underlying finite element mesh due to all cracking being limited to element boundaries. However, it was claimed, that when Mode I fracture of a material is being investigated, the discrete crack method can be a simple and effective way to analyse the model, as the orientation of the cracks were able to be predefined. While Rots felt that changing the nodal connectivity of a mesh to introduce a discrete crack was not an acceptable solution when using the finite element method, various proposals have been made to try and accomplish this in both 2D [21] and in 3D [67, 68, 69, 70]. Another solution to this problem will be discussed in Chapter 5 of this thesis, to demonstrate how discrete cracks were inserted into the initial finite element mesh by taking advantage of the hybrid-Trefftz stress elements used for the continuum. Another proposal to alleviate the problems of mesh dependency and connectivity changes, which has gained a large amount of popularity in recent times, is to allow a crack to pass through the domain of finite elements in the partition of unity approach.

2.2.5 Partition of Unity and XFEM

The partition of unity method was developed from the research into meshless methods [17] to overcome some of their drawbacks, as it was found that meshless methods were less

robust that classical finite elements, more computationally expensive and more difficult to implement in three dimensions [29]. The partition of unity in a domain Ω is achieved by using a set of functions $M_I(\mathbf{x})$ which satisfy:

$$\sum_{n=1}^{I} M_I(\mathbf{x}) = 1, \ \ \forall \mathbf{x} \in \Omega \tag{2.2}$$

Using (2.2), an equation for the displacements, or nodal unknowns, in an enriched sense, can be written as:

$$\mathbf{u}^h(\mathbf{x}) = \sum_{n=1}^{I} N_I(\mathbf{x})\mathbf{u}_I + \sum_{n=1}^{I} M_I(\mathbf{x})\psi(\mathbf{x})\mathbf{q}_I \tag{2.3}$$

where N_I are the standard isoparametric shape functions which satisfy the partition of unity, $\mathbf{u}_I$ are the standard nodal degrees of freedom, M_I contains a separate approximation base which can be, but is not usually, different to N_I, ψ contains the enrichment function and $\mathbf{q}_I$ are nodal values of unknown parameters, which when applied to the enrichment function ensure the approximated solution is correct [16]. In the modelling of strong discontinuities, $\psi(\mathbf{x})$ is the Heaviside function. The introduction of an enrichment function into the partial differential equations was a precursor to the extended finite element method, or XFEM.

XFEM was initially seen as an ideal, and versatile, tool for numerical modelling of problems investigating discontinuities, singularities, localised deformations and complex geometries [16]. The main benefit of XFEM was its ability to produce an accurate evolution of cracks without the need for re-meshing; thus eliminating one of the main drawbacks of using discrete cracks. Re-meshing was not required as the finite elements were enriched to allow the crack to pass through their domain rather than follow their boundaries. However, while XFEM can be considered perfect for modelling discrete cracks in homogeneous materials, there are several issues with the implementation. A simple demonstration of a crack modelled using XFEM is shown in Figure 2.10. The elements that contain a crack are highlighted and the nodes connected to a fully split element, known as step enriched nodes, are grouped into Ω_C, while the nodes of the partially split element, known as tip enriched nodes, are grouped into Ω_T. In XFEM, the highlighted elements contain the enrichment function to capture the discrete crack. This is different to the general partition of unity method, where the enrichment in carried out globally. However, obtaining the form of the local enrichment function can be extremely complex. Different enrichment functions are required when analysing different types of fracture (i.e. brittle or cohesive fracture) and when analysing fracture in an element containing a full crack or crack tip.

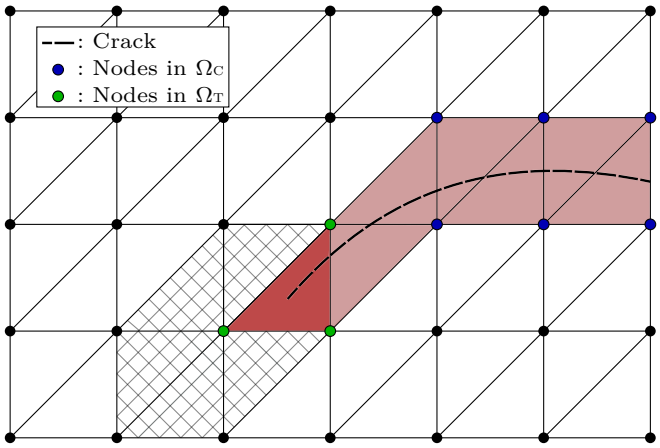

Figure 2.10: Mesh with crack showing enriched elements

When analysing fracture around a crack tip, a special enrichment function must be used, which are defined in terms of curvilinear coordinates φ and ψ and are related to the crack direction. These must be continuously updated throughout the analysis using the Level Set method. The Level Set method is used in XFEM because it is an efficient way to represent the crack by a simple *level set function*, f_Γ. This function is equal to zero at the crack location and as such the crack surface, Γ_{cr}, can be described as:

$$\Gamma_{cr} = \{x \,|\, f_\Gamma(x) = 0\} \tag{2.4}$$

and will allow the crack geometry to be implicitly described by a scalar value at each node in the mesh [46]. The Level Set method also allows the evolution of the crack over time to be captured. This is done by solving the hyperbolic evolution function:

$$\frac{\partial f_\Gamma}{\partial t} + v_n \left\| \frac{\partial f_\Gamma}{\partial x} \right\| = 0 \tag{2.5}$$

where v_n is the velocity in the normal direction to the crack surface and t is time. However, solving this hyperbolic function is often not accurate using the initial finite element mesh so another mesh, often a finite difference mesh, is used to update the Level Set values. Another problem in using the Level Set method is the crack surface must be frozen once it develops [16]. This problem has still yet to be adequately solved for XFEM.

Another problem that has been encountered in XFEM relates to the use of Gauss quadrature. When an element is enriched by a discontinuous function to capture cracking, standard Gauss quadrature can become extremely inaccurate and cause poor convergence of the system. To remedy this problem there are several known methods discussed by Belytschko [16]. All

these different methods add additional complications to the formulation and in some cases even result in subdivision of the elements containing a crack.

Another issue when using XFEM is the transition in a mesh between enriched elements, which contain a crack tip, and non-enriched elements. The problems associated with this are present in the hatched elements in Figure 2.10, where the elements contain both enriched and non-enriched nodes. Due to this mix of node types and the need to use a singular function to capture the crack tip, the shape functions in these elements no longer obey the partition of unity [16], which can result in errors and lead to a reduction in the rate of convergence. While this issue is able to be overcome, it again is adding another level of complexity to the formulation to overcome another weakness.

Finally, there are two explicit reasons why XFEM has not been used in the work carried out in this report. First, in problems where heterogeneities are explicitly resolved by the finite element mesh, there is a likely to be multiple cracks. This means that there will have to be large areas of the mesh where enrichment functions are used and as such the method does not become computationally viable. Second, in such problems with heterogeneities, the majority of cracks will initiate and propagate from the weak interface between an aggregate piece and the surrounding cement. As the finite element mesh will coincide with these weak interfaces it will be easier to insert discrete cracks into the topology in these areas without the added computational effort associated with XFEM.

Throughout the literature XFEM has been used to model brittle fracture, cohesive fracture [99], dynamic crack growth and various other forms of fracture in different types of material. In publications, the limitations and problems associated with XFEM have been discussed and explained and an attempt has been made to overcome them. This section of the report has outlined some of these limitations and given a brief overview of some of the solutions presented. However, it has also been shown that in solving the inherent problems with XFEM, layers of complexity have been added to the initial concept of the partition of unity which has made the implementation of XFEM to obtain accurate results challenging. It has also been noted that, while XFEM may be suitable for application to problems where the material is homogeneous, the case is less strong for materials where the heterogeneities are resolved by the mesh itself.

2.2.6 Interface Elements

It was suggested previously, that there were two major problems with using the discrete fracture approach: changing the connectivity of the mesh and mesh dependence of results. However, in this project, as the heterogeneities will be explicitly resolved by the finite element mesh, there is no obvious mesh dependency. This theory was presented, and results shown which supported it, by Kaczmarczyk and Pearce in 2009 for a two dimensional problem [52]. In this work, the relative stiffness of the heterogeneities to the surrounding material governed the crack path to a much greater extent than the underlying finite element mesh. Therefore, the results for the crack path and stress distributions for the numerical tests were found to be largely independent of the mesh used. Also, due to the explicit representation of the heterogeneities, the discrete fracture approach is able to accurately capture the mesoscale processes of crack initiation, growth and propagation in a manner that smeared crack methods cannot due to its smoothing process [30].

When using the discrete crack model, and limiting cracking to the element boundaries, interface elements have been widely used to model the cohesive nonlinear behaviour after the crack initiates. The initial work on interface elements was applied to model joints, or interfaces, in rock masses which contained discontinuities [36], but was then advocated for use in fracture mechanics of quasi-brittle materials such as concrete. Interface elements have a constitutive relationship embedded within them, which relates the tractions, $\mathbf{t}$, and gap width or relative displacements, $\mathbf{g}$, across the interface, which was first proposed by Hillerborg's Fictitious Crack Model [41] discussed in Section 2.2.2. Traditionally, interface elements were inserted into a mesh before the analysis began and an extremely high elastic stiffness was used to ensure the elastic response of the model was captured. This procedure could either by carried out in certain areas, if the crack location and propagation direction was known *a priori* , or interface elements could be inserted everywhere in the model. Xu and Needleman [107] suggested that, for 2D problems, an increase in computational time of the analysis of at least two, compared to a conventional finite element formulation, could be observed if interface elements were widely used, due to a large increase in degrees of freedom. This problem would be further exacerbated in 3D, where the numbers of degrees of freedom are much greater and the topology of the mesh is much more complex. Also, this approach can introduce errors into the linear-elastic result, as the extremely high elastic stiffness, known as a penalty stiffness, is employed. If the value of this penalty stiffness is too low then the model can become overly flexible, resulting in continuity of displacements not being achieved. However, if it is too high, then the resulting set of equations can become poorly conditioned [84]. In most discrete cohesive crack models, the penalty stiffness is chosen by

the user but careful consideration must be given to ensure a robust and accurate solution is found.

When using classical displacement finite elements, a significant problem of traction oscillations is present due to the inclusion of a high penalty stiffness [78, 79]. This issue occurred when using Gauss quadrature for the numerical integration of stiffness matrix and internal force vector of interface elements and was explored in some detail by Schellekens and de Borst [80]. Here, it was suggested that large stress gradients over the interface element and nodes on each separate side of the crack being coupled with one another were the root cause. To remedy this issue, nodal interface elements, or a different numerical integration scheme, could be used for a linear interface element. However, for a quadratic interface element the use of Newton-Cotes, Lobatto and Gauss integration schemes all resulted in traction oscillations occurring. It was suggested that, when using quadratic elements, Newton-Cotes and Lobatto integration schemes only resolve the traction oscillation issue for certain directions of displacement gradients and to remove the oscillations linear interface elements or extreme mesh refinement must be employed. In the work that is being carried out here, the problem of traction oscillations related to the interface is not applicable for two reasons. Firstly, as the traction oscillations occur due to the penalty stiffness, the development of a dynamic crack insertion algorithm reduces the number of inactive interface elements in the mesh. However, if an interface is inactive, the penalty stiffness is employed and Gauss integration is used the traction oscillations could occur. To remedy this hybrid-Trefftz stress elements are employed for the bulk elements in the mesh [52] with the reasoning behind this being discussed in Chapter 4.

It was shown that, in principle, the discrete crack model is intuitively much easier to understand and visualise and, in the author's opinion, is currently the best method to analyse cracking when heterogeneities are explicitly resolved by the mesh. The major problems associated with this method can be overcome and, as such, the discrete crack method will be used in the subsequent Chapters. There will be further discussion on both the use of interface elements to model the cohesive cracks and the crack insertion technique employed in Chapter 4 and Chapter 5.

2.2.7 Embedded Discontinuity Method

Another method of modelling fracture in materials, which has been widely used and investigated, is the embedded discontinuity method. A comprehensive literature review of this method was carried out by Jirásek [45], but this section will outline the details given in this paper to give an understanding of the method as well as some further advances in this method since the publication of this paper. The development of the embedded discontinuity method was carried out in response to the issue of shear locking in other smeared cracking methods. Shear locking occurs in these methods due to the linking of nodes on either side of a discontinuity in an element and results in spurious stress transfer across a wide crack which is not physically possible or realistic. This was caused by the inherent weakness of these other smeared methods in representing the kinematics the discontinuous displacement field and the embedded discontinuity method was developed to try overcome this.

The initial work into the embedded discontinuity method focused on modifying the linear elastic stress-strain relationship to take account of the softening or discontinuity within an element. This was achieved by replacing the relationship with a reduced secant stress-strain relationship which accounted for the damage in the element. However, the scope of this work was limited, as it was only able to be applied to simple perfect plastic cases and was not suitable for any other types of material which exhibit strain-hardening or strain softening. The seminal paper by Ortiz [66] focused on enriching the strain field of an element to allow a weak discontinuity, described in Figure 2.4, to be captured. This initial work allowed one weak discontinuity line to be captured per element. This meant that if there was a localisation band present in the specimen at least two elements were required to capture it. Through the course of the development of this method, it has been applied to different element types such as Constant Strain Triangles and Quad8 finite elements with a reasonable level of success. Following on from this work and its limitation of having only one line per element, Belytschko [15] introduced an improvement to allow at least two weak discontinuity lines to be present in each element. This meant the method became somewhat mesh independent and the localisation band width became a material parameter which could be found from experimental data.

While the early work associated with the embedded discontinuity method focused on weak discontinuities, Dvorkin [32] developed a formulation which could include a strong discontinuity within the element. This work was carried out using the principle of virtual work where an extra term was inserted into the formulation to allow the cohesive tractions over

the discontinuity to be calculated to allow the behaviour of a material such as concrete to be obtained.

In recent years, the embedded discontinuity method has been applied to several situations using different techniques. One application was an investigating localised failures in heterogeneous materials using structured finite element meshes where both displacement and strain discontinuities are included in the formulation [44]. In this method the strain discontinuity is solved along side the displacement degrees of freedom in the global system whilst the displacement discontinuity is treated as a localised plastic strain field which is solved within the integration loop of each element. Another application was to use the embedded discontinuity method to analyse failure in plane stress solids using quadrilateral finite elements with embedded discontinuities [31]. This was done by embedding the strain and displacement discontinuities within the element to capture the non-linear behaviour of the material and by allowing the displacement discontinuity to vary along the direction of the discontinuity.

The main issue with this method, with regards to the work being carried out in this report, is its inability to deal with the heterogeneities present in the material. The method develops a localisation band or displacement discontinuity within the element which has a single material property for the entire element. In this project, as the heterogeneities are being explicitly resolved by the finite element mesh any discontinuity will most likely be limited to the boundary between two material types which is more easily captured using the discrete crack method than the embedded discontinuity method.

2.2.8 Phase Field Method

A recent development into the investigation of crack propagation has been the phase field method. This principle behind this method is to take fracture that contains sharp crack discontinuities, where the computational modelling can suffer due to complex crack topologies, and improve it by using the diffusive crack modelling by introduction of a scalar auxiliary variable, known as the crack phase field [60, 61]. The crack phase field is essentially a supplementary field with a scalar variable, which interpolates between the cracked and uncracked states in a material. This method can be considered to be similar to continuum damage mechanics where the material is given a scalar value of damage between zero, intact, and one, fully damaged [38]. An advantage in 3D of this method over others, such as the use

of interface elements or XFEM, is that the diffusive nature of the phase field method allows crack branching to be easily captured because it does not explicitly model the discontinuities in the continuum. This method has an advantage of being able to be applied to specific cases of cracking in a dynamic setting [38].

The method can use various approximations for the phase field over the domain to capture both the diffusive crack topology and sharp cracks. Using the chosen approximation basis and the solution to the homogeneous differential equation, a functional can be developed, which when minimised gives the diffusive crack topology. This functional, when scaled with a user defined characteristic length, l, describes the crack surface itself. The approximation function to capture diffusive crack topology can easily be extended into 2D and 3D where the functional in 1D is known as the crack surface density function. This function depends on the approximation basis, or crack phase field, used and its gradient.

The approximation used by Miehe *et. al* [61] is governed by an inherent length scale chosen by the user and, as such, can lead to mesh-size limitations to produce accurate results. It was suggested, for a simple 2D problem investigating cracking using 4 noded quads, an element size

$$h < \frac{l}{2} \tag{2.6}$$

must be used to resolve the regularised crack surface, where h is the length of side of an element and l represents the characteristic length. The work that has been carried out at present on the phase field method has been limited to brittle fracture of solids and, as such, its implementation into cohesive cracking has not yet been investigated.

2.2.9 Mesoscale Analysis of Concrete Fracture

As the work in this thesis is focused on the mesoscale analysis of concrete, a short review of this particular type of analysis for investigating fracture in concrete will now be undertaken. A large amount of work has been carried out to model concrete fracture using a lattice approach. In the lattice approach the domain being analysed is decomposed into polygons using Voronoi tessellation where the nodes are inserted at random positions. When placing the nodes, a minimum distance is enforced depending on the density of the Voronoi cells that is required (which in turn effects the refinement of the mesh). The lattice elements then

connect the centres of the cells defined by the Voronoi tessellation to enable the behaviour between these points to be captured. This process is often carried out by Delaunay triangulation [37]. One way of dealing with the mesostructure of concrete using this method is to map the heterogeneous structure onto the lattice elements which have been created. This would then mean that any lattice elements which are inside the aggregate can have aggregate properties, any lattice elements in the cement matrix can have cement properties and any lattice elements which cross the boundary between the two can have properties of the ITZ [81]. Appropriate constitutive laws can then be embedded within these lattice elements to capture the material behaviour of the section of the material where it is located. This method has been applied by various authors to concrete at the mesoscale with realistic results being captured [37, 81].

The major advantage of the lattice approach when carrying out mesoscale analyses is that it is both computationally efficient and robust. However, mesh dependency of results must be taken into consideration. This problem can be somewhat alleviated by either ensuring that an irregular lattice is employed or by using specially designed constitutive laws [18]. The lattice approach was not considered for implementation in the work presented here due to the desire to investigate the benefits of using hybrid-Trefftz stress elements in capturing concrete fracture, such as their ability to approximate stresses to a high level, and due to the lattice models inherent differences to conventional continuum finite elements.

Further mesoscale studies of concrete have also been carried out by López *et. al.* [20, 22, 23, 57] which follows a similar path to the work presented in this thesis. In this work, zero-thickness interface elements are used in 2D with a constitutive law and Newton-Cotes integration rules. These interface elements are inserted along all potential crack paths which are present in the mesh *a priori*. The work presented in this thesis is similar but with some significant differences. First, the analysis is carried out in 3D. Second, a Newton-Cotes integration rule is not required in this thesis due to traction oscillations not being an inherent problem when using hybrid-Trefftz finite elements and third, interface elements are not present at the start of the analysis due to the implementation of a dynamic crack insertion algorithm. Caballero *et. al* did publish further work in 3D, but again this differs to the work presented here due to their use of classical finite elements and the presence of interface elements from the start of the analysis [19].

2.2.10 Discussion on Computational Methodologies

This section has outlined various different approaches to capturing the failure mechanisms in concrete, both by treating concrete as a homogeneous material at the macroscale and by treating it like a heterogeneous material at the mesoscale. The problems which are investigated in this thesis all use the finite element mesh to explicitly resolve the heterogeneities present in concrete. As this is the case, the methods which treat concrete as a homogeneous material, and in particular the smeared crack models, are not applicable. For this reason, a discrete crack approach will be utilised. When looking at discrete crack approaches, XFEM seems to be an attractive approach. However, because the heterogeneities are present in the mesh it is deemed inappropriate. XFEM would be preferable when using discrete cracks in a continuum setting, where mesh dependence is a concern. However, as has been discussed, mesh dependence is a reduced concern in the types of problems to be analysed where the heterogeneities will have a much bigger influence on the crack propagation and evolution.

As concrete is being analysed, interface elements are the best option for capturing the softening behaviour when used with cracks which follow element boundaries. There are issues with interface elements, in terms of both computational cost and traction oscillations, but by using hybrid-Trefftz stress elements the issue of traction oscillations can be overcome. The issue of computational implementation, due to difficulty of remeshing, can be overcome by developing a dynamic crack insertion algorithm which will minimise the computational cost.

2.3 Historical Development of Hybrid Elements

Classical finite elements are widely used, easily understood and can be easily applied to various engineering problems. However, there have been numerous developments made to develop the theory of the finite element method to improve its performance in certain situations. Hybrid-Trefftz stress elements will be used in this thesis to remove the traction oscillation problem present in interface elements and provide a more accurate representation of the stress state present in the model. As such, this section outlines the historical concept and major distinguishing points of this element type.

In 1964, work by Pian *et. al* [71] proposed a hybrid element where the stresses were approx-

imated over the element domain and the displacements were approximated separately over the element boundary, giving birth to what was known as the hybrid stress element. In this method the displacements on the boundary, also known as the *displacement frame*, allowed a stiffness matrix to be developed in a similar manner to classical finite elements and as such, initially, both these elements were used in a mesh; as demonstrated by Piltner [73] and Gerhardt [35]. It was found that improvements could be made to the classical finite element by satisfying the basic field equations, such as equilibrium, strain compatibility or Hooke's law in a weighted residual sense [51] allowing a better approximation for stresses, displacements or other internal variables to be obtained. A major benefit of this improved formulation is its suitability to parallel processing while still producing a symmetric system of equations [109].

The Trefftz method, produced in 1926 [98], is an alternative method to the Rayleigh-Ritz method for finding the approximate solution to the governing differential equation. In the Trefftz method, the governing equation is satisfied *a priori* in the element domain, Ω, and this method has been widely used throughout the literature. A full review of Trefftz type elements has been presented by Jirousek and Wróblewski [51] giving detailed explanations of Trefftz type elements up to its submission and directs the reader to various applications of these elements from Kirchhoff plate elements [48, 50] to thick plate elements[74] to axisymmetric solid mechanics and to transient heat conduction problems. Jirousek [51] states that

> "Owing to their nature, the Trefftz element, ... , may also be considered as a special, symmetric, substructure oriented boundary solution (BS) approach"

While these elements can be considered to be a BS approach, they also have some initial benefits over classical finite elements which were shown to include:

- greater accuracy for the same number of degrees of freedom;
- ability to use randomly shaped elements due to integration taking place on boundaries only;
- ability to capture stress singularities and concentrations without the need for mesh refinement;
- ability to better describe the stress state in a numerical model due to the implementation of a higher approximation basis;

- ability to have independent and unrelated faces on a single element, which do not necessarily have to *a priori* satisfy the partition of unity concept in an element. This can be advantageous when modifying mesh topology to insert discrete cracks.

Of these advantages, the last two are particularly significant. Being able to better describe the stress state reduces some of the problems with interface elements and, as fracture is a stress driven problem, will produce better results for scenarios investigating crack propagation and initiation. These points will be further discussed in Chapter 4. The ability to have independent and unrelated faces will be highlighted in some depth in Chapter 5, when the algorithm for dynamic crack insertion is fully discussed. While hybrid-Trefftz elements are a form of the BS approach, it can also take another form which uses the boundary integral equation and is known as the boundary element method (BEM). However, the hybrid-Trefftz elements have some advantages over the boundary element such as:

- the use of complex integration of singular functions required to achieve a solution are avoided [75];
- solving governing equations which are non-homogeneous is easily achieved using hybrid elements;
- it is still possible to achieve a sparse and symmetric stiffness matrix using hybrid elements;
- less computationally expensive than the BEM for problems where the geometry in complex;
- does not have fully populated matrices, thus increasing computational efficiency.

The BEM does have some advantages over both the FEM and hybrid-Trefftz elements, such as their suitability to solve problems with infinite domains and that they do no require sophisticated meshing programs to create the initial mesh. However, as the type of problems being solved are finite in nature and due to the wide availability of commercial meshing programs the benefits of the BEM are somewhat reduced. Also, Zienkiewicz [110] shows that to achieve symmetric matrices two separate sets of integration must be performed in the BEM, but at a cost to the computational efficiency. From these discussions, it can be seen that the hybrid-Trefftz type elements contain most of the advantages of both FEM and BEM. This allows accurate solutions to be achieved with minimal computational cost for detailed

	Jirousek Element Name	Freitas Element Name
Displacement approx. in Domain Traction approx. on Boundary	Traction Frame	Displacement
Stress approx. in Domain Displacement approx. on Boundary	Displacement Frame	Stress

Table 2.1: Naming Conventions for Hybrid-Trefftz elements

analyses, whilst any advantages the other methods have over it can largely be mitigated or are not considered to be significant.

2.3.1 Types of Trefftz Elements

Trefftz elements can largely be grouped into four distinct groups:

- hybrid elements with displacements approximated on boundary
- hybrid elements with tractions approximated on boundary
- frameless Trefftz formulations
- hybrid elements where displacements or tractions only approximated on inter element boundaries

At this point the use of different notations for the different element formulations must be discussed. Jirousek suggests that the hybrid-Trefftz elements with displacements approximated on the boundary be named *Hybrid-Trefftz elements with Displacement Frames* while elements with tractions on the boundary be *Hybrid-Trefftz elements with Traction Frames*. However, Freitas [92, 93, 94, 96] uses the terms hybrid-Trefftz displacement elements and hybrid-Trefftz stress elements respectively. The confusion emerges because the hybrid-Trefftz displacement element is actually equivalent to the Traction Frame element. The difference between these terminologies arises because Jirousek uses the approximation on the element boundary to name the elements while Freitas uses the approximation over the element domain. This explanation is clarified in Table 2.1. The naming convention used in this thesis follows the one set out by Freitas. Of the four different formulations of the hybrid-Trefftz elements, the most widely used and best known method is the hybrid-Trefftz stress element. This element has been widely used in the literature to investigate a array

of different problems including elastodynamic analysis [96], elastoplastic dynamic analysis [97] and has been used in fracture analysis problems in 2D [52]. This element is the most widely used due to the displacements being approximated separately on the boundary of the element. This approximation allows the global stiffness matrix to be assembled in a similar manner to classical displacement finite elements, while still including the advantages of the hybrid-Trefftz method such as the higher approximation of stresses.

A more in depth explanation and example of the formulation of the hybrid-Trefftz stress element will be included in Chapter 3.

2.4 Conclusion

This Chapter has set out the historical framework from which the work carried out in this thesis has been developed. Initially, the failure mechanisms present in a heterogeneous material were outlined. The area of the interfacial transition zone (ITZ) between the aggregate and the cement matrix was shown to be the most important area to model correctly when looking at concrete in the mesoscale, as this is where all microcracks initiate and coalesce from. Different fundamental issues were highlighted in the cracking behaviour of concrete such as crack bridging to explain why detailed modelling of this region is required. Several different methods, which have been used to model fracture in materials through out the history of computational mechanics, were outlined. These include smeared models, such as the nonlocal method, and discrete models, such as interface elements and XFEM. This discussion demonstrated that discrete models, and in particular the use of interface elements, where the crack path follows element boundaries are the most successful method for investigating cracking in heterogeneous materials at the mesoscale. This was because you could capture the different phenomena present in the materials such as crack branching and propagation. While there are limitations to this method, some examples of how they have been mitigated in the literature were given, while areas where there is still improvement to be made have been identified. These include using hybrid elements to remove the traction oscillations present in interface elements. Finally, a brief overview was given regarding hybrid elements. The development of these elements was discussed and some of their advantages over classical FEM and BEM were outlined.

Chapter 3

Hybrid-Trefftz Stress Elements

In the formulation of classical finite elements, the inability to approximate stresses accurately is an inherent weakness [95]. However, when investigating fracture in a heterogeneous material, such as concrete, an accurate approximation of the stress state is of paramount importance to ensure an accurate assessment of material fracture. As such, this Chapter will present the formulation of the hybrid-Trefftz stress element and demonstrate its superior properties for approximating stresses in comparison to classical finite elements. The limitation of the classical finite elements stems from the displacement based formulation, which results in the stresses being approximated to one order less than the displacements. However, in a hybrid element there are 2 fields present in a single element. One field is an approximation over the element domain, Ω_e, while the other is an approximation over the element boundary, Γ.

There are two different types of hybrid elements; hybrid stress elements and hybrid displacement elements. Hybrid stress elements, presented in this Chapter, approximate stresses within the element domain and displacements over the element boundary, while hybrid displacement elements approximate the displacements over the domain and the stresses over the boundary. The Trefftz method was first proposed by Trefftz [98] in 1926. It is an alternative method to the Rayleigh-Ritz method for finding the approximate solution to the governing differential equation and was applied to the finite element method by the pioneering work of Pian [71] and Jirousek and Leon [49]. Trefftz-type elements are characterised by *a priori* fulfilling the governing differential equations. There are several advantages to using the hybrid-Trefftz stress elements. In all situations, the formulation allows for a sparse and symmetric stiffness matrix to be obtained. The stiffness matrix, for static problems, can be calculated by carrying out integration over the boundary only. This allows arbitrary shaped

elements to be used, which can be convex or concave in shape. Due to the separate stress approximation basis, a much more accurate representation of stress concentrations can be achieved and, unlike classical finite elements, inconsistencies between the stress field within bulk elements and traction field in cohesive elements, which are discussed in Chapter 4, are avoided [52].

This chapter will outline the element formulation in detail, present the method used for determining the stress approximation, or Trefftz, functions and present some numerical examples to demonstrate the formulation is working as intended.

3.1 Element Formulation

3.1.1 Governing Equations

This section will outline the formulation of the hybrid-Trefftz stress element which is used in subsequent Chapters. The governing differential equation, where body forces are ignored for simplicity, for a typical element with a domain, Ω_e, and a boundary, $\Gamma = \Gamma_\sigma \cup \Gamma_u$ where $\Gamma_\sigma \cap \Gamma_u = \oslash$ are as follows:

$$\mathbf{L}^{\mathbf{T}}\boldsymbol{\sigma} = 0 \qquad \text{in } \Omega_e \tag{3.1}$$

$$\boldsymbol{\varepsilon} = \mathbf{C}\boldsymbol{\sigma} \qquad \text{in } \Omega_e \tag{3.2}$$

$$\boldsymbol{\varepsilon} = \mathbf{L}\mathbf{u} \qquad \text{in } \Omega_e \tag{3.3}$$

$$\mathbf{u} = \bar{\mathbf{u}} \qquad \text{on } \Gamma_u \tag{3.4}$$

$$\mathbf{N}\boldsymbol{\sigma} = \bar{\mathbf{t}} \qquad \text{on } \Gamma_\sigma \tag{3.5}$$

where $\mathbf{L}$ is a differential operator, $\mathbf{N}$ contains the unit normal of the element boundary, $\mathbf{C}$ is the material elastic compliance matrix, $\bar{\mathbf{u}}$ is the prescribed displacement vector applied to the kinematic boundary, Γ_u, and $\bar{\mathbf{t}}$ contains the prescribed tractions applied to the static boundary, Γ_σ. Using Equations (3.4) and (3.5), the relationship for inter-element continuity

can be obtained as follows [92]:

$$\mathbf{t}_{\Gamma}^{el_1} + \mathbf{t}_{\Gamma}^{el_2} = 0 \qquad \text{on } \Gamma^{el_1} \cap \Gamma^{el_2} \tag{3.6}$$

$$\mathbf{u}_{\Gamma}^{el_1} - \mathbf{u}_{\Gamma}^{el_2} = 0 \qquad \text{on } \Gamma^{el_1} \cap \Gamma^{el_2} \tag{3.7}$$

where el_1 and el_2 signify the elements on either side of the boundary. To ensure a statically admissible solution, a stress distribution must satisfy locally both the equilibrium condition (3.1) and the static boundary condition (3.6). In addition, to ensure a kinematically admissible solution the displacement field must satisfy (3.4) and (3.7) and be associated with the strain distribution $\boldsymbol{\varepsilon}$ given by the compatibility condition in (3.3).

In three dimensions $\mathbf{L}$ is:

$$\mathbf{L}^{\mathrm{T}} = \begin{bmatrix} \frac{d}{dx} & 0 & 0 & \frac{d}{dy} & 0 & \frac{d}{dz} \\ 0 & \frac{d}{dy} & 0 & \frac{d}{dx} & \frac{d}{dz} & 0 \\ 0 & 0 & \frac{d}{dz} & 0 & \frac{d}{dy} & \frac{d}{dx} \end{bmatrix} \tag{3.8}$$

and matrix $\mathbf{N}$ is:

$$\mathbf{N} = \begin{bmatrix} n_1 & 0 & 0 & n_2 & 0 & n_3 \\ 0 & n_2 & 0 & n_1 & n_3 & 0 \\ 0 & 0 & n_3 & 0 & n_2 & n_1 \end{bmatrix} \tag{3.9}$$

where n_1, n_2 and n_3 are the components of the outward normal in the x, y and z directions respectively. Matrix $\mathbf{C}$ is:

$$\mathbf{C} = \begin{bmatrix} \frac{\lambda+\mu}{\mu(3\lambda+2\mu)} & \frac{-\lambda}{2\mu(3\lambda+2\mu)} & \frac{-\lambda}{2\mu(3\lambda+2\mu)} & 0 & 0 & 0 \\ \frac{-\lambda}{2\mu(3\lambda+2\mu)} & \frac{\lambda+\mu}{\mu(3\lambda+2\mu)} & \frac{-\lambda}{2\mu(3\lambda+2\mu)} & 0 & 0 & 0 \\ \frac{-\lambda}{2\mu(3\lambda+2\mu)} & \frac{-\lambda}{2\mu(3\lambda+2\mu)} & \frac{\lambda+\mu}{\mu(3\lambda+2\mu)} & 0 & 0 & 0 \\ 0 & 0 & 0 & \frac{1}{\mu} & 0 & 0 \\ 0 & 0 & 0 & 0 & \frac{1}{\mu} & 0 \\ 0 & 0 & 0 & 0 & 0 & \frac{1}{\mu} \end{bmatrix} \tag{3.10}$$

where λ and μ are the Lamé coefficients. In hybrid-Trefftz stress elements, the stresses in Ω_e are approximated as:

$$\boldsymbol{\sigma} = \mathbf{S}_{\mathbf{v}}\mathbf{v} \tag{3.11}$$

where $\mathbf{S}_{\mathbf{v}}$ is the matrix containing the Trefftz approximation functions, which will be discussed in Section 3.2. The vector $\mathbf{v}$ contains the generalised stress degrees of freedom, which

will not, in general, represent the nodal stresses in the finite element. As was mentioned earlier, the Trefftz approximation functions are chosen to *a priori* satisfy the momentum balance equation and, as such, by substituting (3.11) into (3.1) it can be seen that:

$$\mathbf{L}^{\mathrm{T}}\mathbf{S}_{\mathbf{v}}\mathbf{v} = 0 \tag{3.12}$$

This equation must hold for arbitrary values of the stress degrees of freedom and therefore the following must hold:

$$\mathbf{L}^{\mathrm{T}}\mathbf{S}_{\mathbf{v}} = 0 \tag{3.13}$$

Thus, the Cauchy equilibrium condition, shown in (3.5), on the surface of the element is given by:

$$\mathbf{t} = \mathbf{N}\boldsymbol{\sigma} = \mathbf{N}\mathbf{S}_{\mathbf{v}}\mathbf{v} \tag{3.14}$$

The displacement field within the element domain can be expressed, with respect to the generalised stress degrees of freedom, $\mathbf{v}$, as:

$$\mathbf{u} = \mathbf{U}_{\mathbf{v}}\mathbf{v} \tag{3.15}$$

where the matrix containing the stress approximation functions, $\mathbf{S}_{\mathbf{v}}$, are related to the displacement approximation field as follows:

$$\mathbf{S}_{\mathbf{v}} = \mathbf{C}^{-1}(\mathbf{L}\mathbf{U}_{\mathbf{v}}) \tag{3.16}$$

Here, it can be noted, that the approximation of the displacements and the approximation of the stresses are related by the constitutive law, which is contained within the compliance matrix, $\mathbf{C}$.

3.1.2 Enforcement of Static Boundary Condition

The static boundary condition, given in (3.5), is enforced in a weighted residual sense as follows:

$$\int_{\Gamma_\sigma} \mathbf{w}_1^{\mathrm{T}}(\mathbf{N}\boldsymbol{\sigma} - \bar{\mathbf{t}})\,\mathrm{d}\Gamma = 0 \tag{3.17}$$

where $\mathbf{w}_1$ is an appropriate weighting function. Substituting (3.11) into the above gives:

$$\int_{\Gamma_\sigma} \mathbf{w}_1^{\mathrm{T}}\mathbf{N}\mathbf{S}_{\mathbf{v}}\mathbf{v}\,\mathrm{d}\Gamma = \int_{\Gamma_\sigma} \mathbf{w}_1^{\mathrm{T}}\bar{\mathbf{t}}\,\mathrm{d}\Gamma \tag{3.18}$$

The right hand term of this equation represents the increment of stress work on the boundary of an element and as such has the unit of work. Thus, the weighting function $\mathbf{w}_1$, to ensure an energy consistent formulation, takes the form:

$$\mathbf{w}_1 = \mathbf{U}_\Gamma \mathbf{v}_\mathbf{u} \tag{3.19}$$

where $\mathbf{v}_\mathbf{u}$ are the discrete values of the weighting function and $\mathbf{U}_\Gamma$ is a matrix containing the approximation functions for the approximation over the element surfaces. In this work, the approximation functions are the standard isoparametric shape functions and thus, $\mathbf{U}_\Gamma$ is given by:

$$\mathbf{U}_\Gamma = \left[\begin{array}{ccccccc} N_1\mathbf{I} & \vdots & N_2\mathbf{I} & \vdots & \cdots & \vdots & N_i\mathbf{I} \end{array} \right] \tag{3.20}$$

where N_i is the isoparametric shape function of the given node and $\mathbf{I}$ is the identity matrix. Inserting (3.19) into (3.18) gives:

$$\forall \mathbf{v}_\mathbf{u} \quad \mathbf{v}_\mathbf{u}^\mathrm{T} \int_{\Gamma_\sigma} \mathbf{U}_\Gamma^\mathrm{T} \mathbf{N} \mathbf{S}_\mathbf{v} \mathbf{v} \, \mathrm{d}\Gamma = \mathbf{v}_\mathbf{u}^\mathrm{T} \int_{\Gamma_\sigma} \mathbf{U}_\Gamma^\mathrm{T} \bar{\mathbf{t}} \, \mathrm{d}\Gamma \tag{3.21}$$

3.1.3 Enforcement of Kinematics

A kinematically admissible solution is achieved if the displacement field in an element satisfies the kinematic boundary condition, given by (3.4), satisfies inter-element continuity on the boundary between two elements and is also associated to the strains in the element by (3.3) [92]. If we initially consider this final condition, then this can be satisfied in a weighted residual sense by:

$$\int_\Omega \mathbf{w}_2^\mathrm{T} (\boldsymbol{\varepsilon} - \mathbf{L}\mathbf{u}) \, \mathrm{d}\Omega = 0 \tag{3.22}$$

where $\mathbf{w}_2$ is another appropriate weighting function, chosen so as to ensure that the integral has units of work. The weak form of the above equation is then obtained by applying Green's theorem to the second term of the equation to give:

$$\int_\Omega \mathbf{w}_2^\mathrm{T} \boldsymbol{\varepsilon} \, \mathrm{d}\Omega + \int_\Omega (\mathbf{L}^\mathrm{T} \mathbf{w}_2)^\mathrm{T} \mathbf{u} \, \mathrm{d}\Omega - \int_\Gamma (\mathbf{N}\mathbf{w}_2)^\mathrm{T} \mathbf{u} \, \mathrm{d}\Gamma = 0 \tag{3.23}$$

As can be seen, a term containing a boundary integral has now appeared in the equation, which can be uncoupled into its static and kinematic boundaries to give the following:

$$\int_{\Omega} \mathbf{w}_2^{\mathrm{T}} \boldsymbol{\varepsilon} \, \mathrm{d}\Omega + \int_{\Omega} (\mathbf{L}^{\mathrm{T}} \mathbf{w}_2)^{\mathrm{T}} \mathbf{u} \, \mathrm{d}\Omega - \int_{\Gamma_\sigma} (\mathbf{N}\mathbf{w}_2)^{\mathrm{T}} \mathbf{u} \, \mathrm{d}\Gamma = \int_{\Gamma_u} (\mathbf{N}\mathbf{w}_2)^{\mathrm{T}} \bar{\mathbf{u}} \, \mathrm{d}\Gamma \tag{3.24}$$

The weighting function, $\mathbf{w}_2$, was then chosen to ensure an energy consistent formulation:

$$\mathbf{w}_2 = \mathbf{S}_{\mathbf{v}} \mathbf{v}_{\mathbf{s}} \tag{3.25}$$

where $\mathbf{v_s}$ are the discrete values of the weighting function $\mathbf{w}_2$. Substituting (3.3) into (3.24) results in:

$$\forall \mathbf{v_s} \quad \mathbf{v}_{\mathbf{s}}^{\mathrm{T}} \int_{\Omega} \mathbf{S}_{\mathbf{v}}^{\mathrm{T}} \mathbf{C} \mathbf{S}_{\mathbf{v}} \mathbf{v} \, \mathrm{d}\Omega + \mathbf{v}_{\mathbf{s}}^{\mathrm{T}} \int_{\Omega} (\mathbf{L}^{\mathrm{T}} \mathbf{S}_{\mathbf{v}})^{\mathrm{T}} \mathbf{u} \, \mathrm{d}\Omega - \mathbf{v}_{\mathbf{s}}^{\mathrm{T}} \int_{\Gamma_\sigma} (\mathbf{N}\mathbf{S}_{\mathbf{v}})^{\mathrm{T}} \mathbf{u} \, \mathrm{d}\Gamma = \mathbf{v}_{\mathbf{s}}^{\mathrm{T}} \int_{\Gamma_u} (\mathbf{N}\mathbf{S}_{\mathbf{v}})^{\mathrm{T}} \bar{\mathbf{u}} \, \mathrm{d}\Gamma \tag{3.26}$$

Due to (3.12), the second term of the above equation can be eliminated. Furthermore, certain conditions need to be investigated within the overall formulation of the hybrid-Trefftz stress elements [52]. These are:

1. $\Gamma = \Gamma_u$ (i.e. there are only prescribed displacement on the body and $\Gamma_\sigma = 0$).
2. $\Gamma = \Gamma_\sigma$ (i.e. there are only prescribed tractions on the boundary and $\Gamma_u = 0$).
3. $\Gamma = \Gamma_\sigma \cup \Gamma_u$ where $\Gamma_\sigma \cap \Gamma_u = \emptyset$. (i.e. there are both prescribed displacements and prescribed tractions on the boundary but not at the same point).

In Condition 1, Equation (3.21) and the third term of (3.26) vanish and as such the only unknown in either equation is the generalised stress degrees of freedom, $\mathbf{v}$. The only prescribed term in either equation is the displacements, $\bar{\mathbf{u}}$, and therefore, the formulation describes the kinematics in a weighted residual weak sense which satisfies the compatibility within an element in an average sense. In Condition 2, the unknown, $\mathbf{v}$, can be found due to (3.21) alone because the entire boundary is being subjected to prescribed tractions, $\bar{\mathbf{t}}$. In Condition 3, which is the most general case, to maintain the independence of statics and kinematics, an additional displacement approximation field over the traction boundary, Γ_σ, of the element, $\mathbf{u}_\Gamma$, must be introduced. This approximation is independent of the approximation of the displacements within the element domain, $\mathbf{U_v}$, mentioned earlier and takes the form:

$$\mathbf{u}_\Gamma = \mathbf{U}_\Gamma \mathbf{q} \tag{3.27}$$

where $\mathbf{U}_\Gamma$ is the matrix of approximation functions introduced in (3.20) and $\mathbf{q}$ is a vector containing the generalised displacement degrees of freedom on the boundary of the element. The separate approximations over the element domain, Ω_e, and the element boundary, Γ_e, result in a hybrid type of element formulation. Due to these conditions, Equation (3.26) can be re-written as:

$$\forall \mathbf{v_s} \quad \mathbf{v_s}^{\mathrm{T}} \int_{\Omega} \mathbf{S_v}^{\mathrm{T}} \mathbf{C} \mathbf{S_v} \, \mathrm{d}\Omega - \mathbf{v_s}^{\mathrm{T}} \int_{\Gamma_\sigma} (\mathbf{N}\mathbf{S_v})^{\mathrm{T}} \mathbf{U}_\Gamma \mathbf{q} \, \mathrm{d}\Gamma = \mathbf{v_s}^{\mathrm{T}} \int_{\Gamma_u} (\mathbf{N}\mathbf{S_v})^{\mathrm{T}} \bar{\mathbf{u}} \, \mathrm{d}\Gamma \tag{3.28}$$

At this stage, is it appropriate to highlight the difference between hybrid elements and mixed elements which can be found in the literature. As was stated previously, in hybrid elements there are two separate approximations in a single element. However, these do not approximate over the same domain as one approximation takes place over the element domain, while another approximates over the element boundary. In mixed elements, this aspect is not true. In these elements separate approximations for different variables such as displacements, strains and stresses can all be approximated over a single domain [6]. This type of mixed formulation has been combined with the hybrid approach outlined here to produce hybrid-mixed elements. This type of element can be used to extend the hybrid-Trefftz formulation outlined in this Chapter to dynamic problems.

3.1.4 System of Equations

Equations (3.21) and (3.28) result in a coupled set of equations. These equations can be written in matrix form as follows:

$$\begin{bmatrix} \mathbf{F} & -\mathbf{A}^{\mathrm{T}} \\ -\mathbf{A} & 0 \end{bmatrix} \begin{bmatrix} \mathbf{v} \\ \mathbf{q} \end{bmatrix} = \begin{bmatrix} \mathbf{p}_u \\ -\mathbf{p}_\sigma \end{bmatrix} \tag{3.29}$$

where
$$\mathbf{F} = \int_{\Omega} \mathbf{S_v}^{\mathrm{T}} \mathbf{C} \mathbf{S_v} \, \mathrm{d}\Omega$$
$$\mathbf{A} = \int_{\Gamma} \mathbf{U}_\Gamma^{\mathrm{T}} \mathbf{N} \mathbf{S_v} \, \mathrm{d}\Gamma$$
$$\mathbf{p_u} = \int_{\Gamma_u} (\mathbf{N}\mathbf{S_v})^{\mathrm{T}} \bar{\mathbf{u}} \, \mathrm{d}\Gamma$$
$$\mathbf{p}_\sigma = \int_{\Gamma_\sigma} \mathbf{U}_\Gamma^{\mathrm{T}} \bar{\mathbf{t}} \, \mathrm{d}\Gamma$$

This system of equations can be modified using static condensation to reduce the size of the set of algebraic equations for each hybrid-Trefftz stress element [52]. The first equation is

rearranged to find an equation for $\mathbf{v}$:

$$\mathbf{v} = \mathbf{F}^{-1}\mathbf{p}_u + \mathbf{F}^{-1}\mathbf{A}^{\mathrm{T}}\mathbf{q} \tag{3.30}$$

This can then be substituted into the second equation to give a solution entirely in terms of the generalised displacement degrees of freedom, $\mathbf{q}$.

$$(\mathbf{A}\mathbf{F}^{-1}\mathbf{A}^{\mathrm{T}})\mathbf{q} = \mathbf{p}_\sigma - \mathbf{A}^{\mathrm{T}}\mathbf{F}^{-1}\mathbf{p}_u \tag{3.31}$$

where $\mathbf{A}\mathbf{F}^{-1}\mathbf{A}^{\mathrm{T}}$ can be considered to be the element stiffness matrix. If isoparametric shape functions are used for the boundary approximation, as was done here, then the stiffness matrix for an element contains the same number of rows and columns as a classical finite element. This means that, even with the increased stress approximation basis, solving the problem is no more computationally expensive as both the bandwidth and dimensions of the element stiffness matrix would be equal. The use of static condensation also means that the stiffness matrix is symmetric and positive definite. Once $\mathbf{q}$ has been determined, the generalised stress degrees of freedom for each element can be found independently of all other elements, a process which lends itself to using parallel processing [52].

One advantage of the hybrid-Trefftz stress element is that the formulation can be manipulated to ensure only boundary integrals are present in the equations. Considering (3.29), only $\mathbf{F}$ contains a volume integral. However, as $\boldsymbol{\varepsilon} = \mathbf{C}\boldsymbol{\sigma} = \mathbf{C}\mathbf{S}_\mathbf{v}\mathbf{v}$ and $\boldsymbol{\varepsilon} = \mathbf{L}\mathbf{u} = \mathbf{L}\mathbf{U}_\mathbf{v}\mathbf{v}$ the volume integral for $\mathbf{F}$ can be rewritten as:

$$\mathbf{F} = \int_\Omega \mathbf{S}_\mathbf{v}^{\mathrm{T}}\mathbf{C}\mathbf{S}_\mathbf{v}\,\mathrm{d}\Omega = \int_\Omega \mathbf{S}_\mathbf{v}^{\mathrm{T}}(\mathbf{L}\mathbf{U}_\mathbf{v})\,\mathrm{d}\Omega \tag{3.32}$$

Applying Green's theorem leads to:

$$\mathbf{F} = \int_\Omega \mathbf{S}_\mathbf{v}^{\mathrm{T}}\mathbf{C}\mathbf{S}_\mathbf{v}\,\mathrm{d}\Omega = -\int_\Omega \mathbf{U}_\mathbf{v}^{\mathrm{T}}\mathbf{L}^{\mathrm{T}}\mathbf{S}_\mathbf{v}\,\mathrm{d}\Omega + \int_\Gamma \mathbf{S}_\mathbf{v}^{\mathrm{T}}\mathbf{N}\mathbf{U}_\mathbf{v}\,\mathrm{d}\Gamma \tag{3.33}$$

which generates a boundary integral in the formulation. Due to (3.12), the first term on the right hand side of this equation can be eliminated and $\mathbf{F}$ can be described by the following boundary integral:

$$\mathbf{F} = \int_\Gamma \mathbf{S}_\mathbf{v}^{\mathrm{T}}\mathbf{N}\mathbf{U}_\mathbf{v}\,\mathrm{d}\Gamma \tag{3.34}$$

It must be noted that this manipulation can only be carried out for static analyses where $\mathbf{L}^{\mathrm{T}}\mathbf{S}_\mathbf{v} = 0$, and for dynamic analyses, where this does condition does not hold, the evaluation

of a volume integral will always be necessary. If n_V and n_Γ are the total number of linearly independent stress and boundary displacement approximation functions implemented in the analysis, then the following relationship must hold [92]:

$$n_V - n_\Gamma \geqslant 0 \tag{3.35}$$

This condition ensures a statically and kinematically admissible unique solution. For a three dimensional mesh containing 10-noded tetrahedrons, each face of the tetrahedron will have 18 degrees of freedom with 18 separate quadratic approximation functions using the approximation basis outlined for $\mathbf{U}_\Gamma$. This means the minimum number of stress approximation functions in an element can be no lower than 18.

3.2 Formulation of Trefftz Functions

In the hybrid-Trefftz stress formulation, the equilibrium condition in the element domain must be satisfied *a priori*. This is ensured in Equation 3.12 by designing Trefftz functions contained in $\mathbf{S_v}$ in an appropriate manner. These functions are determined with the assumption that the material is isotropic and linear elastic. Furthermore, body forces are ignored for simplicity. The process of construction of the approximation functions used in $\mathbf{S_v}$ is demonstrated here in 2D for simplicity, but the methodology is equally valid for full implementation into 3D. When a structure is statically loaded and in a state of equilibrium, it must have a displacement field which can be described by the Lamé-Navier equation:

$$(\lambda + \mu)u_{j,ij} + \mu u_{i,jj} = 0 \tag{3.36}$$

where indicial notation is used here for convenience and *i*=*x* and *j*=*y* for a 2D problem. λ and μ are the Lamé coefficients given by:

$$\mu = G = \frac{E}{2(1+\nu)} \tag{3.37}$$

$$\lambda = \frac{E\nu}{(1+\nu)(1-2\nu)} \tag{3.38}$$

where E is the Young's modulus of the material and ν is the Poisson's ratio. Equation 3.12 in 2D is given by:

$$\begin{cases} \frac{\partial \sigma_x}{\partial x} + \frac{\partial \sigma_{xy}}{\partial y} = 0 \\ \frac{\partial \sigma_y}{\partial y} + \frac{\partial \sigma_{xy}}{\partial x} = 0 \end{cases} \tag{3.39}$$

where these equations can be expressed using (3.36) as:

$$\frac{\partial \sigma_x}{\partial x} + \frac{\partial \sigma_{xy}}{\partial y} = \mu \left[\frac{\partial^2 u_x}{\partial x^2} + \frac{\partial^2 u_x}{dy^2} \right] + (\mu + \lambda) \left[\frac{\partial^2 u_x}{\partial x^2} + \frac{\partial^2 u_y}{\partial x \partial y} \right] = 0 \tag{3.40}$$

$$\frac{\partial \sigma_y}{\partial y} + \frac{\partial \sigma_{xy}}{\partial x} = \mu \left[\frac{\partial^2 u_y}{\partial y^2} + \frac{\partial^2 u_y}{dx^2} \right] + (\mu + \lambda) \left[\frac{\partial^2 u_y}{\partial y^2} + \frac{\partial^2 u_x}{\partial x \partial y} \right] = 0 \tag{3.41}$$

To construct $\mathbf{S_v}$ and $\mathbf{U_v}$, the displacement fields are assumed to be polynomials. For example:

$$u_x = a_1 x^2 + b_1 xy + c_1 y^2 \tag{3.42}$$

$$u_y = a_2 x^2 + b_2 xy + c_2 y^2 \tag{3.43}$$

Substituting (3.44) and (3.45) into (3.40) and (3.41) gives:

$$\mu[2a_1 + 2c_1] + (\lambda + \mu)[2a_1 + b_2] = 0 \tag{3.44}$$

$$\mu[2a_2 + 2c_2] + (\lambda + \mu)[2c_2 + b_1] = 0 \tag{3.45}$$

These equations were then re-arranged for c_1 in (3.44) and a_2 in (3.45) and gave:

$$c_1 = -\frac{1}{2\mu}[4\mu a_1 + 2\lambda a_1 + \lambda b_2 + \mu b_2] \tag{3.46}$$

$$a_2 = -\frac{1}{2\mu}[4\mu c_2 + 2\lambda c_2 + \lambda b_1 + \mu b_1] \tag{3.47}$$

It must be noted, the terms c_1 and a_2 were chosen to ensure the overall complexity of the equations was reduced by the greatest amount for this particular case. However, the selection of these two variables, in general, can be considered to be arbitrary. If other variables had been chosen for this case the resulting stress approximations found for $\mathbf{S_v}$ would have be different, but would not have impacted the solutions that were found. Substituting these two equations back into (3.42) and (3.43) results in:

$$u_x = a_1 x^2 + b_1 xy - \frac{1}{2\mu}[4\mu a_1 + 2\lambda a_1 + \lambda b_2 + \mu b_2] y^2 \tag{3.48}$$

$$u_y = c_2 y^2 + b_2 xy - \frac{1}{2\mu}[4\mu c_2 + 2\lambda c_2 + \lambda b_1 + \mu b_1] x^2 \tag{3.49}$$

Equations 3.48 and 3.49 were then used to find the individual terms of $\mathbf{U_v}$. This process involved simplifying the above equations by setting a single unknown to one while all others were set to zero. This was done to ensure all individual terms were able to accurately describe the relevant displacement distributions within the element domain without any contribution

Variable Values		u	v
$a_1 = 1$	$b_1 = b_2 = c_2 = 0$	$x^2 - \frac{1}{\mu}[2\mu + \lambda]y^2$	0
$b_1 = 1$	$a_1 = b_2 = c_2 = 0$	xy	$-\frac{1}{2\mu}[\lambda + \mu]x^2$
$b_2 = 1$	$a_1 = b_1 = c_2 = 0$	$-\frac{1}{2\mu}[\lambda + \mu]y^2$	xy
$c_2 = 1$	$a_1 = b_1 = b_2 = 0$	0	$y^2 - \frac{1}{\mu}[2\mu + \lambda]x^2$

Table 3.1: Terms used in $\mathbf{U_v}$ matrix

Variable Value	σ_{xx}	σ_{yy}	σ_{xy}
$a_1 = 1$	$2x[2\mu + \lambda]$	$2\lambda x$	$-2y[2\mu + \lambda]$
$b_1 = 1$	$y[2\mu + \lambda]$	λy	$-\lambda x$
$b_2 = 1$	λx	$x[2\mu + \lambda]$	$-\lambda y$
$c_2 = 1$	$2\lambda y$	$2y[2\mu + \lambda]$	$-2x[2\mu + \lambda]$

Table 3.2: Terms used in $\mathbf{S_v}$ matrix

from the other terms in the equation. This ensured a general displacement field was able to be captured by a single term. The resulting equations that were produced were substituted into the equilibrium equations given in (3.40) and (3.41) to ensure equilibrium was achieved. These terms are shown in Table 3.1 and resulted in $\mathbf{U_v}$ taking the form:

$$\mathbf{U_v} = \begin{bmatrix} x^2 - \frac{1}{\mu}y^2[2\mu + \lambda] & xy & -\frac{1}{2\mu}y^2[\lambda + \mu] & 0 \\ 0 & -\frac{1}{2\mu}x^2[\lambda + \mu] & xy & y^2 - \frac{1}{\mu}x^2[2\mu + \lambda] \end{bmatrix} \tag{3.50}$$

The functions for $\mathbf{U_v}$ were then manipulated using (3.2) and (3.3) to obtain the functions for $\mathbf{S_v}$, shown in Table 3.2. Using (3.1), these functions were verified to ensure they satisfied equilibrium exactly within the element domain. Once the Trefftz functions were found (3.11) could be displayed fully as follows:

$$\begin{bmatrix} \sigma_{xx} \\ \sigma_{yy} \\ \sigma_{xy} \end{bmatrix} = \begin{bmatrix} 2x[2\mu + \lambda] & y[2\mu + \lambda] & \lambda x & 2\lambda y \\ 2\lambda x & \lambda y & x[2\mu + \lambda] & 2y[2\mu + \lambda] \\ -2y[2\mu + \lambda] & -\lambda x & -\lambda y & -2x[2\mu + \lambda] \end{bmatrix} \begin{bmatrix} a_1 \\ b_1 \\ b_2 \\ c_2 \end{bmatrix} \tag{3.51}$$

where a_1, b_1, b_2 and c_2 are the generalised stress degrees of freedom. While it was not applicable here, it is important to ensure that no two columns of $\mathbf{S_v}$ are linearly dependent. If this does occur, then one column must be deleted, along with the corresponding stress degree of freedom, to ensure that a unique solution to the system of equations can be obtained. It must be noted that the example outlined above is used to demonstrate how Trefftz functions are calculated for this particular approximation basis. As (3.35) must hold, these functions would only be applicable to problems where an element has a maximum of 4 displacement

degrees of freedom.

A more formal representation of this method is presented by Kompiš *et al.*[53], which can be used for general cases and has been applied to calculate Trefftz functions for 3D problems. This method also begins with the Lamé-Navier equations and considers a polynomial approximation of the displacement field to be:

$$\begin{bmatrix} u_x \\ u_y \\ u_z \end{bmatrix} = \begin{bmatrix} \mathbf{P}(\mathbf{x}) & 0 & 0 \\ 0 & \mathbf{P}(\mathbf{x}) & 0 \\ 0 & 0 & \mathbf{P}(\mathbf{x}) \end{bmatrix} \begin{bmatrix} \mathbf{C}^{(1)} \\ \mathbf{C}^{(2)} \\ \mathbf{C}^{(3)} \end{bmatrix} \tag{3.52}$$

where $\mathbf{P}(\mathbf{x})$ contains the polynomial of a given order, n:

$$\mathbf{P}(\mathbf{x}) = \left[1, x_1, x_2, x_3, \ldots, x_1^n, x_1^{n-1}x_2, \ldots, x_2x_3^{n-1}, x_3^n\right] \tag{3.53}$$

and $\mathbf{C}^{(i)}$ contains the unknown coefficients for these polynomials. This system of equations is then decomposed into two terms, where one contains terms which automatically satisfy the equilibrium condition (i.e. all the terms that have an order less than two), while the other contains all the higher order terms:

$$\begin{bmatrix} u_x \\ u_y \\ u_z \end{bmatrix} = \begin{bmatrix} \mathbf{V}^{(1)} & 0 & 0 \\ 0 & \mathbf{V}^{(2)} & 0 \\ 0 & 0 & \mathbf{V}^{(3)} \end{bmatrix} \begin{bmatrix} \mathbf{v}^{(1)} \\ \mathbf{v}^{(2)} \\ \mathbf{v}^{(3)} \end{bmatrix} + \begin{bmatrix} \mathbf{B}^{(1)} & 0 & 0 \\ 0 & \mathbf{B}^{(2)} & 0 \\ 0 & 0 & \mathbf{B}^{(3)} \end{bmatrix} \begin{bmatrix} \mathbf{b}^{(1)} \\ \mathbf{b}^{(2)} \\ \mathbf{b}^{(3)} \end{bmatrix} \tag{3.54}$$

where $\mathbf{B}$ contains the higher order terms and $\mathbf{V}$ the lower. It must be noted that the terms in $\mathbf{V}$ automatically satisfy the equilibrium condition but the terms in $\mathbf{B}$ cannot be arbitrary as they are the ones which must be specially designed to achieve this [54]. Equation 3.54 can then be substituted into the Lamé-Navier equation (i.e. the equilibrium equation) to give the following:

$$\begin{bmatrix} \mathbf{N}^{(1)} & 0 & 0 \\ 0 & \mathbf{N}^{(2)} & 0 \\ 0 & 0 & \mathbf{N}^{(3)} \end{bmatrix} \begin{bmatrix} \mathbf{v}^{(1)} \\ \mathbf{v}^{(2)} \\ \mathbf{v}^{(3)} \end{bmatrix} + \begin{bmatrix} \mathbf{M}^{(1)} & 0 & 0 \\ 0 & \mathbf{M}^{(2)} & 0 \\ 0 & 0 & \mathbf{M}^{(3)} \end{bmatrix} \begin{bmatrix} \mathbf{b}^{(1)} \\ \mathbf{b}^{(2)} \\ \mathbf{b}^{(3)} \end{bmatrix} = \begin{bmatrix} 0 \\ 0 \\ 0 \end{bmatrix} \tag{3.55}$$

where $\mathbf{M}$ and $\mathbf{N}$ contain the differentiated forms of $\mathbf{B}$ and $\mathbf{V}$ respectively which have been multiplied by the relevant Lamé co-efficients. This system of equations can then be solved for $\mathbf{b}$ which can be substituted into (3.54) to give an an expression for $\mathbf{U_v}$:

$$\mathbf{U_v} = \mathbf{V} - \mathbf{B}\mathbf{M}^{-1}\mathbf{N} \tag{3.56}$$

Again these functions could then be manipulated to find the expressions for $\mathbf{S_v}$ by applying (3.2) and (3.3):

$$\mathbf{S_v} = \mathbf{CL}(\mathbf{V} - \mathbf{BM}^{-1}\mathbf{N}) \tag{3.57}$$

The functions for $\mathbf{S_v}$ up to fourth order can be found in full in Appendix A of this thesis.

3.3 Numerical Integration

In the previous sections, the full formulation of the hybrid-Trefftz stress element has been outlined. In practice, when using this formulation, numerical integration will be performed to calculate all terms where required. In this thesis, standard Gaussian integration has been used to integrate over any element domains, Ω_e, and any element boundaries, Γ_e. It can be seen that the system of equations in (3.29) can be comprised of both volume and boundary integrals, or boundary integrals solely, depending on whether a volume or boundary integral is used for $\mathbf{F}$. The calculation of the volume integral is carried out in a similar manner to the classical finite element, where the Jacobian mapping between the global and local co-ordinate systems is calculated in the standard manner. However, the calculation for the Jacobian for the boundary integrals will now be outlined. In a standard tetrahedron, we can consider a set of local co-ordinates ξ, η and ζ in the standard curvilinear co-ordinate system. Generally, for a boundary integral it can be assumed that one of these local co-ordinates (here ζ) is constant. If we consider the boundary integral for $\mathbf{p}_\sigma$:

$$\mathbf{p}_\sigma = \int_{\Gamma_\sigma} \mathbf{U}_\Gamma^{\mathrm{T}} \bar{\mathbf{t}} \, \mathrm{d}\Gamma \tag{3.58}$$

then to calculate the Jacobian for this problem, we can consider $\mathrm{d}\Gamma$ to be equivalent to a vector which is normal to the surface of the element [109]. This can then be written as:

$$\mathrm{d}\Gamma = \mathbf{n}\mathrm{d}\xi\,\mathrm{d}\eta = \begin{bmatrix} \frac{\partial x}{\partial \xi} \\ \frac{\partial y}{\partial \xi} \\ \frac{\partial z}{\partial \xi} \end{bmatrix} \times \begin{bmatrix} \frac{\partial x}{\partial \eta} \\ \frac{\partial y}{\partial \eta} \\ \frac{\partial z}{\partial \eta} \end{bmatrix} \mathrm{d}\xi\,\mathrm{d}\eta \tag{3.59}$$

This means that the formula for the numerical integration of $\mathbf{p}_\sigma$ can be written as:

$$\mathbf{p}_\sigma = \sum_{i=1}^{nb} \mathbf{U}_\Gamma^{\mathrm{T}}(\xi_i, \eta_i)\, \bar{\mathbf{t}}\, \mathbf{n}(\xi_i, \eta_i)\, \mathrm{d}\xi\,\mathrm{d}\eta \tag{3.60}$$

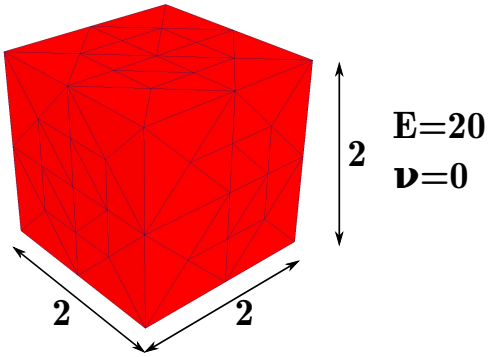

Figure 3.1: Numerical test layout

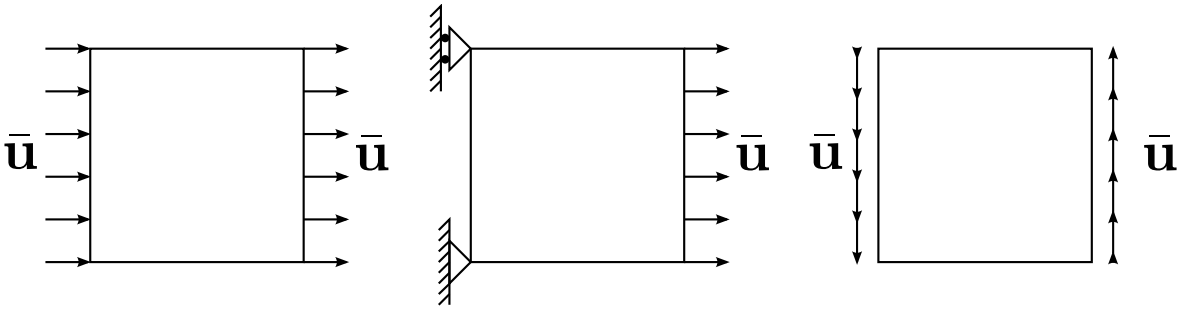

(a) Translational Loading (b) Tensile Loading (c) Shear Loading

Figure 3.2: Three loading situation for numerical tests

where *nb* is the number of integration points used on the face of the element. A similar procedure can be used for all other boundary integrals required in the formulation.

3.4 Numerical Tests

To validate the formulation three simple numerical tests were carried out on a 3D cube constructed of 10 noded tetrahedrons hybrid-Trefftz stress elements. For testing purposes, the stresses were approximated to the fourth order, which meant 54 generalised stress degrees of freedom per element were solved for on top of the 30 displacement degrees of freedom. The layout of the numerical problem, with material properties, can be seen in Figure 3.1. Three tests were performed on the cube to ensure the formulation could capture the correct response to rigid body translation, tensile loading and shear loading. The prescribed displacement fields are shown in Figure (3.2) for $\bar{\mathbf{u}} = 0.01$ in all cases. The results for relevant displacements, direct stresses and shear stresses are shown in Figures 3.3, 3.4 and 3.5.

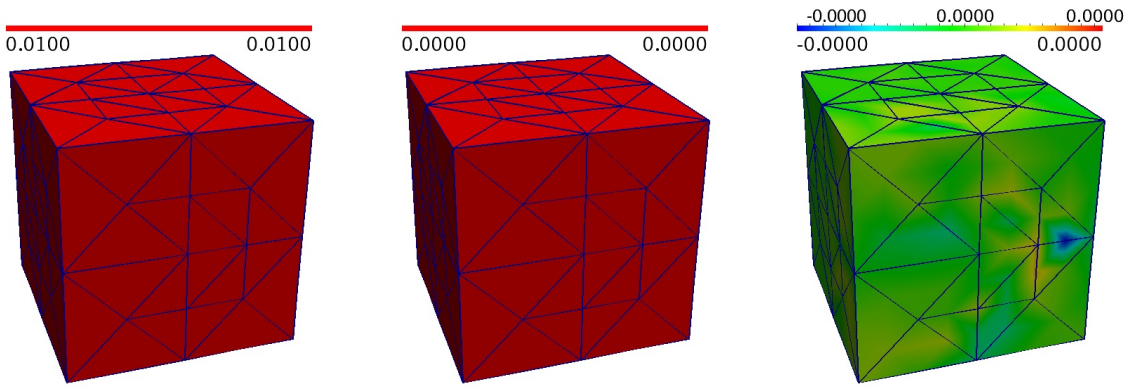

(a) X-Displacements (b) Y-Displacement (c) XX-Stress

Figure 3.3: Results for translational loading

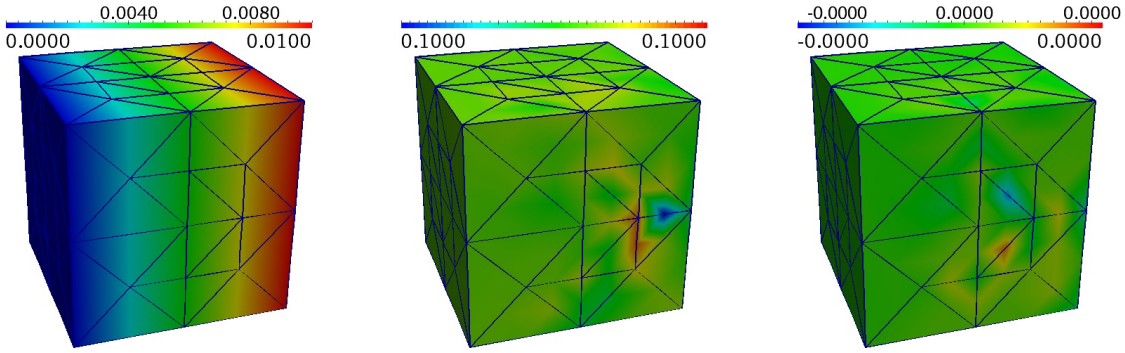

(a) X-Displacement (b) XX-Stress (c) XY-Stress

Figure 3.4: Results for tensile loading

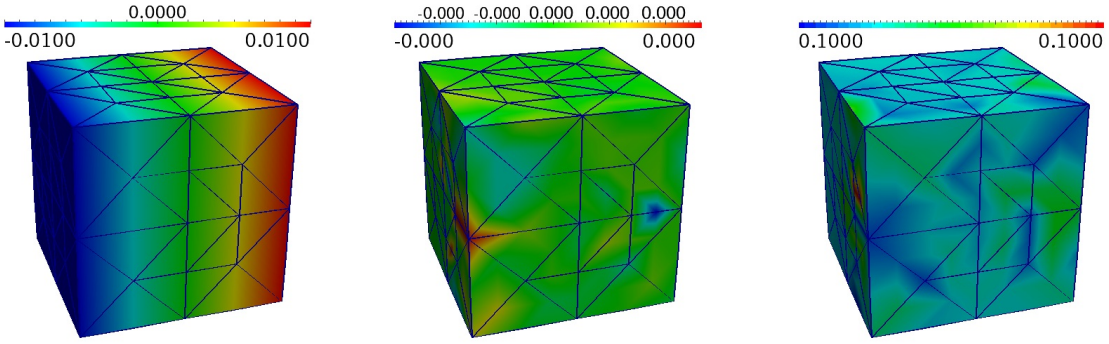

(a) Z-Displacement (b) ZZ-Stress (c) ZX-Stress

Figure 3.5: Results for shear loading

In all the cases presented, the element formulation behaved as expected. For the rigid body translation test, the model was able to capture the displacement of the cube and no stresses were generated, as expected. For the tensile loading test, the model accurately predicted the displacement distribution throughout the cube as well as the stresses present in the model. Figures 3.4b and 3.4c indicate there are very small discrepancies in the values of stress between elements (of the order of $1x10^{-8}$) due to the basic smoothing process for the stresses which has been used in the post processing of the results. The tests were repeated with a non-zero value of Poisson's ratio giving the correct results in all cases. In the shear loading test, it can be seen that the formulation was able to capture the non-zero value of shear in the XY direction while there were no principal stresses present. Again the values presented were confirmed using simple hand calculations to ensure overall correctness.

3.5 Conclusion

This Chapter has presented the formulation of the hybrid-Trefftz stress element which will be used in the rest of this thesis. A brief outline of the element type was discussed explaining how it differs to the classical displacement finite element as two different fields are present in a single element. In the hybrid-Trefftz stress element, the stresses are approximated over the volume of the element while the displacements are approximated over the element boundary. The formulation of the element is presented from the initial momentum balance equation and shows how the statics of the element are enforced in the strong sense, while the kinematics of the element are satisfied in the weak sense. The system of equations for the element is presented showing how static condensation can be used to allow a stiffness-like matrix, similar to that found in the classical displacement finite element, to be obtained. A demonstration of how the static formulation allows only boundary integrals to be carried out was also presented.

Within the hybrid-Trefftz stress element the approximation basis used is vitally important. As such, a method was presented which found the Trefftz functions for a simple 2D problem using second order approximations. This method was also presented in a more generalised format which could be used to find approximations for different problems in 3D and for higher order levels of approximation. Finally, simple numerical examples were outlined for validation purposes. These examples show that the elements perform as expected when subjected to rigid body translation, tensile and shear loading.

Chapter 4

Interface Element and Constitutive Law

This Chapter will present a methodology for modelling fracture at the mesoscale of concrete in 3D. Here, concrete will be considered a composite material, comprised of stiff aggregates embedded in a soft matrix with a weak interfacial transition zone (ITZ). Thus, the aggregate particles will be explicitly resolved by the finite element mesh. The elastic behaviour will be modelled by the hybrid-Trefftz stress elements discussed in the preceding Chapter. However, fractures will be modelled by continuous interface elements that are inserted between the hybrid-Trefftz stress elements. It can be assumed for all subsequent analyses that the bulk elements are linear-elastic and all non-linearity will occur in the continuous interface elements alone. The interface element used to model cohesive fracture will be discussed together with an appropriate constitutive model. Finally, separate simplified numerical tests will be presented, which will validate the interface element formulation and the application of the constitutive law presented.

4.1 Interface Elements in Fracture

As was discussed in Chapter 2, there are various different methods for modelling fracture, or damage, in heterogeneous materials such as concrete. The two main options used are smeared crack models or discrete crack models and both have been widely implemented in the literature. Here, a particular type of discrete crack model will be discussed where interface elements are utilised. Interface elements contain a non-linear constitutive law which relates the tractions across the crack face to the relative displacements of the crack. This allows the response of the material being analysed to be captured. This section will outline

the formulation of these interface elements from first principles and discuss any advantages or disadvantages associated with their implementation. It should be noted that the interface elements will be used to capture the non-linear behaviour of the concrete and it is assumed that the bulk elements contain a simple linear elastic constitutive law. The constitutive law which is used in the interface will be discussed in full in Section 4.2.

Interface elements can be considered to be zero thickness elements which connect two sides of a crack, or discontinuity, in a finite element mesh. To do this, two types of interface elements are widely used; continuous interface elements, which are used here, or nodal interface elements [80]. Nodal interface elements are more simple to implement and similar to a discrete spring element acting between nodes on either side of the crack. Continuous interface elements are more complicated but allow for a better description of the crack behaviour to be captured and require numerical integration over the crack face. Interface elements are used to describe the relationship between the tractions and relative displacements (or crack width) and this is done at each integration point on the face for continuous interface elements. In both cases, an interface element can be viewed as connecting two distinct faces on each side of the crack as shown in Figure 4.1. In the work presented here, 10-noded tetrahedrons are

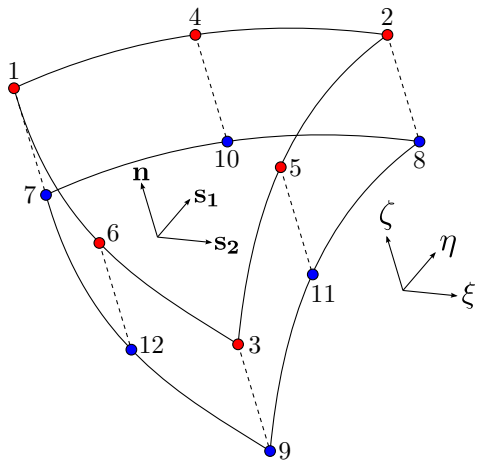

Figure 4.1: General interface element

used for the bulk elements together with 6-noded continuous interface elements. A local co-ordinate system, used in this thesis, is defined where **n** is the normal direction to the crack face and $\mathbf{s_1}$ and $\mathbf{s_2}$ are the tangential directions to the face.

4.1.1 Element Formulation

In Figure 4.1 the upper face, $+$, can be identified by the red nodes while the lower face, $-$, can be denoted by the blue nodes and this interface element connects two bulk elements, Ω^+ and Ω^-. For each face, a displacement vector can be constructed as follows:

$$\mathbf{q}^+_{\text{face}} = \left[q^1_x, q^1_y, q^1_z, \ldots, q^6_x, q^6_y, q^6_z\right]^{\mathrm{T}} \tag{4.1}$$

$$\mathbf{q}^-_{\text{face}} = \left[q^7_x, q^7_y, q^7_z, \ldots, q^{12}_x, q^{12}_y, q^{12}_z\right]^{\mathrm{T}} \tag{4.2}$$

where q^i_x, q^i_y and q^i_z are the displacement values for node i in the standard global Cartesian system and $+$ and $-$ signify the upper and lower faces of the interface element. To find the displacement value of any point on the face, $\mathbf{q}_i$, the matrix $\mathbf{U}_\Gamma$ containing the standard isoparametric shape functions is used:

$$\mathbf{q}_i^{+,-}(\xi_i, \eta_i) = \mathbf{U}_\Gamma(\xi_i, \eta_i)\, \mathbf{q}^{+,-}_{\text{face}} \tag{4.3}$$

where ξ_i and η_i are the standard natural element co-ordinates for point i, which range from 0 to 1. The matrix $\mathbf{U}_\Gamma$ takes the form shown in (3.20) on page 32. While the same approximation basis for displacements has been used for both sides of the crack face, this does not necessarily need to be the case [52]. As mentioned previously, the constitutive relationships used in interface elements relate the tractions and relative displacements across the interface. This relationship exists in the local co-ordinate system, shown in Figure 4.1, where the relative displacements at a point are given by:

$$\mathbf{g}_i^{loc}(\xi, \eta) = \begin{bmatrix} g_n \\ g_{s_1} \\ g_{s_2} \end{bmatrix} = \begin{bmatrix} \mathbf{n}^+ \cdot \mathbf{q}_i^+ - \mathbf{n}^+ \cdot \mathbf{q}_i^- \\ \mathbf{s_1}^+ \cdot \mathbf{q}_i^+ - \mathbf{s_1}^+ \cdot \mathbf{q}_i^- \\ \mathbf{s_2}^+ \cdot \mathbf{q}_i^+ - \mathbf{s_2}^+ \cdot \mathbf{q}_i^- \end{bmatrix} \tag{4.4}$$

where the unit normal $\mathbf{n}$ of the given face is:

$$\mathbf{n} = \frac{1}{\left\| \frac{\partial \mathbf{x}_i}{\partial \xi} \times \frac{\partial \mathbf{x}_i}{\partial \eta} \right\|} \left[\frac{\partial \mathbf{x}_i}{\partial \xi} \times \frac{\partial \mathbf{x}_i}{\partial \eta} \right] \tag{4.5}$$

and the unit vectors in the tangential directions are:

$$\mathbf{s_1} = \frac{1}{\left\| \frac{\partial \mathbf{x}_i}{\partial \xi} \right\|} \frac{\partial \mathbf{x}_i}{\partial \xi} \tag{4.6}$$

$$\mathbf{s_2} = \mathbf{n} \times \mathbf{s_1} \tag{4.7}$$

where

$$\frac{\partial \mathbf{x}_i}{\partial \xi} = \begin{bmatrix} \frac{\partial x_n}{\partial \xi} \\ \frac{\partial x_{s_1}}{\partial \xi} \\ \frac{\partial x_{s_2}}{\partial \xi} \end{bmatrix} = \begin{bmatrix} \sum_{i=1}^{n} \frac{\partial N_i}{\partial \xi} x_n^i \\ \sum_{i=1}^{n} \frac{\partial N_i}{\partial \xi} x_{s_1}^i \\ \sum_{i=1}^{n} \frac{\partial N_i}{\partial \xi} x_{s_2}^i \end{bmatrix} \quad \& \quad \frac{\partial \mathbf{x}_i}{\partial \eta} = \begin{bmatrix} \frac{\partial x_n}{\partial \eta} \\ \frac{\partial x_{s_1}}{\partial \eta} \\ \frac{\partial x_{s_2}}{\partial \eta} \end{bmatrix} = \begin{bmatrix} \sum_{i=1}^{n} \frac{\partial N_i}{\partial \eta} x_n^i \\ \sum_{i=1}^{n} \frac{\partial N_i}{\partial \eta} x_{s_1}^i \\ \sum_{i=1}^{n} \frac{\partial N_i}{\partial \eta} x_{s_2}^i \end{bmatrix} \tag{4.8}$$

where n is the number of nodes in the interface element. In (4.4), only $\mathbf{n}$, $\mathbf{s_1}$and $\mathbf{s_2}$ for the upper face are used. This ensures the relative displacement in the normal direction is always positive, which is of paramount importance when examining the constitutive laws which will be discussed later.

As with the hybrid-Trefftz stress elements outlined in Chapter 3, the formulation of the interface element was carried out in such a way to ensure that all integrals in the formulation had the dimension of work. If we consider the face of an element which is a crack face, the internal work due to the tractions from the interface element, Γ_{cr}, can be written as:

$$IW = \int_{\Gamma_{\text{cr}}} \mathbf{w}_3^{\text{T}} \mathbf{t} \, \text{d}\Gamma \tag{4.9}$$

where $\mathbf{w_3}$ is an appropriate weighting function, $\mathbf{t}$ is a vector containing the tractions on the interface in the global co-ordinate system and IW is the internal work of the interface. When using interface elements, the constitutive laws used to relate the tractions across the interface to the relative displacements is formulated in the local co-ordinate system shown in Figure 4.1. Therefore the tractions in the local co-ordinate system, $\mathbf{t}^{loc}$, can be written as:

$$\mathbf{t}^{loc} = \begin{bmatrix} t_n \\ t_{s_1} \\ t_{s_2} \end{bmatrix} \tag{4.10}$$

where t_n is the traction in the direction normal to the face and t_{s_1} and t_{s_2} are the tractions in the tangential directions. Due to the constitutive law being applied in the local co-ordinate system of the interface element a rotation matrix, $\mathbf{R}$, must be applied to allow the local tractions to be expressed in the global co-ordinate system. This can be written as:

$$IW = \int_{\Gamma_{\text{cr}}} \mathbf{w}_3^{\text{T}} \mathbf{R}^{\text{T}} \mathbf{t}^{loc} \, \text{d}\Gamma \tag{4.11}$$

where $\mathbf{R}$ takes the form:

$$\mathbf{R} = \begin{bmatrix} \mathbf{n}^{\mathrm{T}} \\ \mathbf{s_1}^{\mathrm{T}} \\ \mathbf{s_2}^{\mathrm{T}} \end{bmatrix} \tag{4.12}$$

To ensure that the integral has the unit of work as required, the weighting function was chosen to be:

$$\mathbf{w}_3 = \mathbf{U}_\Gamma \mathbf{v}_{cr} \tag{4.13}$$

where $\mathbf{U}_\Gamma$ contains the approximation functions for the boundary element, which takes the form shown in (3.20), and $\mathbf{v}_{cr}$ contains the discrete values of the weighting function. In the problems being analysed, $\mathbf{U}_\Gamma$ uses the isoparametric shape functions for a 6-noded triangle as its approximation functions, but this need not necessarily be the case. The use of this weighting function means that the internal force vector of the interface element, $\mathbf{f}_{\mathrm{cr}}^{\mathbf{int}}$, can be written as:

$$\mathbf{f}_{\mathrm{cr}}^{\mathbf{int}} = \int_{\Gamma_{\mathrm{cr}}} \mathbf{U}_\Gamma^{\mathrm{T}} \mathbf{R}^{\mathrm{T}} \mathbf{t}^{loc} \, \mathrm{d}\Gamma \tag{4.14}$$

Here, $\mathbf{t}^{loc}$ can be described in a manner which relates it to the relative displacements of the crack as follows:

$$\mathbf{t}^{loc} = \mathbf{D}(\mathbf{g})\mathbf{g} \tag{4.15}$$

where $\mathbf{D}(\mathbf{g})$ is the 3x3 matrix containing the constitutive relationship of the interface element. The stiffness matrix of the interface element, $\mathbf{K_{cr}}$, can be used to relate the displacement degrees of freedom, $\mathbf{q}$, to the internal force vector using the following:

$$\mathbf{f}_{\mathrm{cr}}^{\mathbf{int}} = \mathbf{K_{cr}}\mathbf{q} \tag{4.16}$$

and by using (4.14), and substituting in (4.15), it is possible to obtain $\mathbf{K_{cr}}$ given by:

$$\mathbf{K_{cr}} = \int_{\Gamma_{\mathrm{cr}}} \mathbf{U}_\Gamma^{\mathrm{T}} \mathbf{R}^{\mathrm{T}} \mathbf{D}(\mathbf{g}) \mathbf{R} \mathbf{U}_\Gamma \, \mathrm{d}\Gamma \tag{4.17}$$

The constitutive relationship embedded within $\mathbf{D}(\mathbf{g})$ used in the interface element formulation will be discussed in detail in Section 4.2.

4.1.2 Interface and Hybrid-Trefftz Stress Elements

In the hybrid-Trefftz stress element formulation, outlined in Chapter 3, the kinematics were satisfied in the weak sense by (3.28) which was found by taking the weak form of the element continuity equation. If it is assumed that no prescribed displacements are applied to the interface element, then this equation can be modified to include the interface element contribution in the formulation as follows:

$$\int_{\Omega^+} \mathbf{S}_{\mathbf{v}}^{\mathrm{T}} \mathbf{C} \mathbf{S}_{\mathbf{v}} \mathbf{v}^+ \, \mathrm{d}\Omega - \int_{\Gamma^+} (\mathbf{N}\mathbf{S}_{\mathbf{v}})^{\mathrm{T}} \mathbf{U}_{\Gamma} \mathbf{q}^+ \, \mathrm{d}\Gamma - \int_{\Gamma_{cr}} (\mathbf{N}\mathbf{S}_{\mathbf{v}})^{\mathrm{T}} \mathbf{U}_{\Gamma} \mathbf{q}^+_{face} \, \mathrm{d}\Gamma = 0 \tag{4.18}$$

When using the notation in Chapter 3 this can be written in matrix form as:

$$\mathbf{F}^+ \mathbf{v}^+ - (\mathbf{A}^+)^{\mathrm{T}} \mathbf{q}^+ - (\mathbf{A}^+_{\mathrm{face}})^{\mathrm{T}} \mathbf{q}^+_{\mathrm{face}} = 0 \tag{4.19}$$

with a further, and similar, equation describing the kinematics of the element on the other side of the crack, Ω^-:

$$\mathbf{F}^- \mathbf{v}^- - (\mathbf{A}^-)^{\mathrm{T}} \mathbf{q}^- - (\mathbf{A}^-_{\mathrm{face}})^{\mathrm{T}} \mathbf{q}^-_{\mathrm{face}} = 0 \tag{4.20}$$

The enforcement of these equations allow a full description of the compatibility of displacements over the interface element to be obtained. The compatibility of displacements over the element is enforced in the weak integral sense using these equations due to the formulation outlined. As can be seen in (4.19) and (4.20), for both the upper and lower faces the compatibility is enforced separately. The is an advantage which will be further discussed when considering the implementation of a crack insertion algorithm in Chapter 5.

It was also possible to frame the enforcement of statics across an element boundary in such a way to investigate the implementation of interface elements into the formulation. In this case the traction boundary condition is enforced in a strong integral sense. This too can be enforced independently for the upper and lower faces and if there is no discontinuity, and thus no interface element, the following equation describes this condition:

$$\int_{\Gamma^+} \mathbf{U}_{\Gamma}^{\mathrm{T}} \mathbf{N} \mathbf{S}_{\mathbf{v}} \mathbf{v}^+ \, \mathrm{d}\Gamma + \int_{\Gamma^-} \mathbf{U}_{\Gamma}^{\mathrm{T}} \mathbf{N} \mathbf{S}_{\mathbf{v}} \mathbf{v}^- \, \mathrm{d}\Gamma = 0 \tag{4.21}$$

which can then be written in matrix format as:

$$\mathbf{A}^+_{\mathrm{face}} \mathbf{v}^+ + \mathbf{A}^-_{\mathrm{face}} \mathbf{v}^- = 0 \tag{4.22}$$

If there is a discontinuity and an interface element is present, (4.22) must be modified to ensure that traction continuity is achieved. If we take the interface stiffness matrix $\mathbf{K_{cr}}$ from (4.17), then in matrix form the modified equation can be written as:

$$\mathbf{A}^{+}_{\text{face}}\mathbf{v}^{+} + \mathbf{K_{cr}}\mathbf{q}^{+} - \mathbf{K_{cr}}\mathbf{q}^{-} = 0 \tag{4.23}$$

$$\mathbf{A}^{-}_{\text{face}}\mathbf{v}^{-} - \mathbf{K_{cr}}\mathbf{q}^{+} + \mathbf{K_{cr}}\mathbf{q}^{-} = 0 \tag{4.24}$$

These equations ensure traction continuity is maintained throughout the mesh when interfaces are included.

4.1.3 Interface Elements and Traction Oscillations

It has been noted in the literature that the use of interface elements led to oscillations in the traction field when solving the non-linear system of equations [80]. It should be noted that it was common practice to include interface elements *a priori* at every interface in the mesh, rather than add them dynamically, as and when required, as is proposed in this thesis. Continuity of the initial elastic continuum was enforced by the use of a "penalty" stiffness in the interface element. Once a crack was initiated, the penalty stiffness would be removed and a non-linear law relating the tractions and relative displacements across the interface was adopted [36, 52, 69, 84]. It was initially suggested that the reason for the oscillations in the traction field was because of the high initial penalty stiffness used.

Schellekens and de Borst [80] examined the influence of using different numerical integration schemes and demonstrated that there were several different situations where interface elements were not performing in a satisfactory manner. First, it was found that the traction oscillations were not a direct result of using the penalty stiffness but occurred due to the large traction gradients they induced. These large gradients could not be accurately captured using the given integration schemes and could only be solved by increasing mesh refinement in these areas. Analyses were carried out using both Gaussian integration and Newton-Cotes/Lobatto integration scheme for both linear and quadratic elements to test the effectiveness of the different methods. It was found that when using linear interface elements, both the Gaussian and Newton-Cotes/Lobatto integration schemes caused traction oscillations to occur. When using quadratic interface elements, Gaussian integration still caused traction oscillations but this was not the case for certain situations when using the

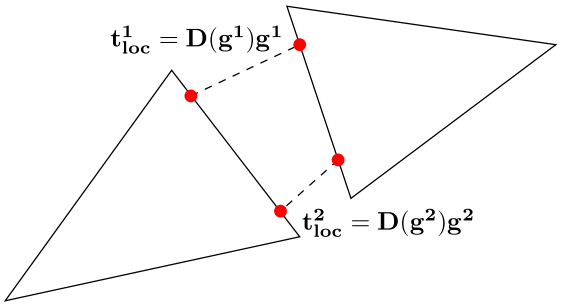

Figure 4.2: 2D interface element highlighting spatial variation of relative displacements

Newton-Cotes/Lobatto scheme. If the gradient of the displacement field across the interface was in the direction of one of the principal local directions, ξ or η, then there were no traction oscillations. This was because the Newton-Cotes/Lobatto scheme used an integration point in the centre of the interface element which was only dependent on the displacement values of nodes where there was no displacement gradient. Outside of this special case the Newton-Cotes/Lobatto scheme still produced traction oscillations and it was found that the problem was only solved if "severe" mesh refinement was employed. The overall conclusion of the paper was that the integration scheme used did perform under certain situations but care must be taken when selecting both the correct scheme and the level of approximations used.

While the work carried out by Schellekens and de Borst provided a detailed explanation for the observed traction oscillations and suggested possible remedies, there was still some work required to try and overcome the limitations present in interface elements with regards to this issue. A fundamental flaw when using interface elements is apparent when the approximation basis of both the interface and a classical finite element is examined. In classical finite elements, there is a single approximation basis over an element to describe the displacements which is used to calculate the strains, these are then related to the stresses by a constitutive law. This relationship means that the stress state in an element will always be described by an approximation that is one order less than that used to describe the displacements. As such, in classical finite elements when a linear approximation basis is used for the displacements the stresses are constant. However, when interface elements are used with these classical finite elements, the stress, or traction, approximation along the interface is not constant. In general, the relative displacements will vary along an interface element. Thus, the traction field will also vary as they are related via a constitutive law, which is typically non-linear, and this is illustrated in Figure 4.2 for linear elements. This causes an inherent inconsistency in the finite element solution as the stress state in the neighbouring bulk finite elements may

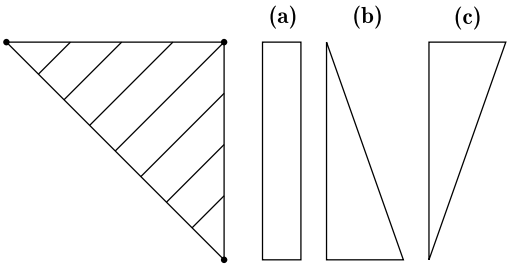

Figure 4.3: Example of inconsistency in stresses when using interface elements

not match the traction field in the interface element. This inconsistency is at the root of the traction oscillation problem when using interface elements. The phenomenon can be further highlighted by Figure 4.3, which shows three different tractions states that could be present in the interface element in (a), (b) and (c). Due to the level of approximation in the finite element it would not be possible to determine which stress state of (a), (b) or (c) is the actual solution as the average of the three states is the same. The work in this thesis overcomes the traction oscillation issue by utilising hybrid-Trefftz stress elements.

When using hybrid-Trefftz stress elements the stresses in the element domain are able to be approximated to a much higher order, without the need to increase the order of approximation of the displacements on the boundary. In the numerical tests shown in Chapter 3, the stresses were approximated to the fourth order but, by designing the Trefftz functions properly, even higher orders can be used. This means that, when using hybrid-Trefftz stress elements with interface elements, there is no significant inconsistency between the values of stress at the integration point as the element and the interface element are of a sufficiently high order of approximation to capture the stress profile.

4.2 Constitutive Law

Interface elements have been used to model the non-linear response due to cracking in different materials. In concrete, this was achieved by implementing different constitutive laws which were developed to ensure the correct material response was captured. The material response of concrete has been found to be quasi-brittle in nature. This means that the Fracture Process Zone (FPZ) of the material is much larger than in the case of brittle materials and this phenomena is demonstrated in Figure 4.4. The Fracture Process Zone can be defined as the zone in which there is degradation of the material and fracturing is taking place. In con-

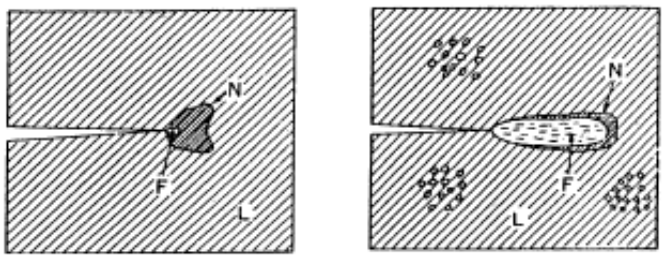

(a) Brittle Material (b) Quasi-brittle Material

Figure 4.4: Fracture Process Zone of brittle material and quasi-brittle material - F signifies the fracture process zone, N signifies an area where non-linear behaviour is occuring and L signifies the area where linear-elastic behaviour occurs [11]

crete, this degradation is characterised by cracking occurring at the lower scales before the cracks coalesce and join to form macrocracks in the specimen. Interface elements have been used to capture this process in the continuum setting by using Hillerborg's Fictitious Crack Model [41]. This methodology was used to model concrete at the macroscale and assumed that all cracking which occurs in the meso or microscale could be lumped into a single crack. This process can also be known as the cohesive crack model and its basic hypothesis is that the FPZ can be described by this single crack which allows the transmission of tractions, $\mathbf{t}$, across the crack which are dependent on the relative displacement, or width, of the crack, $\mathbf{g}$.

In the work in this thesis, the analyses will be performed at the mesoscale but the use of the Fictitious Crack Model is deemed appropriate. At the mesoscale, it is still possible to lump all the cracking which is taking place at the microscale into a single crack and use the Fictitious Crack Model to capture the material behaviour. This theory can be supported by the microstructure of concrete presented in Figure 4.5. It can be seen that, even at smaller scales, due to the microstructure of concrete, cracks will appear which will not be visible at the mesoscale. The picture also demonstrates why the methodology is being developed where aggregate particles are explicitly resolved by the finite element mesh. As the ITZ is not smooth and is essentially the transition stage between the aggregate and the surrounding cement paste, stress concentrations and microcracking are likely to begin here. This is because the ITZ contains both asperities and voids as expected and the behaviour here can be modelled by a single crack with an appropriate constitutive law.

When using the lumped single crack, the constitutive law must be able to capture the correct non-linear response of the material due to the presence of the physical phenomena, such as

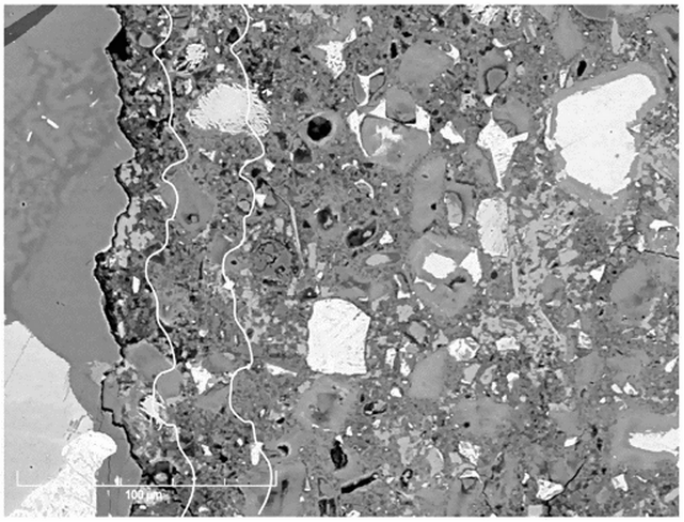

Figure 4.5: Microstructure of concrete showing the interfacial transition zone between the bulk matrix and an aggregate piece - The ITZ is signified as the area between the two white lines and the aggregate piece is the large solid shape on the left of the picture [82]

asperities or voids shown in Figure 4.5, but which will not be explicitly modelled. This is vitally important as it is believed that the immediate zones around aggregate particles can constitute up to 20-30% of the entire cement paste in the concrete specimen [83]. In computational mechanics this process has been achieved by developing material models which accurately simulate the observed experimental behaviour [33]. For zero-thickness interface elements, which are used here, the convention is to use constitutive laws which are unrelated to the material properties of the bulk elements but produce appropriate results [103].

The constitutive models used in problems where interface elements are implemented can be broadly described as being based on the damage concept or based on pure plasticity. The constitutive model which will be outlined here was developed by Winnicki [105] to model fracture in concrete in 3D. When choosing a constitutive model to implement there were several requirements which had to be met. First, the model had to be able to capture mixed mode fracture which, in general, would be prevalent in the types of analyses which were going to be performed. Second, it should be computationally robust to ensure the overall computational solution scheme was stable and efficient. Finally, it should be as simple a law as possible while still ensuring the physical phenomena appropriate to concrete were being taking into consideration. It is believed that the Winnicki law implemented fulfills these requirements and thus was suitable for use in the computational framework.

The work presented in the following section will initially focus on describing the constitutive law developed by Winnicki and underline its suitability for use in analysing concrete. The implementation of a plasticity law into the overall computational framework will be discussed and its advantages over other laws will be given.

4.2.1 Winnicki Constitutive Law

The Winnicki model is a plasticity based approach which adopts a yield surface that can be considered to be an evolution of the Mohr-Coulomb yield surface. The evolution from the Mohr-Coulomb yield surface was carried out to better describes the behaviour of concrete, as the Mohr-Coulomb law struggles to capture pure Mode I fracture. As the yield surface is not smooth, under purely tensile loading a normal (and therefore the direction of plastic flow) would not be able to be defined. However, this issue has been overcome by converting the Mohr-Coulomb law into a yield surface which is hyperboloidal in 3D, which ensures the yield surface is smooth [23, 58]. Winnicki further modified the shape of the yield surface to be paraboloidal given by:

$$F(\mathbf{t},\kappa) = t_n + \frac{C_0}{B^2(\kappa)}\left(t_{s_1}^2 + t_{s_2}^2\right) - C(\kappa) \tag{4.25}$$

which was suggested as being more appropriate for concrete. Here, t_n is the traction in the normal direction to the interface, t_{s_1} and t_{s_2} are the tractions in the tangential direction to the interface, C_0 is the ultimate tensile strength of the material, κ is a degradation parameter and $C(\kappa)$ and $B(\kappa)$ are the current strengths of the material in the normal and tangential directions respectively when degradation of the material is considered. The paraboloidal shape of the yield surface was deemed to be more appropriate because it allowed experimental results to be captured more accurately for cases where large values of compressive normal stresses would reduced the asperities within the concrete. This, in turn, reduced the internal friction angle which can be captured by the degraded yield surface shown in Figure 4.6 in 2D. While the investigations carried out in this report focus on mixed mode fracture, this demonstrates that the yield surface has been designed to be able to capture the behaviour of concrete in compressive loading situations.

Figure 4.7 demonstrates how the yield surface evolves when the parameters of $C(\kappa)$ and $B(\kappa)$ reduce from the ultimate tensile and shear strengths of the material. Figure 4.7a demonstrates the case of Mode I fracture where no reduction is shear capacity is allowed. As can been seen

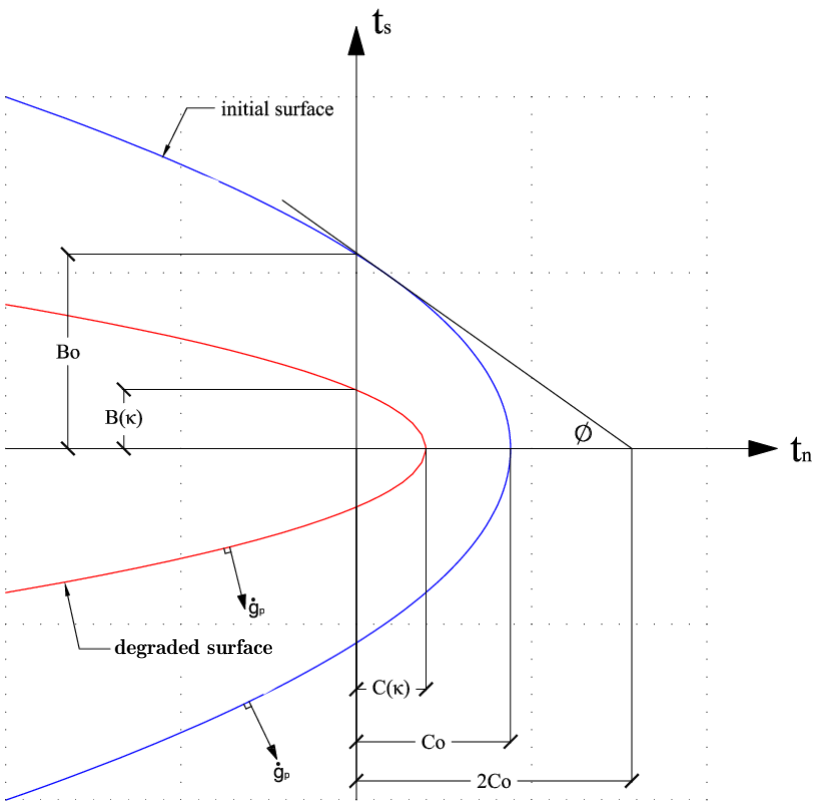

Figure 4.6: Winnicki yield surface in 2D [105]

the yield surface simply shifts to the left in this case with the tensile capacity of the material being reduced. This means that there will be no change in the value of combined compressive and shear loading the material could take in this case. Figure 4.7b shows the case of Mode II fracture where the tensile capacity of the material does not reduce. Here, the meridians reduce but there is no shift to the left for the yield surface. Finally, Figure 4.7c shows the most likely load case of Mixed Mode fracture, which will be implemented in future analyses. Here, there is a shift to the left and the envelope encased by the meridians reduces, showing the coupling of degradation between the normal and shear directions. This final case is what is expected in concrete. These graphs demonstrate the ability of the yield surface to evolve due to the applied load case and how separate laws could be implemented to capture different reductions in the shear and tensile capacities simple by changing $C(\kappa)$ and $B(\kappa)$ respectively.

As was shown in Section 4.1.1, the tractions present in the interface are related to the relative displacement across the interface, $\mathbf{g}$, by a constitutive relationship, in this case the Winnicki law. However, as the Winnicki model is a type of pure plasticity constitutive law, it is as-

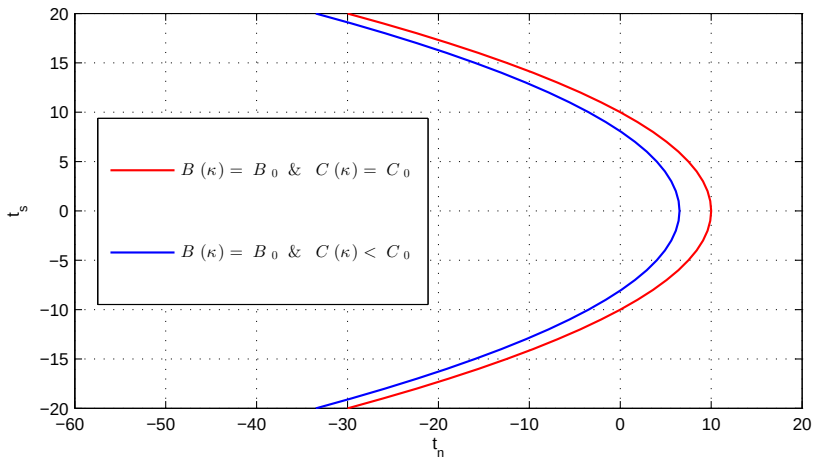

(a) Mode I fracture

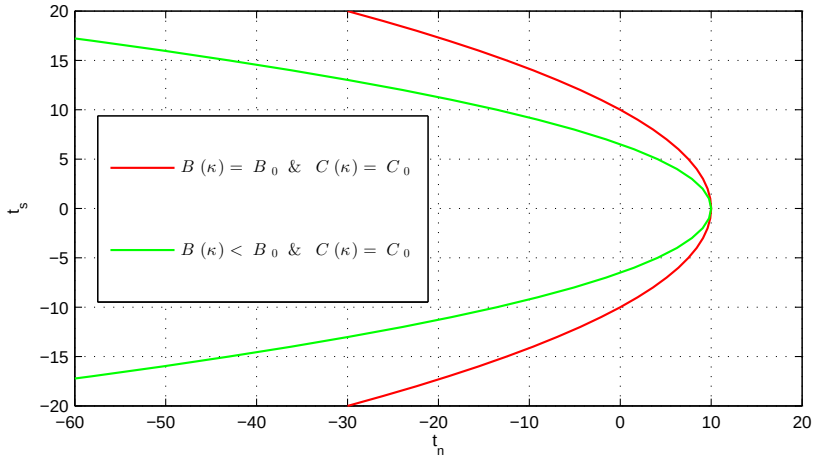

(b) Mode II fracture

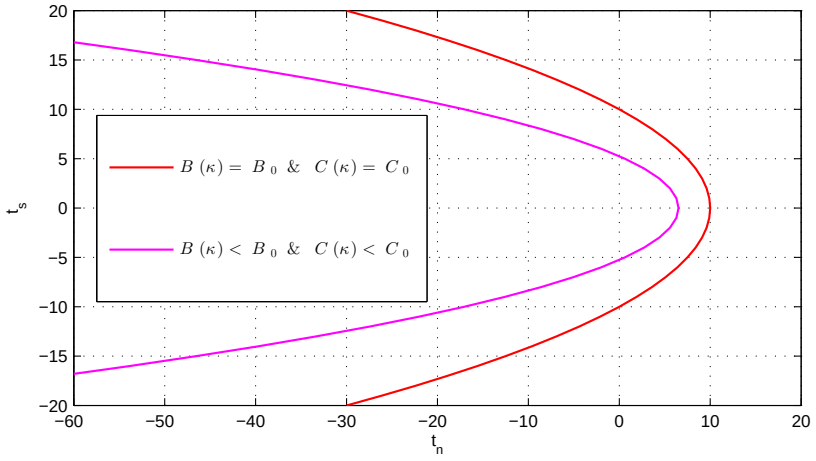

(c) Mixed Mode fracture

Figure 4.7: Yield surface evolution for different scenarios

sumed that the total relative displacement can be additively decomposed:

$$\mathbf{g} = \mathbf{g_e} + \mathbf{g_p} \tag{4.26}$$

where $\mathbf{g_e}$ is the elastic (reversible) relative displacement and $\mathbf{g_p}$ is the plastic (irreversible) relative displacement. The traction vector, $\mathbf{t}^{loc}$, can be related to the elastic relative displacements by the following relationship:

$$\mathbf{t}^{loc} = \mathbf{D^e g_e} = \mathbf{D^e}\left(\mathbf{g} - \mathbf{g_p}\right) \tag{4.27}$$

where

$$\mathbf{D^e} = \begin{bmatrix} \frac{E_n^{int}}{h} & 0 & 0 \\ 0 & \frac{E_{s_1}^{int}}{h} & 0 \\ 0 & 0 & \frac{E_{s_2}^{int}}{h} \end{bmatrix} \tag{4.28}$$

The matrix $\mathbf{D^e}$ is the elastic stiffness matrix of the interface element and contains values for the normal and tangential stiffness for the interface element. It should be noted that while h, which can be considered the interface thickness, is included in the terms of $\mathbf{D^e}$ it is not actually used to calculate a value for the elastic stiffness of the interface. The value that is used for this parameter is user defined but this terminology must be used to ensure the units of the elastic stiffness of the interface element are consistent. As can be seen, this stiffness matrix prevents any coupling between the normal and tangential components and this is consistent with ensuring that there is zero dilatancy in the elastic behaviour of the interface. As zero thickness interface elements are being used, it is vital that the discontinuity of displacements between two neighbouring finite elements is minimised and the overall elastic response is not altered due to their inclusion. To achieve this, penalty stiffness terms are used for E_i^{int} in (4.28). Theoretically, for the continuity of displacements to be maintained the value of this penalty stiffness should be infinity. However, this is not possible as it would cause the solution scheme to become numerically unstable. Therefore, careful consideration must be given to the selection of the penalty stiffness used to ensure it is high enough to produce results which maintain continuity of displacements as closely as possible. However, it must also be low enough to ensure the global stiffness matrix does not become ill-conditioned. There have been various attempts to formalise the value which should be used, such as stating it should be roughly three orders of magnitude bigger than the value of Young's modulus used for the bulk material [39] or by trying to relate it to the constitutive model used to capture softening in the interface [62]. However, these approaches did not present exact answers for how the values for the penalty should be selected and ultimately the value is problem specific.

In the conventional use of interface elements, where they are *a priori* inserted into the mesh before the analysis begins, this penalty stiffness obviously plays an important role. In this thesis, discrete cracks will be dynamically inserted into the finite element mesh as and when required, but the penalty stiffness will still be utilised. In the analyses performed, where the crack direction is not predefined and numerous cracks can appear, there is a possibility that some interface elements will unload and behave elastically. In these cases the interface elements will not be dynamically removed from the mesh and the penalty stiffness will be required to ensure continuity of displacements between elements is achieved.

4.2.2 Evolution of the Plastic Surface

This section outlines how the evolution of the yield surface was captured for concrete using appropriate equations. These equations contain several user defined variables which will be discussed in terms of their effect on the response of the material. A full discussion on the tuning of these parameters for use in realistic problems will be given in Chapter 7.

The yield function defined in (4.25) was developed to take account of the physical phenomena in concrete but also required the inclusion of a softening law to allow the non-linear behaviour and reduction in the material's ability to carry load to be captured . The softening of the material is governed by the evolution terms, $B(\kappa)$ and $C(\kappa)$ in (4.25), which take the form:

$$C(\kappa) = (C_0 - C_u)\exp\left(-(\alpha\kappa)^{\gamma_1}\right) + C_u \tag{4.29}$$

$$B(\kappa) = (B_0 - B_u)\exp\left(-(\beta\kappa)^{\gamma_2}\right) + B_u \tag{4.30}$$

where C_0 and B_0 are the ultimate tensile and shear strengths of the material, C_u and B_u are the residual strengths of the material in tension and shear respectively and κ is a degradation parameter which is a measure of the equivalent relative plastic displacements across the interface given by:

$$\kappa = \left\|\mathbf{g_p}\right\| = \sqrt{\left(g_p^n\right)^2 + \left(g_p^{s_1}\right)^2 + \left(g_p^{s_2}\right)^2} \tag{4.31}$$

The rest of the variables were user defined variables which could be tuned to allow the correct material response to be obtained. Clearly, these variables can be used to alter the response of concrete, so it could be suggested that the application of these equations produces a somewhat phenomenological response. This means that some tuning would be required to find realistic values for these variables. Figures 4.8 and 4.9 demonstrate the effect changing

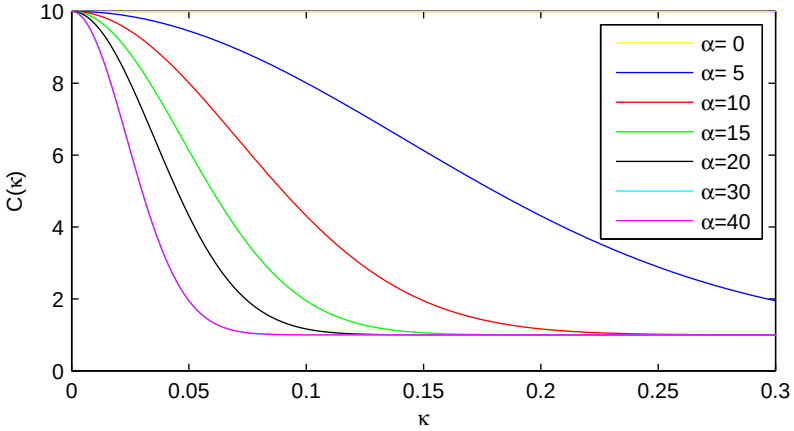

Figure 4.8: Response of softening law due to variation of α

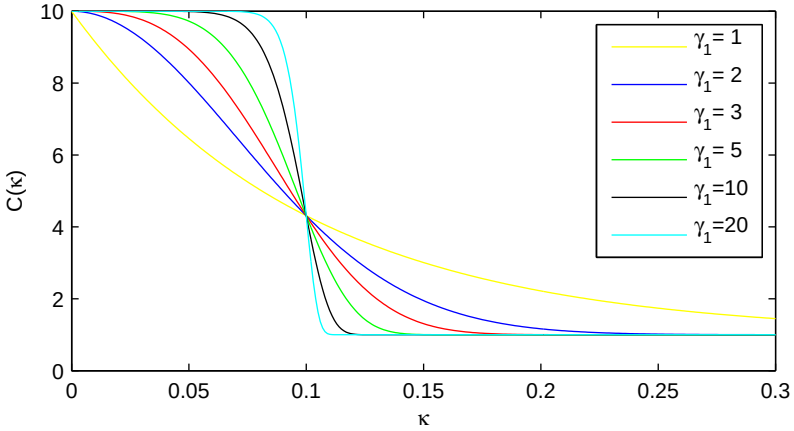

Figure 4.9: Response of softening law to variation of γ_1

the values of α and γ_1 has on the pattern of $C(\kappa)$. In these tests $C_0 = 10$ and $C_u = 1$ and identical curves would be obtained when varying β and γ_2 in $B(\kappa)$ if the same values were used for B_0 and B_u. From the results presented, it can be seen that α (and therefore β) control the amount of energy dissipated in the system due to the irreversible plastic processes which are occurring in the material. The energy dissipated by the plastic processes drops as the value of this parameter increases. The variable γ_1 (and γ_2) do not apparently have a large effect on the amount of energy which is being dissipated, but does effect the overall rate of dissipation. In fact, the graph for this variable demonstrates that it determines the brittleness of the response of the material.

In Winnicki's work, initial tests were carried out to test the suitability of the constitutive law for capturing the behaviour of concrete [105]. A direct shear test of a masonry structure and a direct tension on a concrete specimen were performed. The direct shear test was performed

as the macroscale where the constitutive law was used in interface elements which were inserted between the masonry bricks. Both of these tests showed that the constitutive law performed well for these cases. However, no analyses were performed when using the law to analyze concrete at the mesoscale using interface elements. Winnicki focused on adapting the constitutive law outlined here to be employed in the continuum setting. In this setting the interface has an assumed finite thickness in order to allow it to describe strain localization in the material. This approach has not been used in the work presented in this thesis as is it more suitable for problems where the heterogeneities are not explicitly resolved into the finite element mesh. In these cases the averaging procedure becomes important to ensure mesh independent result on the structural level [56]. As the interface elements are used in problems where the heterogeneities are resolved explicitly at the mesoscale, the underlying finite element mesh does not play as important a part in the crack path or behaviour and the constitutive law becomes more importance. Therefore, implementing a sophisticated law, such as Winnicki's, allows the author to capture the crack behaviour in an accurate, if slightly phenomenological, way.

4.2.3 Investigation of the Elasto-Plastic Rate Equations

Following the standard plasticity methodology, adopted for interface elements, the rate of the relative plastic displacements (i.e. the crack opening) is expressed by the normality rule [47]:

$$\dot{\mathbf{g}}_{\mathbf{p}} = \dot{\lambda}\mathbf{m} \tag{4.32}$$

where $\dot{\lambda}$ is the plastic multiplier and $\mathbf{m}$ is the normal to the plastic potential Q :

$$\mathbf{m} = \frac{\partial Q}{\partial \mathbf{t}^{loc}} \tag{4.33}$$

Adopting an associated flow rule (i.e. $Q \equiv F$):

$$\mathbf{m} = \frac{\partial F}{\partial \mathbf{t}^{loc}} \tag{4.34}$$

Using (4.32) and the rate form of (4.27), the rate of tractions in the interface element is given by:

$$\dot{\mathbf{t}}^{loc} = \mathbf{D}^{\mathbf{e}}\left(\dot{\mathbf{g}} - \dot{\lambda}\mathbf{m}\right) \tag{4.35}$$

where $\mathbf{D}^{\mathbf{e}}$ is the elastic stiffness of the interface defined in (4.28). If plastic flow occurs, then the consistency condition must hold. The consistency condition is a mathematical expression

that states the traction state must remain on the yield surface at all times, even if the yield surface is evolving due to the evolution of the degradation parameter κ. This condition can be formalised by the Kuhn-Tucker conditions which are expressed by:

$$\dot{\lambda} \geq 0 \qquad F \leq 0 \qquad \dot{\lambda} F = 0 \tag{4.36}$$

From this condition, if $\dot{\lambda} > 0$ and $F = 0$ and plastic flow is occurring, the consistency condition will only be satisfied if $\dot{F} = 0$, which means:

$$\frac{\partial F}{\partial \mathbf{t}^{loc}} \dot{\mathbf{t}}^{loc} + \frac{\partial F}{\partial \kappa} \dot{\kappa} = 0 \tag{4.37}$$

From (4.31), κ can be described by the magnitude of the plastic displacements. As such, $\dot{\kappa}$ can be calculated by taking the magnitude of (4.32) and this can be substituted into (4.37) to give:

$$\frac{\partial F}{\partial \mathbf{t}^{loc}} \dot{\mathbf{t}}^{loc} + \frac{\partial F}{\partial \kappa} \dot{\lambda} \left\| \mathbf{m} \right\| = 0 \tag{4.38}$$

This equation demonstrates that, to satisfy the consistency condition, the evolution of the yield surface is dependent on both the traction state and the plastic multiplier. For numerical implementation, we must alter the equations to deal with discrete increments of variables and not the rate form of the above equation. The discrete form of (4.32) is given by:

$$\Delta \mathbf{g_p} = \Delta \lambda \mathbf{m} \tag{4.39}$$

On the global level, the requirement of the finite element analysis is to solve the system of equations for the generalised stress degrees of freedom, $\mathbf{v}$, and the displacement degrees of freedom, $\mathbf{q}$. This ensures that global equilibrium is achieved at the end of the load step $n+1$. In the process of advancing from load step n to $n+1$, the calculation of the discrete increment of total relative displacement, $\Delta \mathbf{g}$, at every integration point is required. Using this, we are able to calculate the elastically predicted trial tractions, $\mathbf{t^{tr}}$, using:

$$\mathbf{t^{tr}} = \mathbf{D^e} \left(\mathbf{g}^n + \Delta \mathbf{g}^{n+1,i} - \mathbf{g}_\mathbf{p}^n \right) = \mathbf{D^e} \left(\mathbf{g}^{n+1,i} - \mathbf{g}_\mathbf{p}^n \right) \tag{4.40}$$

where i is the current iteration of the load step. The reason that $\mathbf{g}^n$ and $\mathbf{g}_\mathbf{p}^n$ are used in the above equation, and not the versions for iteration i for the step $n+1$, is that the updated values would be taken from a global iteration solution which is not at equilibrium. Therefore, the last known correct solutions for these variables must be used, which is at the end of load step n. Using $\mathbf{t^{tr}}$ in (4.25), if $F < 0$ then the step is elastic and the traction state is admissible. However, if $F > 0$ the traction state is inadmissible and it is necessary to "return" the traction state to the yield surface to ensure that the Kuhn-Tucker yield condition is met and

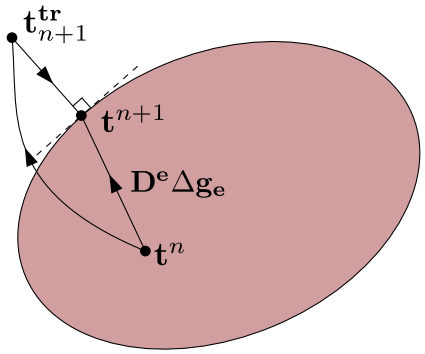

Figure 4.10: Example of Closest Point Projection in traction space

$F = 0$. This return step is known as the plastic corrector. This procedure is highlighted in Figure 4.10. Here, the use of the Closest Point Projection method is demonstrated in traction space where, if an associated flow rule is used and the yield surface is convex, the traction state at $n+1$ represents the minimum distance to the yield surface from the trial traction, $\mathbf{t^{tr}}$ [47]. The plastic corrector step represents the solution to a non-linear problem, whereby the traction state at the end of the iterative procedure results in a decomposition of the relative displacements into their elastic and plastic components. The plastic displacements are computed so that they are representative of the final state at iteration i. The discrete increment of relative displacements, $\Delta\mathbf{g}$, can be decomposed by:

$$\Delta\mathbf{g} = \Delta\mathbf{g_e} + \Delta\mathbf{g_p} \tag{4.41}$$

Substituting in (4.39) and multiplying by the elastic stiffness of the interface gives:

$$\mathbf{D^e}\Delta\mathbf{g} = \mathbf{D^e}\Delta\mathbf{g_e} + \Delta\lambda\mathbf{D^e}\mathbf{m} \tag{4.42}$$

If we consider (4.27), which shows a relationship between the elastic displacements and the tractions, this equation can be written as:

$$\mathbf{D^e}\Delta\mathbf{g} = \mathbf{t}^{n+1} - \mathbf{t^n} + \Delta\lambda\mathbf{D^e}\mathbf{m} \tag{4.43}$$

The first term in this equation assumes that the entire increase in the relative displacement, $\Delta\mathbf{g}$, is elastic and therefore can be considered to be the trial traction, $\mathbf{t^{tr}}$, or the change from $\mathbf{t}^n$ to $\mathbf{t}^{\mathbf{tr}}_{n+1}$ shown in Figure 4.10. Therefore, the above equation can be written as:

$$\mathbf{t}^{\mathbf{tr}}_{n+1} - \mathbf{t}^n = \mathbf{t}^{n+1} - \mathbf{t^n} + \Delta\lambda\mathbf{D^e}\mathbf{m} \tag{4.44}$$

where $\mathbf{t}^{\mathbf{tr}}_{n+1}$ in future is simply written as $\mathbf{t^{tr}}$. For the non-linear solution to be correct, by ensuring the consistency condition and the above equation are satisfied, the following equations

for the residuals can be written as:

$$\mathbf{R_1} = \mathbf{t^{tr}} - \mathbf{t}^{n+1} + \Delta\lambda \mathbf{D^e m} = 0 \tag{4.45}$$

$$R_2 = F^{n+1} = 0 \tag{4.46}$$

To solve these equations a numerical technique is required which is iterative in nature. The two equations are able to be linearised as follows to allow a Newton-Raphson type scheme to be performed:

$$\mathbf{R_1}^{n+1} = \mathbf{R_1}^n + \frac{\partial \mathbf{R_1}}{\partial \mathbf{t}} \delta\mathbf{t} + \frac{\partial \mathbf{R_1}}{\partial \dot{\lambda}} \delta\lambda = 0 \tag{4.47}$$

$$R_2^{n+1} = R_2^n + \frac{\partial F}{\partial \mathbf{t}} \delta\mathbf{t} + \frac{\partial F}{\partial \dot{\lambda}} \delta\lambda = 0 \tag{4.48}$$

where $\delta\lambda$ represents $\delta\Delta\lambda$ for convenience. These two coupled equations give the following system of equations:

$$\begin{bmatrix} \frac{\partial \mathbf{R_1}}{\partial \mathbf{t}} & \frac{\partial \mathbf{R_1}}{\partial \dot{\lambda}} \\ \left(\frac{\partial F}{\partial \mathbf{t}}\right)^{\mathrm{T}} & \frac{\partial F}{\partial \dot{\lambda}} \end{bmatrix} \begin{bmatrix} \delta\mathbf{t} \\ \delta\lambda \end{bmatrix} = \begin{bmatrix} -\mathbf{R_1}^n \\ -R_2^n \end{bmatrix} \tag{4.49}$$

The full derivation for all the terms in this equation, which are applicable to the Winnicki law used here, can be found in Appendix B. This set of equations can be manipulated to find an expression for the iterative change in the plastic multiplier, $\delta\lambda$:

$$\delta\lambda = \frac{R_2^n - \mathbf{m}^{\mathrm{T}} \Xi \mathbf{R_1}^n}{h + \mathbf{m}^{\mathrm{T}} \Xi \mathbf{D^e m}} \tag{4.50}$$

where

$$h = -\frac{\partial F}{\partial \kappa} \|\mathbf{m}\| \quad \& \quad \Xi = \left[\mathbf{I} + \Delta\lambda \mathbf{D^e} \frac{\partial^2 F}{\partial \mathbf{t}^2}\right]^{-1} \tag{4.51}$$

Here, $\mathbf{I}$ is the identity matrix and (4.50) is utilised to find an expression for the change in tractions, $\delta\mathbf{t}$, by using the rearranged form of (4.47) to give:

$$\delta\mathbf{t} = \Xi\left[-\mathbf{R_1} - \delta\lambda \mathbf{D^e m}\right] \tag{4.52}$$

Given $\delta\lambda$ and $\delta\mathbf{t}$, the tractions ($\mathbf{t}$) and plastic multiplier ($\Delta\lambda$) can be updated allowing new residuals to be calculated. If the new residuals are less than specified tolerances then the stress return algorithm is complete, tractions which satisfy the material law for the global iteration have been found and the Kuhn-Tucker yield conditions have been satisfied. To ensure the Closest Point Projection works effectively within the global solution scheme the tolerances used must be carefully chosen. It has been found in the numerical analyses car-

ried out that using tolerances which are at least 3 orders of magnitude smaller than that the tolerances used for the global non-linear solution scheme is sufficient to ensure robustness of both non-linear systems. The procedure for the Closest Point Projection method outlined here can be seen in Algorithm 4.1.

While the Closest Point Projection method has been implemented and explained by several different authors, some particular aspects of its implementation with respect to the Winnicki yield surface must now be highlighted. In (4.51) there is a requirement to calculate $\partial F/\partial \kappa$. This takes the form:

$$\frac{\partial F}{\partial \kappa} = -\frac{2C_0\left(t_{s_1}^2 + t_{s_2}^2\right)B'(\kappa)}{B^3(\kappa)} - C'(\kappa) \tag{4.53}$$

where

$$B'(\kappa) = -\beta\gamma_2\left(B_0 - B_u\right)\exp\left(-\left(\beta\kappa\right)^{\gamma_2}\right)\left(\beta\kappa\right)^{\left(\gamma_2-1\right)} \tag{4.54}$$

$$C'(\kappa) = -\alpha\gamma_1\left(C_0 - C_u\right)\exp\left(-\left(\alpha\kappa\right)^{\gamma_1}\right)\left(\alpha\kappa\right)^{\left(\gamma_1-1\right)} \tag{4.55}$$

To ensure the Closest Point Projection is general and robust, some consideration must be given to the values that are used in light of these previous equations. Since $C'(\kappa)$ and $B'(\kappa)$ contain the terms $\gamma_1 - 1$ and $\gamma_2 - 1$, if no plastic flow has previously taken place in the interface (i.e. $\kappa = 0$) then γ_1 and γ_2 must be greater than or equal to 1.0. If a value less than 1.0 was used, these equations would become ill-posed with no real solution. It must also be noted that, while the equations and procedure outlined in the Closest Point Projection method have used an associated flow rule, Winnicki has demonstrated [105] that the use of non-associated flow rules is also possible.

To test the numerical implementation of the Closest Point Projection algorithm, shown in Algorithm 4.1, three separate numerical tests were carried out. In all cases the Winnicki yield surface was used. However, the evolution of the yield surface could be altered to capture the cases of perfect plasticity, linear hardening and softening purely by changing the equations of $B(\kappa)$ and $C(\kappa)$. For the perfect plasticity and linear hardening cases, the following equations were used:

$$\text{(a) Perfect Plasicity} \begin{cases} C(\kappa) = C_0 & C'(\kappa) = 0 \\ B(\kappa) = B_0 & B'(\kappa) = 0 \end{cases} \tag{4.56}$$

input : $\mathbf{g}$ for Global Iteration i
output: $\mathbf{t_{loc}}$ for Global Iteration i

for *Integration Point in Global Iteration i* **do**
- Find $\mathbf{g}$ at the end of last global load step;
- Find $\mathbf{g_p}$ at end of last global load step;
- Find $\mathbf{g}$ for current global iteration, i;
- Calculate degradation variable $\kappa^{(0)}$;
- Calculate $C(\kappa)$ and $B(\kappa)$;
- Calculate $\mathbf{t^{tr}}$;
- Evalulate F;
- **if** $F <= 0$ **then**
  - Copy $\mathbf{t^{tr}}$ to $\mathbf{t}$;
  - Set $\mathbf{D^e}$ to be elastic modulus;
  - **EXIT ALGORITHM**;
- **else**
  - Set $\Delta\lambda^{(0)} = 0$, $\mathbf{t}^{(0)} = \mathbf{t^{tr}}$, $\mathbf{R}^{(0)} = 0$;
  - *Enter iterative solver to return to yield surface*;
  - **for** *iteration k* **do**
    - Calculate $\delta\lambda^{(k)}$;
    - Calculate $\delta\mathbf{t}^{(k)}$;
    - Update $\Delta\lambda^{(k)}$, $\mathbf{t}^{(k)}$ and $\kappa^{(k)}$;
    - Calculate $\mathbf{R_1^{(k)}}$ and $R_2^{(k)}$;
    - **if** $\|\mathbf{R_1}\| <$ TOL1 & $|R_2| <$ TOL2 **then**
      - **Exit Iterative Solver**;
    - **else**
      - $k = k + 1$;
    - **end**
  - **end**
  - **EXIT ALGORITHM**;
- **end**

end

Algorithm 4.1: Closest Point Projection algorithm

C_0	5MPa	C_u	0MPa
B_0	5MPa	B_u	0MPa
γ_1	2.0	γ_2	2.0
α	2.0	β	2.0
TOL1	$1x10^{-9}$	TOL2	$1x10^{-9}$

Table 4.1: Values for Evaluation of Closest Point Projection

$$\text{(b) Linear Hardening} \begin{cases} C(\kappa) = C_0 + C_0\kappa & C'(\kappa) = C_0 \\ B(\kappa) = B_0 + B_0\kappa & B'(\kappa) = B_0 \end{cases} \tag{4.57}$$

Case (c) is the softening case and it used the equations which were outlined in Section 4.2.2. The test performed determined the number of iterations that were required to return a range of trial traction states to the yield surface. This is visually represented by the contour plots which can be seen in Figure 4.11. These contour plots show the number of iterations required to return to the yield surface from the trial traction state where the iteration number is at the trial traction value. The values used for the terms in the equation and the tolerances employed in the analyses are given in Table 4.1. It must also be noted that in all the tests it was assumed that the value of κ at the start of the analysis was zero. It can be seen in all cases that, if a traction state has no shear component, only one iteration is required. In the transition between pure tension and pure shear, there is a "spike" in the number of iterations required. It is believed that this is due to the influence of the high variation of the tensile regime of the yield surface. As expected, the perfect plasticity case takes the least number of iterations to return to the yield surface. This is because there is no evolution of the yield surface as the iterative procedure progresses. The reason that the linear hardening case takes the highest number of iterations to return to the yield surface is due to the expansion of the yield surface. As the iterative procedure returns to the yield surface, the degradation parameter κ is increasing which causes the yield surface to expand. In effect this means the return procedure and the evolution of the yield surface are moving in opposite directions, so there will be more iterations required to arrive at the correct solution. The same cannot be said for the softening case where the return algorithm and the yield surface evolution are moving in the same direction, thus meaning fewer iterations are required.

4.2.4 Algorithmic Stiffness

When using Closest Point Projection, or any stress return algorithm, some consideration must be given to how the contribution to the global stiffness matrix will be calculated. Once

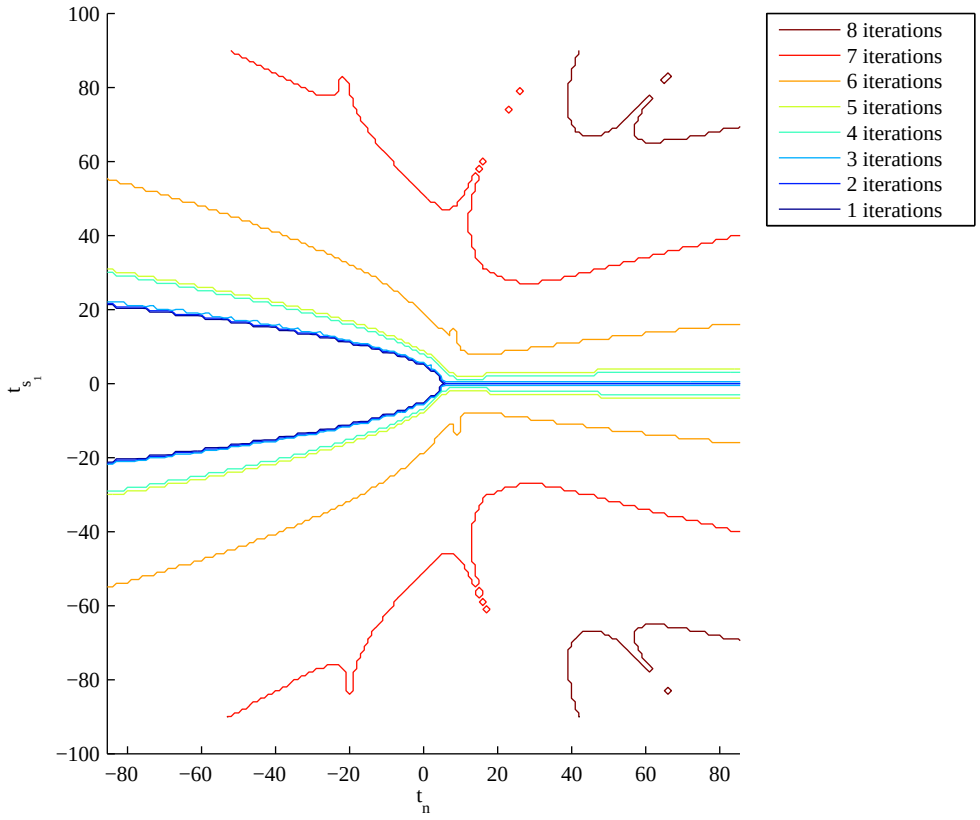

(a) Perfect Plasticity

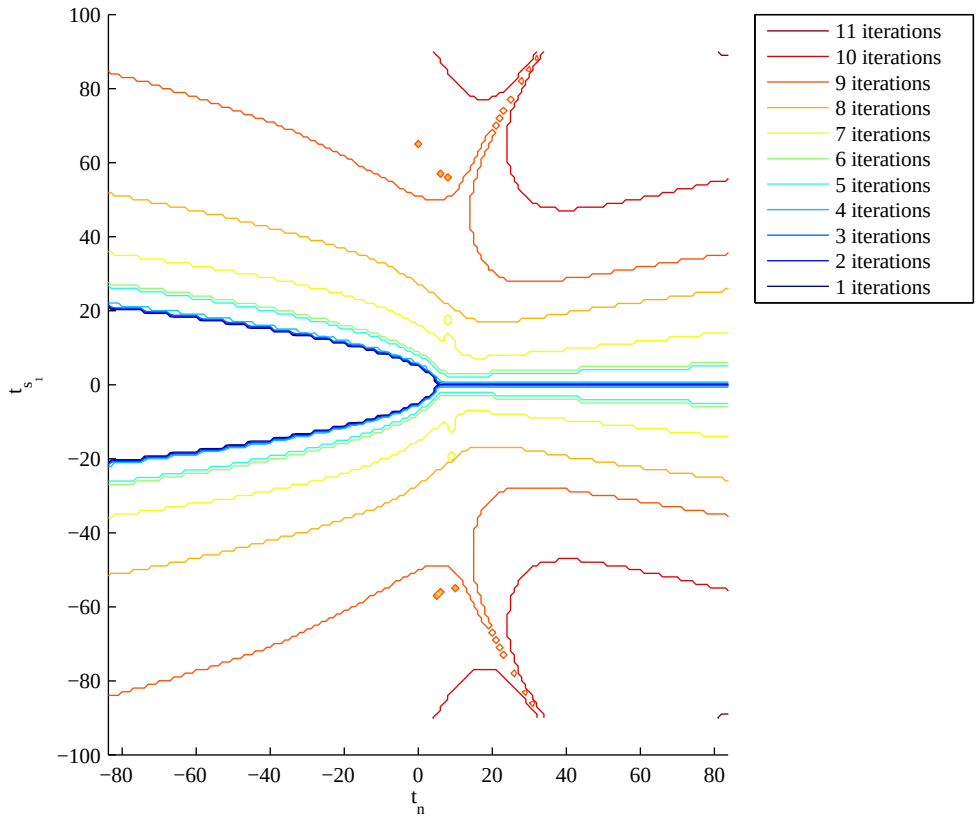

(b) Linear Hardening

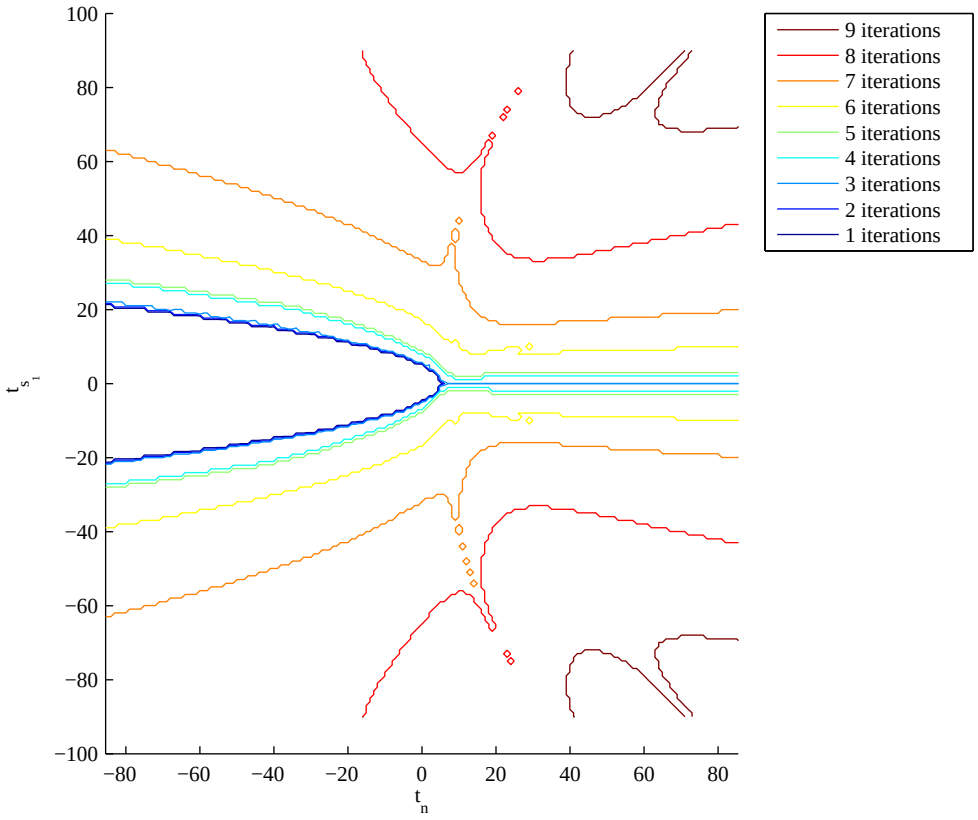

(c) Softening

Figure 4.11: Iso-iteration maps for closest point projection algorithm

the traction state and plastic multiplier for the current iteration, i, in the load step, $n+1$, has been calculated these values can be used to calculate the algorithmic stiffness. If we recall the equation for the interface stiffness matrix, $\mathbf{K_{cr}}$, in (4.17) contains the general term $\mathbf{D}(\mathbf{g})$. This contains the relationship between the tractions and the relative displacements in the interface but for the case outlined here can be considered to be the algorithmic stiffness in the local co-ordinate system related to the constitutive law. If an elastic step is assumed the term $\mathbf{D}(\mathbf{g})$ will simply be the elastic stiffness, $\mathbf{D^e}$, shown in (4.28). However, for the case where plastic flow is occurring this relationship can be defined by the algorithmic stiffness, $\mathbf{D^{ep}}$. The algorithmic stiffness can be defined as being the matrix which is found by the consistent linearisation of the numerical algorithm used for the stress return procedure [47]. It is also known as the consistent stiffness. However, Jirásek has suggested the name consistent stiffness may be slightly misleading as the generic tangent stiffness matrix for materials is also consistently derived [47]. To allow the algorithmic stiffness to be found, some consideration must be given to what is actually trying to be achieved. From the stress return algorithm, we know $\mathbf{t}^{n+1,i}$ but, for the case of the interface element, we are trying to find the relationship which describes the change in tractions, $\delta\mathbf{t}$, due to the change in relative displacements, $\delta\mathbf{g}$,

for the current load step $n+1$. This relationship can be described by:

$$\mathbf{D}^{\mathbf{ep}} \equiv \frac{\delta \mathbf{t}^{n+1}}{\delta \mathbf{g}^{n+1}} \tag{4.58}$$

It must also be noted that the change in plastic multiplier, $\delta\dot{\lambda}$, has to be taken into consideration when formulating the algorithmic stiffness. To accomplish this we must take the basic equation for the evolution of the tractions which can be written as:

$$\delta \mathbf{t}^{n+1} = \mathbf{D}^{\mathbf{e},n+1}\left[\delta \mathbf{g}^{n+1} - \delta \mathbf{g}_{\mathbf{p}}^{n+1}\right] = \mathbf{D}^{\mathbf{e},n+1}\left[\delta \mathbf{g}^{n+1} - \dot{\lambda}^{n+1}\mathbf{m}^{n+1}\right] \tag{4.59}$$

This equation contains the relationship for the change in tractions with respect to changes in relative displacement and contains the plastic multiplier. This equation can then be linearised with respect to both the tractions and the plastic multiplier and with some manipulation an equation for $\mathbf{D}^{\mathbf{ep}}$ can be found:

$$\mathbf{D}^{\mathbf{ep}} = \left.\frac{\delta \mathbf{t}}{\delta \mathbf{g}}\right|_{n+1} = \Xi - \frac{\Xi \mathbf{m}\mathbf{m}^{\mathrm{T}}\Xi}{h + \mathbf{m}^{\mathrm{T}}\Xi\mathbf{m}} \tag{4.60}$$

where

$$h = -\frac{\partial F^{n+1}}{\partial \kappa}\|\mathbf{m}\| \quad \& \quad \Xi = \left[\mathbf{D}^{\mathbf{e}\,-1} + \dot{\lambda}^{n+1}\frac{\partial \mathbf{m}^{n+1}}{\partial \mathbf{t}^{n+1}}\right]^{-1} \tag{4.61}$$

The full derivation of this equation can be seen in Appendix C. The equation presented for the algorithmic stiffness is very similar to the equations found for the Closest Point Projection method and are somewhat independent of the constitutive law used. This means that the implementation into a finite element code can be easily achieved as only terms $\mathbf{m}$,h and $\partial F/\partial \kappa$ will change if a different constitutive law is used. However, further modification would be required in an unassociated flow rule was used.

The major benefit of using the algorithmic stiffness is that it conserves the quadratic rate of convergence of the global Newton-Rhapson iteration scheme. This rate of convergence is lost if a stress return algorithm is implemented without the algorithmic stiffness. The algorithmic stiffness ensures that any problems solved using this scheme are efficient and results will be presented later to show that this convergence rate has been achieved.

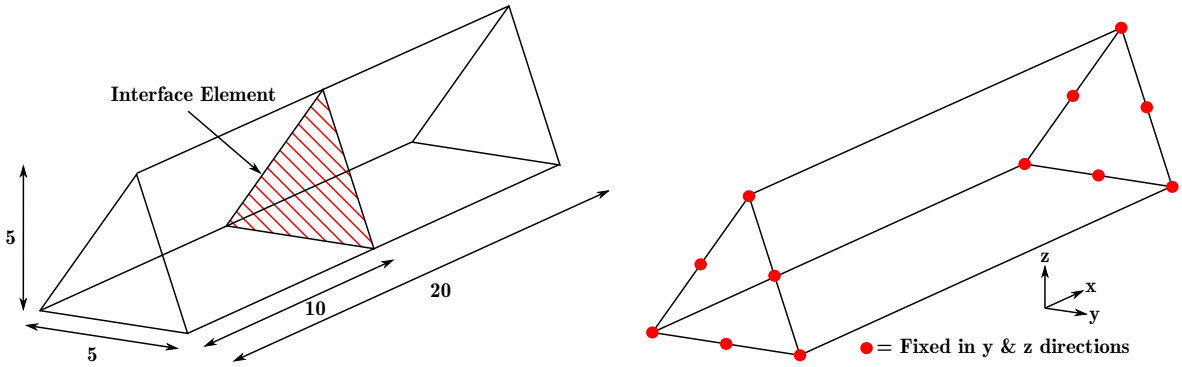

(a) Geometry (in mm) (b) Boundary Conditions

Figure 4.12: Layout of Simple Numerical Test

Material Property	Value
E	20GPa
ν	0.0
C_0 & B_0	5.0N/mm^2
C_u & B_u	0.0N/mm^2
$E_{\text{interface}}$	2000GPa/m

Table 4.2: Values used for numerical test

4.3 Simple Numerical Tests

To test the effectiveness of both the constitutive relationship and numerical technique outlined, a simple numerical test was developed. In this test, and all subsequent numerical tests, 10-noded tetrahedrons are used and as such the interface elements used are 6-noded triangles. To allow a detailed analysis of the interface behaviour to be captured, the mesh was designed so that only one interface was present. The problem is a prismatic bar with a triangular cross section and the interface is placed in the middle, as can be seen in Figure 4.12. The material properties are given in Table 4.2. The elastic (penalty) stiffness of the interface element, $E_{\text{interface}}$, was chosen to ensure numerical stability but was high enough to ensure continuity of displacements in the elastic response range.

To allow the overall softening response to be captured without the need for arc-length control, prescribed displacements were applied horizontally in opposite directions at each end of the specimen leading to a Mode I fracture response. The increment of prescribed displacements for every load step was kept constant to ensure numerical robustness. The numerical test was carried out for different values of α and γ_1 to investigate the effect of changing these parameters. The resulting load-displacement curve can be seen in Figure 4.13. The

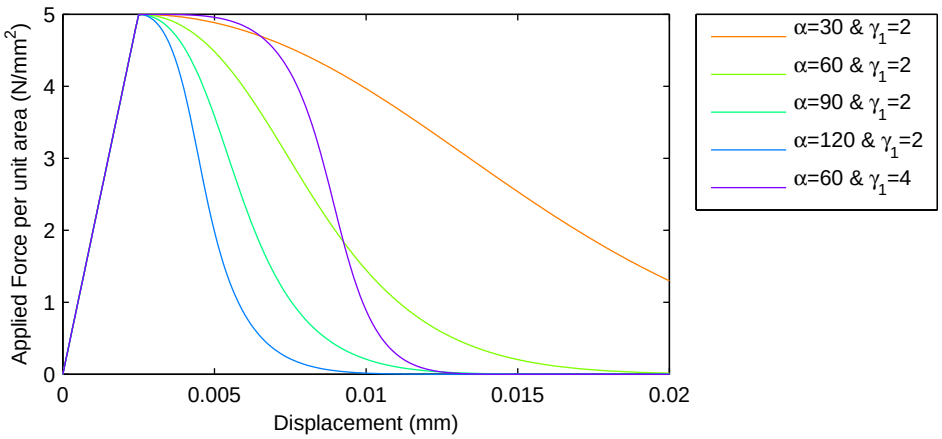

Figure 4.13: Load-displacement curve showing different values of α and γ_1

softening response was initiated at the value of C_0 and higher values of α produced a more pronounced softening branch with less dissipation of energy. Changes in values of γ_1 confirms that this variable controls the brittleness of the response. When a higher value is used the load-displacement graph initially shows very little softening before a much steeper gradient is observed, resulting in a smaller value of displacement at which the material reaches its residual strength.

In the analysis, 200 load steps were carried out with a displacement increment of $1\text{x}10^{-4}$mm. Figure 4.14 shows the results found when $\alpha = 60$ and $\gamma_1 = 2$ for the stress and displacement distributions at load steps 25, 50 and 200. At load step 25, there is no discernible crack and the stress is at its maximum value. Load step 50 shows a well-defined crack in the specimen and a non-zero stress state less than the value of C_0. Finally, load step 200 shows a crack width where almost complete failure is present and there is very little residual strength left in the material. It can be seen that the two separate parts of the prismatic bar are displacing as rigid bodies. These results show a uniform stress state for all load steps and demonstrate that the interface elements and hybrid-Trefftz stress elements are working together as expected and the correct solution is being obtained.

When carrying out this numerical test it was possible to monitor the convergence rate of every load step. Load Step 50 was chosen where the value of prescribed displacement was 0.05mm and the softening law outlined in (4.30) was utilised. The rest of the material parameters were outlined in Table 4.2. For this numerical example, the tolerances used for the Closest Point Projection were set at $1\text{x}10^{-11}$. The convergence of this load step is shown in Figure 4.15.

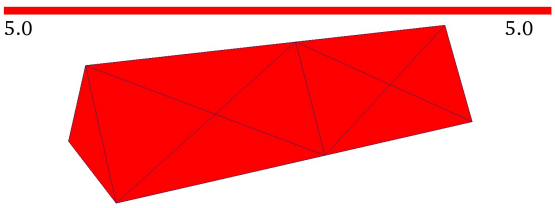

(a) XX stress state at load step 25 (MPa)

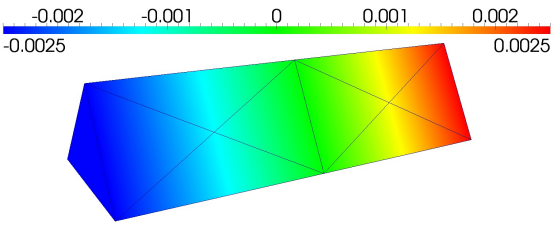

(b) x-displacement state at load step 25 (mm)

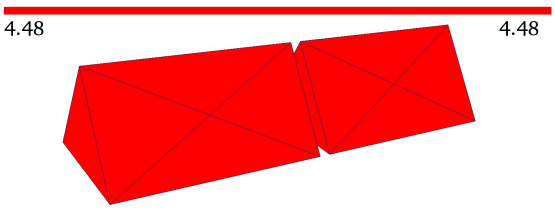

(c) XX stress state at load step 50 (MPa)

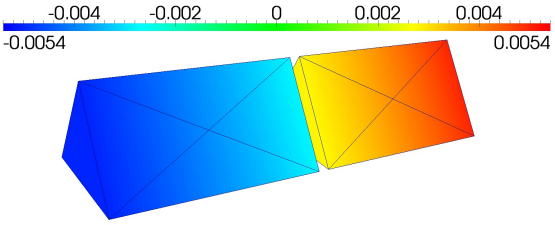

(d) x-displacement state at load step 50 (mm)

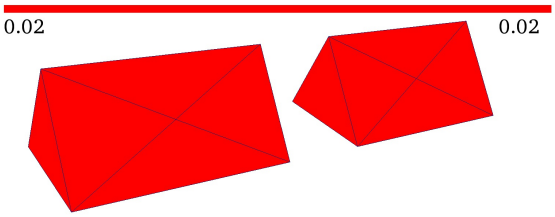

(e) XX stress state at load step 200 (MPa)

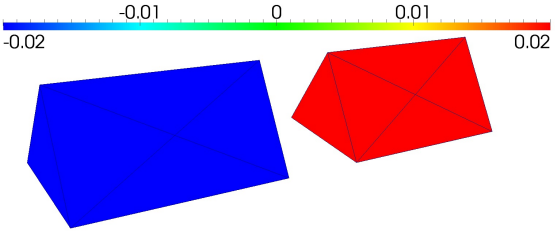

(f) x-displacement x state at load step 200 (mm)

Figure 4.14: Visualisation of numerical test results (displacements magnified x100)

If we have a sequence of numbers, such as the values of the Residual Norm used to plot the graph in Figure 4.15, then an estimation of the convergence rate of this sequence can be found by [4]:

$$\theta \approx \frac{\log\left|\left(x_{n+1}-x_n\right)/\left(x_n-x_{n-1}\right)\right|}{\log\left|\left(x_n-x_{n-1}\right)/\left(x_{n-1}-x_{n-2}\right)\right|} \tag{4.62}$$

where θ is the rate of convergence and x_i signifies the residual norm value of iteration i . If we take the values used for Figure 4.15 and insert them into the above equation, we find $\theta = 2.00$. This signifies that quadratic convergence has been for this load step in the numerical example. The other load steps in this numerical example also exhibited the same rate of convergence.

A second test was devised to investigate the performance of the law in a situation where Mode II fracture dominates. As such the mesh topology of the previous test was modified so that the interface element was inclined to the horizontal at 45° and the loading was applied in the opposite direction (i.e. compressive loading). The material parameters re-

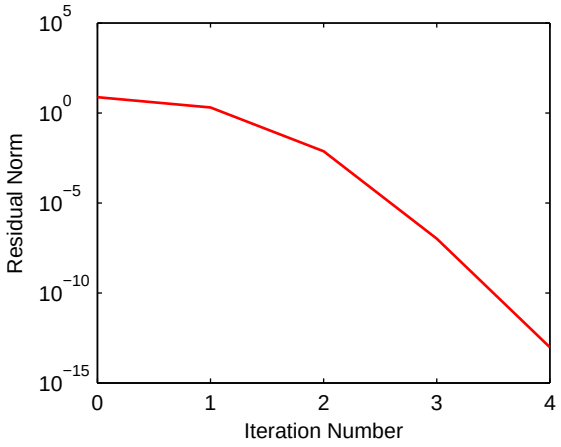

Figure 4.15: Convergence of Load Step 50 with $\alpha = 60$ & $\gamma_1 = 2$

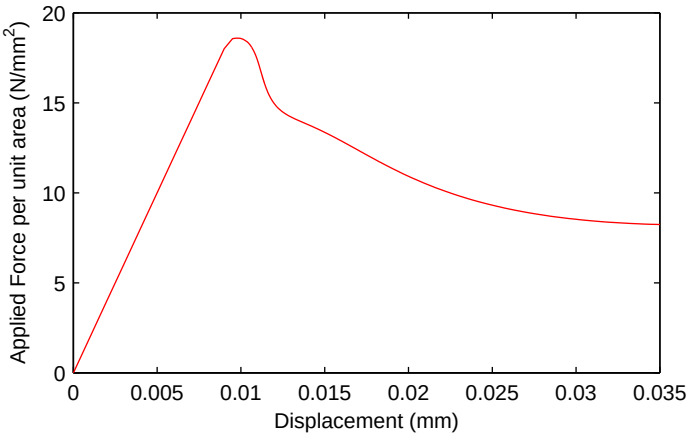

Figure 4.16: Load-displacement curve for compressive loading test

mained unchanged from the previous analysis. The load-displacement curve for the end face of this analysis can be seen in Figure 4.17a. The displaced shape of the model, with the x-displacement field represented, can be seen in Figure 4.17, with the xx stress state at the same displacement value being shown in Figure 4.17b. As can be seen from the load-displacement curve, the non-linear behaviour of the material under compressive loading leading to shear failure has been captured. The displaced shape of the bar shows that Mode II fracture has been captured with no interpenetration of elements in the normal direction to the crack face occurring.

The third test carried out used the same mesh topology as the second test but the load was applied in the tensile direction. This test was devised to investigate the performance of the law in a situation where mixed-mode fracture occurred due to tensile loading. This was the case that was expected to be prevalent in the numerical examples where heterogeneities were

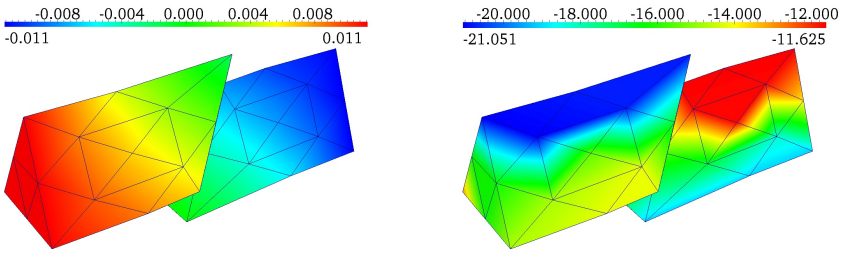

(a) x-displacement state (b) XX stress state

Figure 4.17: Results at end displacement of 0.011mm (displacements magnified x100)

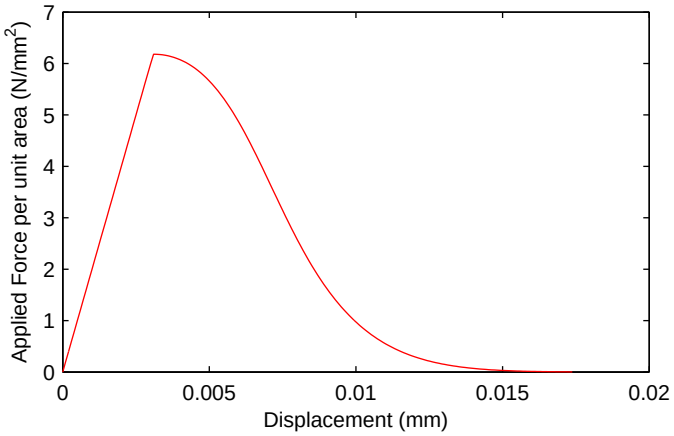

Figure 4.18: Load-displacement curve for tensile loading test with inclined interface element

explicitly resolved by the finite element mesh. To ensure that no bending was induced in the system, the right hand end of the bar was free to move in the vertical direction. This also ensured that the behaviour of the interface alone was captured. The load-displacement curve for the left hand end face in this analysis can be seen in Figure 4.18. The displaced shape of the model, again with the x-displacement field represented, and the stress state can be seen in Figure 4.19. The load-displacement curve for this test shows that the complete capture of degradation of the interface element is achieved in the case of mixed-mode fracture and the stress state results presented show a uniform reduction in the stress in the model is achieved

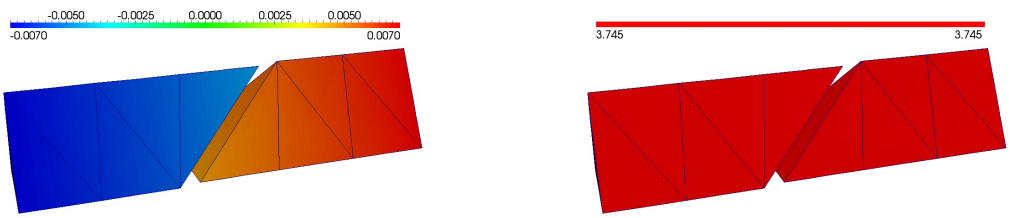

(a) x-displacement state (b) XX stress state

Figure 4.19: Results at end displacement of 0.007mm (displacements magnified x100)

from the peak value where softening initiates.

While carrying out the second test when an interesting aspect of the constitutive law is highlighted. In (4.32), the evolution of plastic displacements is controlled by the plastic multiplier, $\dot{\lambda}$, and $\mathbf{m} = \partial Q / \partial \mathbf{t}$. As an associated flow rule was used, $Q = F$ and $\mathbf{m}$ can be written as:

$$\mathbf{m} = \begin{bmatrix} \frac{\partial F}{\partial t_n} \\ \frac{\partial F}{\partial t_{s_1}} \\ \frac{\partial F}{\partial t_{s_2}} \end{bmatrix} = \begin{bmatrix} 1 \\ \frac{2C_0 t_{s_1}}{B^2(\kappa)} \\ \frac{2C_0 t_{s_2}}{B^2(\kappa)} \end{bmatrix} \tag{4.63}$$

The form of $\mathbf{m}$ means that, for a problem where there is no apparent relative displacement in the normal direction, as was the case in the second test, plastic flow in the normal direction will, nonetheless, occur. At the meso or microscale in concrete, any cracking which occurs is likely to cause dislocations of sections of the material structure. If this occurs when Mode II fracture is taking place, then it is reasonable to assume that the dislocations will cause relative displacements to occur in the normal direction. These relative displacements in the normal direction would be plastic as the surface of the material has been changed by the dislocations and full crack closure in the normal direction would not be possible. The equation shown above ensures that this physical phenomena is captured by the constitutive law outlined in this Chapter.

4.4 Conclusions

The work presented in this Chapter outlined the computational methodology for capturing the non-linear behaviour of concrete in 3D. Initially, the use of interface elements to model the non-linear behaviour was discussed, where tractions across the crack were related to the relative displacements of the crack. The formulation of the stiffness matrix and force vector of the interface element was presented. It was then shown how the interface elements were incorporated into a solution scheme where hybrid-Trefftz stress elements were used. The issue of traction oscillations occurring when interface elements are used with classical finite elements was highlighted and discussed. It was explained that, when hybrid-Trefftz stress elements are used for the bulk elements, the inconsistencies between the stress field in the finite element and the traction field in the interface element are removed to overcome this problem.

The Chapter then moved on to discuss the constitutive law which was applied in the interface element. The Winnicki law was used, which is a plasticity based constitutive model. It was used because it had been developed to be able to capture mixed mode fracture which occurs in concrete, whilst also being computationally robust. One aspect which must be noted about this law, is its phenomenological nature due to the inclusion of variables which were not directly related to any material parameters. It was felt that this could be advantageous, as it gives the user the ability to fine tune the law for particular types of concrete. A stress return algorithm, known as the Closest Point Projection method, was outlined for use with the constitutive law. To ensure a quadratic rate of convergence, an algorithmic stiffness was utilised and results were presented showing that this rate of convergence was achieved for the first numerical test which has been analysed. To ensure computational robustness and to demonstrate the effectiveness of the law for different loading situations, simple numerical tests were also performed on a 3D finite element mesh which included a single interface element. These results showed that non-linear behaviour was adequately captured.

Chapter 5

Crack Insertion Algorithm

The work presented in this Chapter will outline a methodology for inserting interface elements along element boundaries in 3D. This process will be carried out in a dynamic fashion as the analysis progresses, where interface elements are inserted as and when it is deemed necessary to include a cohesive crack, which is different to the conventional approach taken when using interface elements. A full discussion of the method and its computational implementation will be outlined.

When using interface elements in discrete fracture analysis, the convention has been to place them between every element in the mesh or to place them in areas of the mesh where is it predicted cracks will occur. The major disadvantage of this approach is the increase in the number of degrees of freedom (DOFs) in the numerical model. While no detailed analysis has been carried out to compare exact times, Xu and Needleman [107] stated that placing them between every element for a 2D analysis would result in calculation times being at least twice as long if no interface elements were present. This difference in time would clearly be even more extreme for a 3D analysis where the topology is much more complex and the number of interface elements required could increase dramatically. The significant increase in computational time has meant that interface elements were only used in certain locations where cracks were expected to occur to limit the computational cost [63, 77]. However, predicting the crack path *a priori*, both in terms of initiation and propagation, is generally not possible. Also, limiting the areas where interface elements are present may mean that important results are either incorrect or missed entirely. This is particularly true for problems where heterogeneities are explicitly resolved by the finite element mesh. In these cases, it can be assumed that cracks will initially appear around the aggregate particles. However,

once these initial cracks have formed it is very difficult to determine exactly how the crack will propagate and how the initial cracks will join to form a crack on the macro level.

A brief historical overview will be given for how this problem has been tackled in the past, the new methodology will then be presented, the computational aspects of the implementation will be discussed and numerical results showing the cracking algorithm being applied to problems of varying complexity will be presented.

5.1 Historical Review and Problem Discussion

In finite element research, there has been relatively little work carried out to investigate modifying the topology of 3D finite element meshes to allow discrete cracks to be inserted as the analysis progresses. The main sources for work which has investigated this area has been carried out by Pandolfi and Ortiz [69] and later by Pearce *et. al* [70]. The work by Pandolfi and Ortiz gave a detailed outline of how the modification of the mesh would be carried out and therefore formed the basis of the work presented here. The basic idea behind their work, and the new methodology in this report, is that at the end of every load step, the tractions at every integration point on every face are checked to determine if they violate the material law. If it does, then this face is "marked" as a location where a discrete crack must be created. Marking the face is simply a computational term for highlighting the face in the mesh database so that it can be found at a later time. Pandolfi and Ortiz outlined four different positions where a face could be located at in a finite element mesh and demonstrated graphically how the algorithm would work. These locations are shown in Figure 5.1 where newly created nodes are signified by x'. The four different positions are distinguished by how many edges of the face are on the outer surface of the mesh. In the work discussed here, the initial outer surface of the mesh is as expected. However, as cracks are inserted into the mesh, any cracks faces that are created are now also considered as part of the outer surface to allow the procedures to be carried out successfully. The procedure for the four cases outlined in Figure 5.1 can be described as follows:

- Option (a): If no edges of the face are on the outer surface of the mesh, no nodes are split.
- Option (b): If one edge of the face is on the outer surface of the mesh, the mid-side node of this edge is split and a new node is added to the mesh.

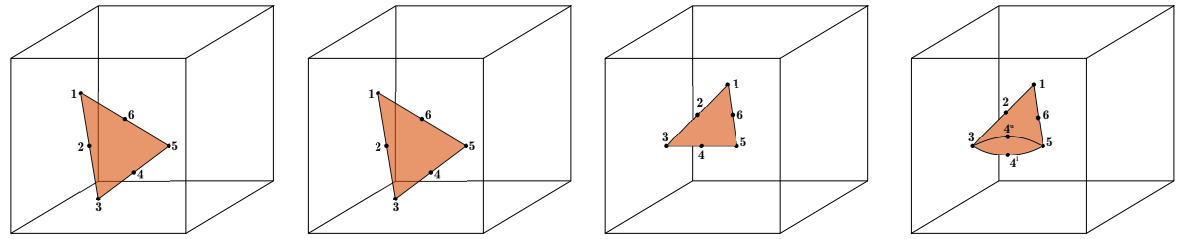

(a) No element edges on surface of mesh

(b) One element edge on surface of mesh

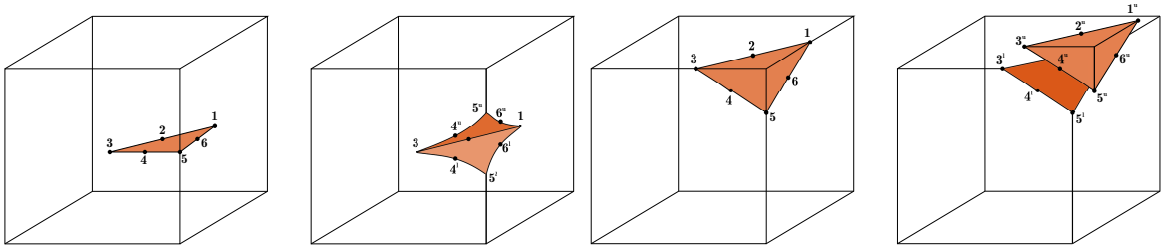

(c) Two element edges on surface of mesh

(d) Three element edges on surface of mesh

Figure 5.1: 4 face locations and subsequent geometry after splitting [69]

- Option (c): If two edges of the face are on the outer surface of the mesh, both mid-side nodes will be split and the corner node that is on both edges will also be split.
- Option (d): If three edges of the face are on the outer surface of the mesh, all 3 mid-side nodes and all 3 corners nodes will be split.

The work presented by Pandolfi and Ortiz [69] has been used in numerous different studies to investigate cohesive fracture but the limitation of Option (a) outlined above was not discussed or highlighted in their seminal paper. In an implicit non-linear finite element analysis, there are two fundamental criteria which must be met. First, the numerical model must be at equilibrium at the end of every load step and, second, the material law must be satisfied at every point in the domain. However, by implementing Option (a), the basic requirement of satisfying the material law is not met. While a new face is created in the data structure and subsequently marked as being on the outer surface of the mesh, which is required for subsequent cracks to be correctly inserted, the connectivity of the mesh does not change and no new nodes are created. Therefore, the solution will be exactly the same as when the analysis was initially run and the material law will still be violated. As this thesis focuses on problems where the heterogeneities are explicitly resolved by the finite element mesh, correcting this issue was vitally important. In these types of problems, it is reasonable to anticipate that the material law would be violated first at the weak interface between the heterogeneities and the surrounding material. As these locations would, in general, not initially be connected to the evolving outer surface of the mesh, Option (a) would be used and no crack would be initiated. This report will now propose a new crack insertion methodology to overcome this

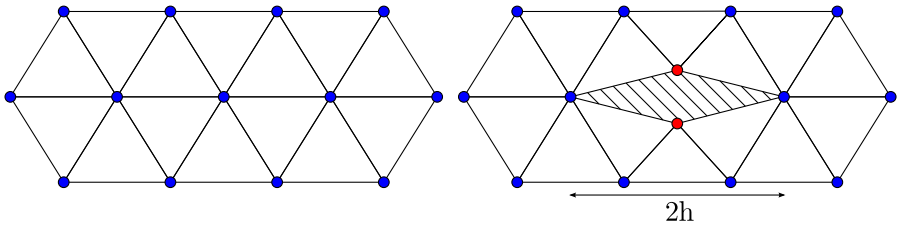

Figure 5.2: Classical finite element before and after node splitting

limitation by taking full advantage of the use of hybrid-Trefftz stress elements used for bulk elements in the analyses.

5.2 New Crack Insertion Methodology

The root of the problem in the Pandolfi and Ortiz method occurred due to the use of the classical finite element and is demonstrated in Figure 5.2, where a 2D problem with linear elements is shown for simplicity. It can be seen that for a single node to be split, a minimum of two adjacent faces to the node must have been marked for splitting to allow this to take place. Therefore, the minimum crack length is $2h$. This is a limitation of using linear classical finite elements in 2D and quadratic classical finite elements in 3D. Therefore, a new methodology has to be developed which can overcome this limitation.

In hybrid-Trefftz stress elements, inter-element compatibility and the kinematic (or displacement) boundary conditions are satisfied in the weak sense, while the traction boundary condition and element equilibrium is enforced in the strong sense *a priori*. However, in displacement based finite (DBF) elements the reverse is the case, i.e. the displacement boundary conditions and inter-element compatibility are enforced in the strong sense *a priori*, while the traction boundary condition and elements equilibrium are enforced in the weak sense. Therefore, for hybrid-Trefftz stress elements, two adjacent faces are able to be treated "independently". This independence is possible because the displacement continuity at the nodes of the element is enforced weakly and the approximation of displacements over the element does not have to strongly satisfy the partition of unity. This is not the case for DBF elements where this partition of unity is enforced *a priori*. This difference means that the minimum crack length can be reduced from $2h$ to h, as is demonstrated in Figure 5.3. Here, the face between Elements 5 and 6, represented by the dashed line, was marked to be split. Taking full advantage of the properties of the hybrid-Trefftz stress element outlined, meant that this

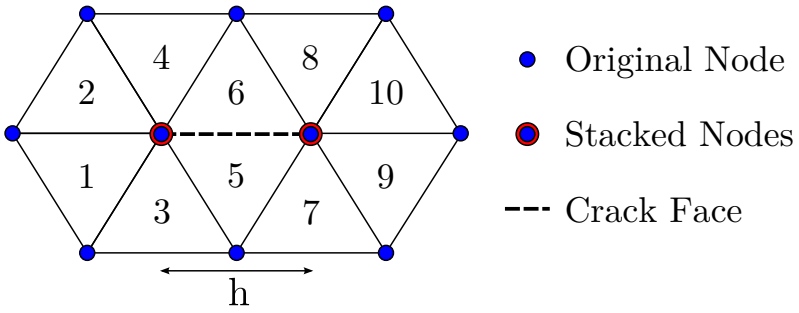

Figure 5.3: Hybrid-Trefftz stress element demonstrating procedure for node splitting

face could be treated separately from the other faces of Elements 5 and 6. As required by interface elements, nodes have to be present on either side of the crack, which would result in the creation of 4 new nodes (2 at each nodal position). Therefore, at the location of the "Stacked Nodes", there would be 3 separate nodes. Two nodes for either side of the interface and the initial node. This initial node would still be a part of all the elements it was originally, as well as the other faces of Element 5 and 6. This arrangement means the two faces which now make up the interface (one face of Element 5 and one of Element 6), are able to move relative to each other, as they are no longer strongly enforcing the partition of unity within the elements. However, a statically admissible solution will still be obtained due to the use of the hybrid-Trefftz stress element *a priori* satisfying equilibrium in the element.

The implementation of the method outlined above needed to be designed to ensure computational efficiency, particularly as 3D problems were being examined. If the method was implemented in 3D (i.e. every node of the marked face was duplicated), the number of nodes in an element with all 4 faces split would increase from 10 to 24. Applying this methodology to a high number of elements in a mesh would then cause the numerical analysis to become inefficient. Therefore, to reduce the number nodes created, the corner nodes are treated in the manner outlined by Pandolfi and Ortiz. By duplicating the mid-side nodes only, relative movement in the interface element would still be captured due to the higher order approximation used for displacement on the face. This is demonstrated in Figure 5.4, where the face is able to move due to the creation of new mid-side nodes, even though the corner nodes have not been modified. The corner nodes are then be split if Option (c) or (d) in Figure 5.1 exists. This alteration reduces the total number of nodes possible for a single element to 16 resulting in improved computational efficiency.

With reference to Figure 5.3, it has been explained that new nodes are created on both sides of

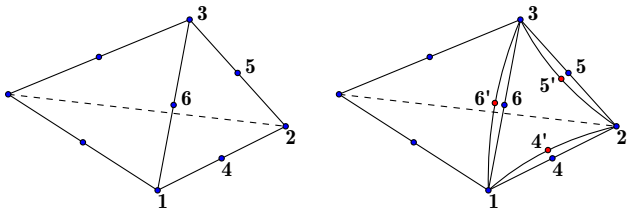

Figure 5.4: Face splitting of interior face showing before and after

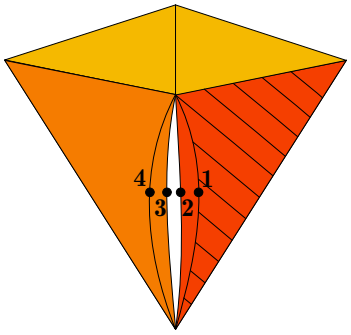

Figure 5.5: Demonstration of mid-side node creation for face splitting

the crack, which allows relative movement between the two independent faces to occur. This movement is controlled by the interface element and is essential to allow the initial stages of cracking to be captured. However, in 3D, the proper implementation of the methodology outlined is much more complex. In these cases, as a crack propagates and faces are split, numerous decisions have to be made to ensure the correct connectivity in the mesh is achieved (i.e. changing element connectivity to ensure elements appear on the correct side of the crack). This problem can become computationally expensive and difficult to implement to ensure a robust solution. However, by using the property of the hybrid-Trefftz stress element outlined above, where the faces can be treated "independently", a simpler approach was implemented. The face marked for splitting contains midside nodes which are members of numerous different faces via its three edges in 3D. Therefore, to aid in the implementation and ensure the method is robust, a new node is created for each face connected via the edges of the face being split. This results in a situation shown in Figure 5.5, where the hatched face is being split. In this Figure, the nodes have been displaced to demonstrate the concept but in reality they will be "stacked" at the same location as before. In this simplified case, where two elements are shown, every face connected to the edge (in this case 4) has a separate node after splitting. As a general rule, for each edge being split $n-1$ new nodes will be created, where n is the number of adjacent faces to this edge. It is recognised that this procedure will increase the number of nodes that are created when a face is split but the procedure performs well and ensures the overall splitting procedure is robust.

As has been shown, the newly proposed method ensures the material law is obeyed at all times but does lead to an increase in computational time due to the addition of new nodes. However, the new method ensures more accurate behaviour is captured if a crack initiates in the interior of the mesh. This is of particular importance in problems where the heterogeneities are resolved by the finite element mesh, as cracks are likely to initiate at the interfacial transition zone and initial crack behaviour may impact on the propagation and evolution of future cracks.

5.3 Computational Methodology of Crack Insertion

This section will now discuss the computational implementation of the method described above. It will show how the crack insertion was carried out in the context of the analysis, how the data structure was handled to allow the cracks to be inserted in a consistent manner and pseudo-code will be presented which outlines the procedure.

When carrying out an implicit non-linear analysis, equilibrium is achieved at the end of a load step. This is done by using an iterative process, such as the Newton-Rhapson scheme. As such, it is prudent to only check for violation of the yield criterion at the end of each load step once equilibrium is achieved. Any face where the traction state across an element boundary violates the yield criterion is "marked" to be "modified". This check is performed at each integration point on the face and the face is marked if the yield criterion is violated at any of these integration points. After the modification procedure, which involves changing the connectivity of the face to insert a discrete crack, has taken place, the load step is then re-analyzed. This procedure is repeated within each load step until the traction state does not violate the yield criterion and equilibrium (convergence) is achieved. This procedure is outlined in Algorithm 5.1.

As can be seen, there is no limitation to the number of faces which can be split in a single load step. Using the approach outlined, some faces which initially violated the yield criterion may not do so in subsequent re-analysis of the load step. Where cracks are introduced but not active, they are not removed, but instead the penalty stiffness is used to ensure continuity of displacements is maintained. It is noted that this approach will increase the computational cost of the analyses that are performed.

```
for General load step, i do
    Solve non-linear system of equations;
    for Every face in mesh do
        for Every integration point on face do
            Evaluate traction state;
            if Material law violated and face not on outer Surface of Mesh then
                Mark face for splitting;
            end
        end
    end
    if Number of faces marked > 0 then
        Split faces;
        Return to start of loop and re-run load step, i;
    else
        Finish load step;
        i = i + 1;
    end
end
```

Algorithm 5.1: Load step outline for crack insertion

5.3.1 Data Structures and Storage

When carrying out crack insertion and geometry modifications to a mesh there is a requirement to ensure the data structures and storage of the mesh is handled in an efficient manner which results in a robust application of the crack insertion algorithm. Pandolfi and Ortiz devoted a large section of their seminal paper on a 3D crack insertion methodology to how this data structure could be created and managed [69]. This allowed very complex crack patterns to be captured in a computationally efficient manner as well as ensuring the code could be applied to any type of problem. However, in the work carried out here all the storage of data about the mesh and changes in the topology were recorded using the Mesh Oriented Database (MOAB) [91]. MOAB has been developed as part of the Interoperable Technologies for Advanced Petascale Simulations (ITAPS) which develops computational packages which can be used together to carry out large scale analyses of problems. ITAPS allows the user to carry out various computational aspects of finite element analyses, such as mesh quality evaluation and improvement, adaptive mesh refinement and partitioning of the mesh to assist with parallel processing. Within the context of the work presented here, MOAB is used to evaluate, store and represent mesh data in an efficient manner both in terms of time

and memory.

MOAB has a built in structure where every object in the finite element mesh has its own unique identifier, known as an EntityHandle. Each type of object (element, face, edge or vertex/node) has an EntityHandle whose form is unique to the type of object. Each single object of that type has an EntityHandle which is unique to all the others. This allows specific types, or even single objects, to be easily identified and grouped together. The major benefit of using MOAB for the crack insertion methodology is its use of the canonical numbering system [90]. In this system the nodes, edges and faces are numbered locally on an element in a certain order. This means that all the procedures developed can be applied to a generic finite element which is numbered in this way.

In addition, MOAB also allows data to be assigned to any Entity and this was utilized in the crack insertion algorithm. This is done using an object called a Tag. These Tags can contain any data the user wants to save and can be assigned to any object with an EntityHandle. Furthermore, MOAB allows elements, faces, edges and nodes to be added to the mesh and allows the connectivity of the elements and faces to be altered as required. MOAB also allows the procedures to be problem independent as it allows the procedures to be based on the topological features of the mesh with no requirement for any geometric information. While an exact implementation of all the MOAB functions used is not given here, any use of these functions will be highlighted so that the use of MOAB is fully outlined.

5.3.2 Detailed Computational Procedure for Crack Insertion

This section will focus on the detailed implementation of the crack insertion methodology for a single crack. This process can be repeated numerous times if several element faces have to be split but to keep the description as simple as possible a single crack in a random location in a body will be dealt with here. As was mentioned, data can be attached to any object in the mesh using MOAB. To allow the outlined methodology to be implemented a change had to be made to how the faces of each tetrahedral element was stored.

In a standard tetrahedron, MOAB can use a built in function to find the four faces of this element, known as its adjacent faces. Usually, the connectivity of the adjacent faces would

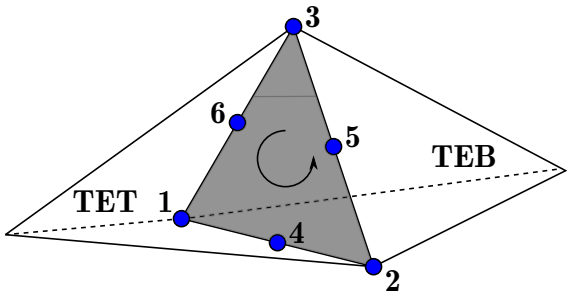

Figure 5.6: Identification of TET and TEB

be dependent on the canonical node numbering of the parent tetrahedron. However, for the proposed crack insertion procedure this will, in general, not be the case after faces have been split. This situation occurs because new mid-side nodes will be created for a face which are not explicitly related to its parent tetrahedron. This means that the MOAB database, and, as such, the built in function, cannot be used to find the adjacent faces. To overcome this issue, at the start of the analysis every tetrahedron had the EntityHandles of its adjacent faces saved in a Tag on the tetrahedron. This means that the adjacent faces can be changed as cracks and new faces are added to the mesh by altering the information in the Tag.

Algorithm 5.2 outlines the basic procedure carried out for each face which has been marked for splitting. A brief guide to some of the aspects of this algorithm will now be given. As the faces which are being split will always have two adjacent tetrahedrons (i.e. the face cannot be on outer surface of the mesh) an early action was to identify the two tetrahedrons adjacent to the face, TET and TEB, which are shown in Figure 5.6. This is done by determining the "sense" of the face with respect to one of the two tetrahedrons adjacent to it, allowing this tetrahedron to be assigned as either TET or TEB. This assignment was vitally important to ensure the correct behaviour of the rest of the algorithm. In the algorithm a new node is created in the data structure as shown in Algorithm 5.3.

This function creates the new node and copies all the relevant data from the old node. As can be seen from Algorithm 5.2 the midside nodes will always be created if a face is marked for splitting, which is in line with the procedure outline in Section 5.2. The procedures for making the decision whether corner nodes are split (Algorithm 5.4) and actually carrying out the splitting (Algorithm 5.5) are in line with those presented by Pandolfi and Ortiz [69]. The procedure for making the decision on whether the corner nodes have to be split is a nested function. It checks if tetrahedrons are connected to the node being decided upon and makes a series of simple logic choices to determine whether the nodes have to be split. If the node

```
for Face marked for splitting, i do
    Find nodal connectivity of face i (MOAB);
    Find two adjacent tets to face i (MOAB);
    Check sense of first Tet w.r.t face i (MOAB);
    if Sense == -1 then
        TET = first Tet;
        TEB = second Tet;
    else
        TEB = first Tet;
        TET = second Tet;
    end
    oldface = Face i;
    Create newface with oldface nodal connectivity (MOAB);
    Add the newface to the Data Structure (MOAB);
    Set oldface and newface as being on edge of mesh (MOAB);
    Set oldface and newface as being opposite faces of Interface Elements
    (MOAB);
    Modify TET adjacencies to replace oldface with newface (MOAB);
    for All Midside Nodes of oldface, j do
        Find all faces in the mesh that contain node j (MOAB);
        Remove oldface from the list of faces;
        for Remaining List of Faces do
            Create New Node - Figure 5.3;
            Change the Connectivity of Face;
        end
    end
    for All Corner Nodes of oldface, k do
        Test whether corner should be split - Figure 5.4;
        if Test == 0 then
            Corner node k not to be split;
            k=k+1;
        else
            Create New Node - Figure 5.3;
            Update Corner Nodes - Figure 5.5;
            k=k+1;
        end
    end
end
```

Algorithm 5.2: Crack insertion algorithm for a face

input : Old Node
output: New Node

for *Old Node* **do**

Get Co-ordinates of Old Node (MOAB);

Create New Node using the Co-ordinates (MOAB);

Add New Node to Data Structure and assign New Node a Global ID (MOAB);

Copy Values of Displacement, Stress State and Boundary Conditions from Old Node to New Node (MOAB);

Mark both Nodes as now being on the Surface of the Mesh (MOAB);

end

Algorithm 5.3: Node creation procedure

has to be split the function will work its way back through the nested procedure and return a final value of 1. This value will then be used in Algorithm 5.2 in another simple logic test.

Looking at the procedure for splitting the corner nodes in Algorithm 5.5 it can be seen that a nested function is once again used to ensure the node splitting is carried out correctly. It can also be seen that the two procedures work in tandem as the value of *counted* is set in Algorithm 5.4 and then is used in Algorithm 5.5 to ensure only tetrahedrons which need to be checked are checked, which saves computational effort. While these procedures have been developed by Pandolfi and Ortiz the use of MOAB made their implementation much more straightforward as a data structure did not need to be created to allow the splitting to take place. The functions themselves are also relatively simple and have been designed in such a way that the splitting is carried out in an efficient and consistent way which only uses the topology of the mesh and takes no account of its geometry.

In this section, the computational implementation of the crack insertion methodology has been outlined using pseudo-code to allow the reader to grasp the concept of how the implementation was achieved. There is an expectation that a thorough knowledge of computational packages such as MOAB would need to be obtained before this methodology could be utilized.

```
input  : TET, TEB, oldnode
output: return value of 0 or 1
Find 4 faces of TET;
Mark TET as having been counted (i.e. counted=1);
for 4 faces of TET, j do
    Find the tetrahedrons adjacent to face j;
    Remove TET from list of adjacent tetrahedrons;
    if Number of Tetrahedrons Left == 0 then
        continue;
    end
    Tetrahedron Left = TET_LEFT
    Find Corner Nodes of TET_LEFT;
    for Corner Node, k do
        if Node k != oldnode then
            continue;
        end
        if TET_LEFT == TEB then
            return 0;
        end
        if counted value of TET_LEFT == 1 then
            continue;
        end
        if This Function Nested with Input TET=TET_LEFT, TEB=TEB and
        oldnode=Node k == 0 then
            return 0;
        end
    end
end
return 1;
```

Algorithm 5.4: Function to test whether corner node to be split

```
input  : TET, oldnode, newnode
output: Updated Topology
Find 4 faces of TET;
Change the connectivity of TET and its 4 faces from oldnode to newnode;
Find tetrahedrons adjacent to 4 faces and remove TET from list;
for Adjacent Tetrahedrons, j do
    Evaluate value of counted for Tetrahedron j;
    if counted == 0 then
        continue;
    end
    Carry out function nested with Input TET=j, oldnode=oldnode and
    newnode=newnode;
end
return;
```

Algorithm 5.5: Function for splitting corner node

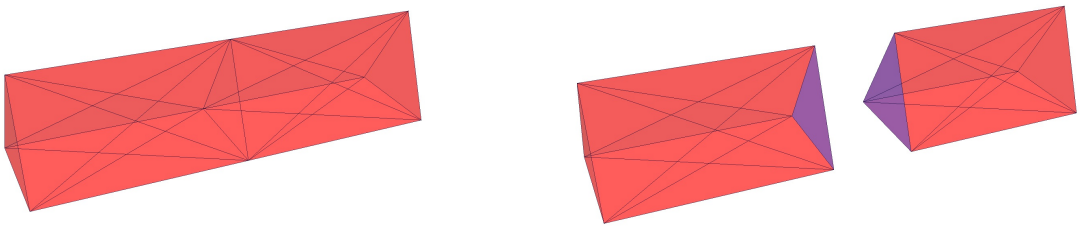

(a) Before Crack (b) After Crack

Figure 5.7: First test of cracking methodology (displacements magnified x100)

5.4 Numerical Examples of Crack Insertion

To demonstrate the use of the crack insertion methodology, several numerical examples have been performed. These numerical tests range in complexity to demonstrate the generality of the algorithm produced. In all of the examples presented, a traction-free (rather than cohesive) crack is inserted if the yield criterion is violated for simplicity. The first numerical test used the same simple 3D mesh that was used to test the interface element constitutive law in Section 4.2. Again a prescribed displacement was applied in increments until the material failed and a face was marked to be split. The results can be seen in Figure 5.7. As can be seen, a single crack was inserted into the mesh which resulted in full separation of the two halves of the model in the correct manner.

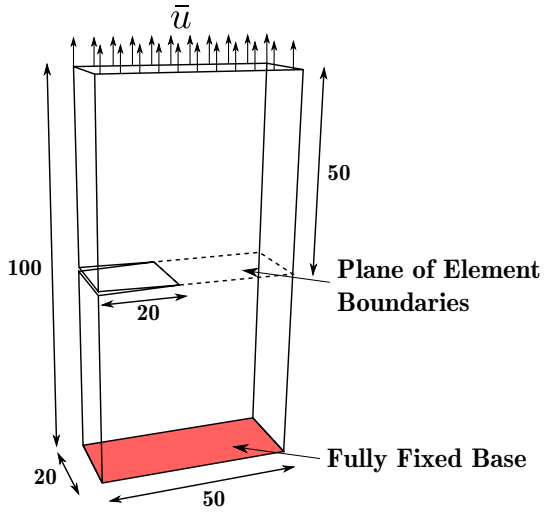

Figure 5.8: Layout of second numerical test with a 0.5mm wide notch showing boundary conditions and position of prescribed displacements in vertical direction only, $\bar{u}_z$ (all dimensions are in mm and lateral displacement on the top face is not restrained)

E	20GPa
ν	0.0
C_0 & B_0	5.0MPa
$\bar{u}_{step}$	0.01mm

Table 5.1: Material parameters used in second numerical test

The second numerical test used a more complex mesh than the first. In this test a notched beam was used so that the crack would initiate from a known position on the surface of the mesh. The mesh was designed to have a plane of element boundaries running from the pre-existing notch perpendicular to the direction the load was applied. This test was done to ensure that the methodology could capture a single crack extending across many elements on a given plane. The layout of the test is shown in Figure 5.8 and the material parameters used for the analysis are given in Table 5.1.

The results can be seen in Figure 5.9. In this test the bottom face of the analysis is fully fixed, while a prescribed displacement, $\bar{u}$, in the vertical direction is applied to the top face. The prescribed displacements were applied in increments, $\bar{u}_{step}$, of 0.01mm to monitor the evolution of the crack. The results presented for this test show that the methodology is working as expected. The crack initiates at the expected location for a notched beam and propagates horizontally in the expected manner until full separation of the two halves of the specimen was achieved.

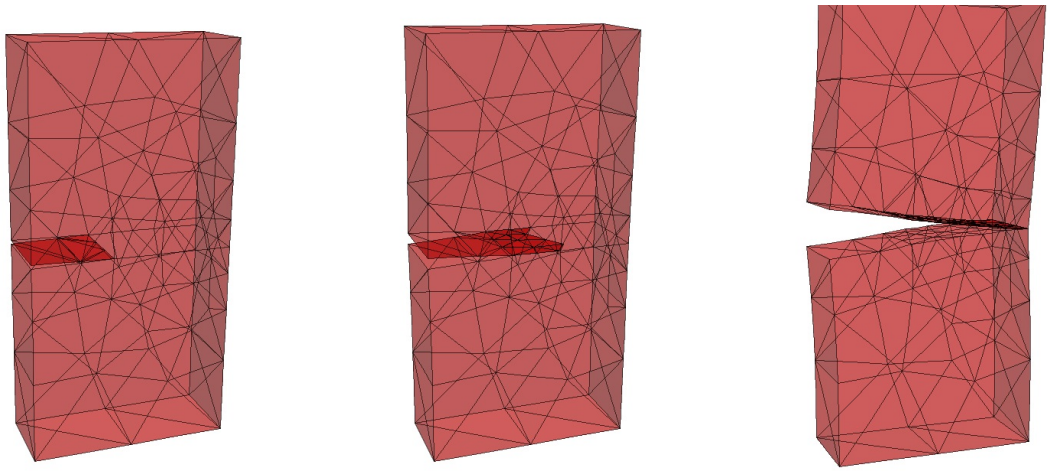

(a) Before crack (b) During crack propagation (c) Full separation of model

Figure 5.9: Second test of cracking methodology

The third numerical test was designed to test the methodology when the crack initiated in the interior of the finite element mesh. In this case a single stiff inclusion (much like aggregate in concrete) was placed in the interior of the volume and the layout of the problem can be seen in Figure 5.10. The material parameters that were used in the analysis can be seen in Table 5.2. It can be seen that the tensile strength, C_0^{ITZ}, and the shear strength, B_0^{ITZ}, of the interface between the stiff sphere and the surrounding material was weaker than between two elements of the same material, C_0^{CEMENT} and B_0^{CEMENT}. This was done to mimic the

E^{CEMENT}	20GPa
$E^{INCLUSION}$	53GPa
ν	0.0
C_0^{ITZ} & B_0^{ITZ}	2.0MPa
C_0^{CEMENT} & B_0^{CEMENT}	5.0MPa
$\bar{u}_{step}$	0.01mm

Table 5.2: Material parameters used in third numerical test

interfacial transition zone of concrete where cracks generally start before propagating out into the cement matrix. As with the previous numerical test the prescribed displacement, $\bar{u}$, was applied in increments of 0.01mm to allow the evolution of the crack to be observed. The results for this analysis can be seen in Figure 5.11. Here, the crack initiates around the sphere as expected (denoted by blue element faces) before eventually propagating to the outer surface of the body.

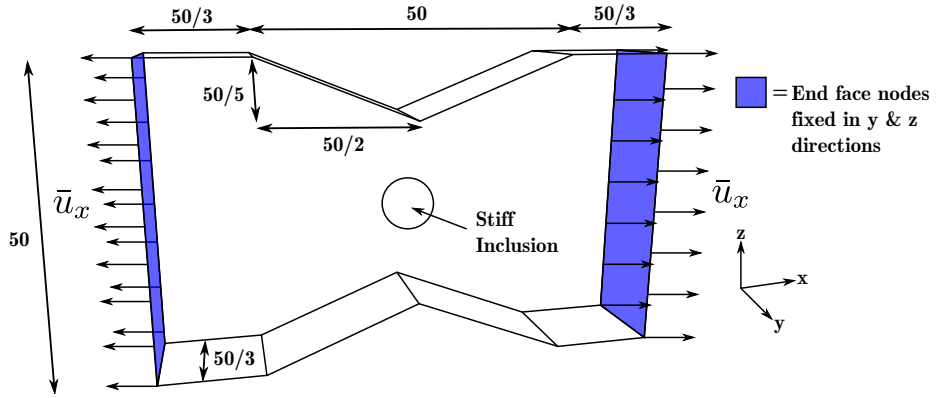

Figure 5.10: Layout of third numerical test showing boundary conditions applied to end faces, the application to the end faces of prescribed displacements, $\bar{u}_x$, in the x-direction only and position of stiff inclusion of radius 4mm at the centroid of the specimen (all dimensions are in mm)

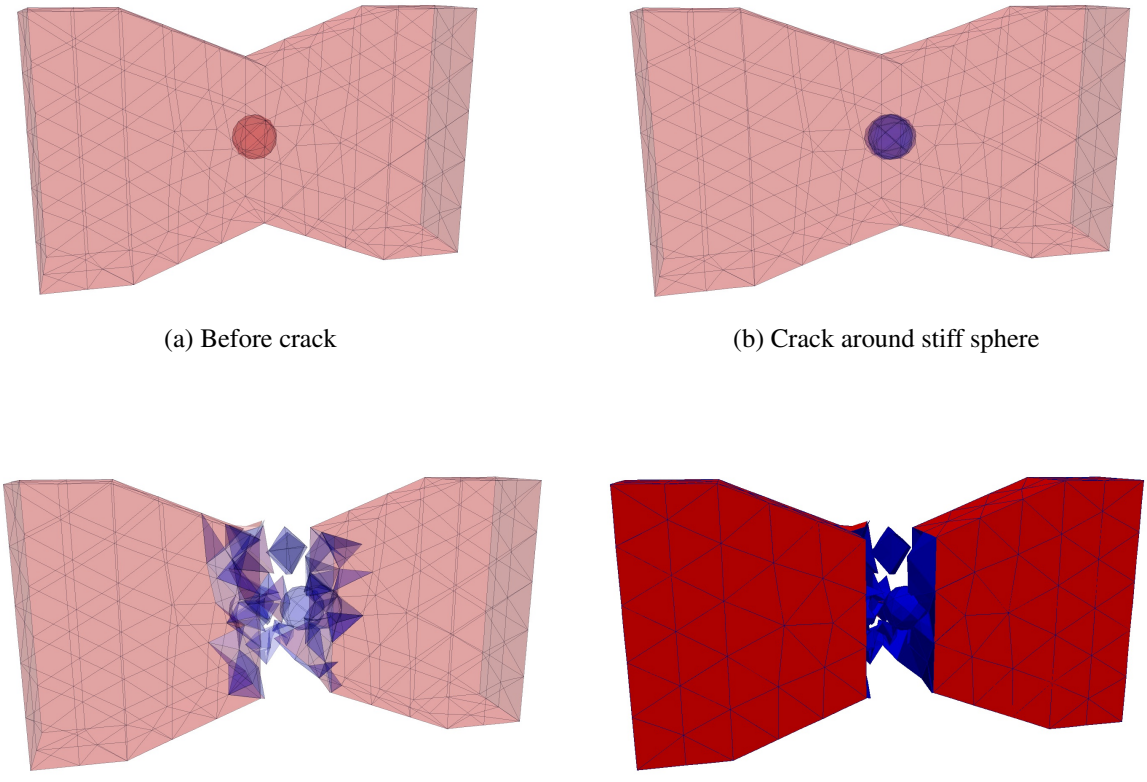

(a) Before crack

(b) Crack around stiff sphere

(c) Full separation showing all cracks

(d) Full separation showing macrocrack

Figure 5.11: Third test of cracking methodology

As has been discussed previously, every time a face is marked for splitting, the first action is to split all of the midside nodes. As hybrid-Trefftz stress elements have been used and the displacement boundary condition is enforced weakly, each face which contains this midside node has a new node created for it. It is acknowledged that this procedure results in a large number of nodes being created when numerous faces are split. For example, in Figure 5.11, the initial mesh contains 1383 nodes which increases to 2433 nodes when the mesh is fully separated by the macrocrack. This increase in nodes obviously increases the computational effort required to solve the problem but it is believed that the improved accuracy of the solution due to the new methodology outweighs any disadvantages.

5.5 Conclusions

This Chapter presented a new methodology to insert discrete cracks along element boundaries in a 3D finite element mesh. The methodology used the work of Pandolfi and Ortiz [69] as its basis but tried to resolve a particular issue with their methodology. As their methodology was created for problems using classical finite elements, at least two adjacent faces had to be split before a discrete crack could be inserted in the interior of a mesh. This presented a large issue in problems where heterogeneities were resolved by the finite element mesh. In these problems, the cracking generally initiates in the interior of the mesh and, using their methodology, would not allow the material law to be obeyed if a single crack face was marked for splitting. In this case, no new nodes are inserted as two connected faces must be marked before a discrete crack can be inserted. This meant that the stress state in the model would not change if one face was marked and the material law would still be violated. However, the new methodology took advantage of using hybrid-Trefftz stress elements to remove this limitation as a single face could now be split independently due to the weak enforcement of continuity within the element domain. A full presentation of this methodology was given, the computational implementation was outlined and details were given on how the storage of mesh data was managed using MOAB. Finally, some numerical tests were presented which showed the new methodology in action for three different problems which ranged in complexity.

Chapter 6

Mesostructure Generation

The focus of the work carried out in this thesis has been to accurately model fracture in heterogeneous materials, such as concrete. As the modelling of this material is taking place on the mesoscale it is important that the heterogeneities are represented in an accurate and precise way to ensure the correct material behaviour is captured [86]. As demonstrated in Figures 6.1 and 6.2, the mesoscale can generally be considered to be at the millimeter scale while the microscale it as the nanometer scale. As the focus of the work presented in this Chapter is at the mesoscale we will focus on the heterogeneities, or aggregate for concrete, which have dimensions of millimeters. At smaller scales than this, concrete contains different physical features such as air voids and cement grains which will be considered to be part of the cement matrix and will not be explicitly modelled. Also, a threshold of 2mm was chosen for the minimum size of the heterogeneity which would be explicitly modelled.

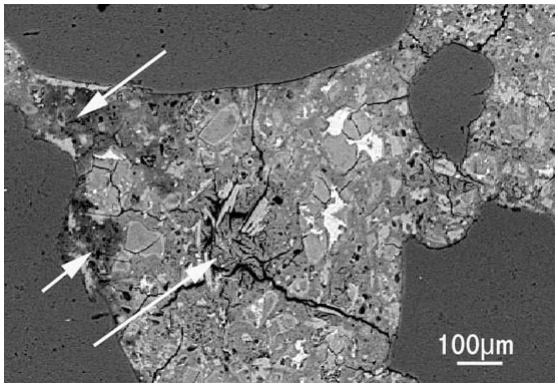

Figure 6.1: Microstructure of concrete[5]

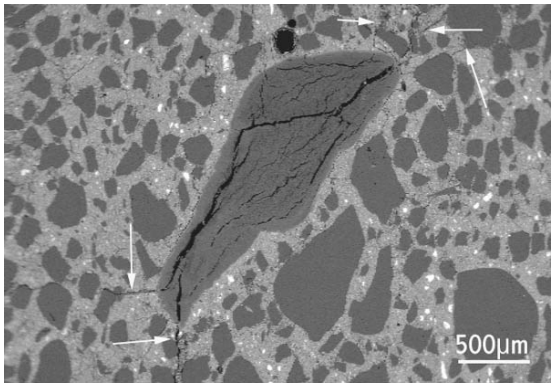

Figure 6.2: Mesostructure of concrete[1]

This chapter will present a methodology to allow fast, efficient and robust production of the mesostructure of a material such as concrete to be obtained. This internal structure can then be used to obtain a good quality finite element mesh to be used in an analysis, where the heterogeneities are explicitly resolved by the mesh. Initially, this Chapter will discuss the historical development of producing geometric representations of heterogeneous structures, sometimes known as particle packing. A historical method, known as Random Sequential Addition, will be presented and its deficiencies will be discussed. Then a newly proposed method called the Maximum Level Set method will be outlined. The benefits of using the Maximum Level Set method will be discussed and finally, results will be presented showing examples of different geometries which have been produced using this method.

Throughout the Chapter, reference will be made to different computational aids, such as CGAL [2] and Cubit [3], which have been used to allow efficient production of both specimen geometries and finite element meshes. CGAL is a Computational Geometry Algorithms Library which can be utilised to perform various algorithmic procedures in a computationally efficient manner. Cubit is a commercial finite element meshing programme which has been utilised to create finite element meshes from the mesostructures that have been created.

6.1 Historical Development

The development of accurate procedures to determine the heterogeneous structure of different materials, such as concrete, is important in many different fields and has been researched in some detail. The method for obtaining these structures is sometimes known as particle packing and can be carried out in various different ways. Experimental work on particle packing has been carried out [42], but is some what limited due to the complexity of setting up appropriate experiments. Therefore, numerical simulations have been developed which can generally be divided into two distinct groups. First, there is a method which uses Random Sequential Addition (RSA) to place the particles in the domain being analyzed. When using RSA, particles are randomly placed within the domain in a sequential manner. Overlap with existing particles, or the boundary of the domain, leads to rejection of that location for the particle. This method has been widely used to generate arbitrary particle arrangements for a domain with some success [26, 85, 89] though there are limitations to this method. The major disadvantage of this method is the extremely high rejection rates, and thus computational time, for problems where high particle packing densities are required. In fact, the

performance of RSA when related to the particle packing density is almost exponential [86]. The performance of RSA can also be severely affected by trying to model particles which are non-spherical in shape and if there is a requirement to keep a certain distance between particles.

Huan [42] has suggested that due to the particles being placed rather than packed RSA results in more evenly distributed particles than in reality and neglects different phenomena such as flocculation, agglomeration and clustering. To overcome these limitations, another method has been developed using the Discrete Element Method (DEM). DEM allows dynamic interactions between particles to be captured by taking into account contact laws, particle velocities and packing characteristics [34]. This method has been applied to concrete in various studies with good results [34, 40, 87] but requires a very substantial computational cost to allow accurate particle packing to be obtained. In fact, in some cases, it was found that the use of DEM to produce an accurate and detailed heterogeneous structure could actually take longer than the finite element analysis itself. Using DEM, there is scope to model the physical phenomena which occur during mixing and pouring of concrete to better capture the particle packing of the material. However, apart from this being computationally expensive [86], it is difficult to accurately capture the physical phenomena which are being observed in reality. Several improvements have been made to attempt to improve the physics behind DEM. These include beginning with a diluted shape which then contracts to bring the particles together in a dynamic manner using Newtonian fluid laws [104] and eliminating the wall effects where particle packing is unrealistically altered due to contact with the external boundary of the volume being modelled [34].

While both the RSA method and DEM have their advantages in particle packing to produce representative mesostructures, both have issues which must be considered. The major issue is the computational time required to carry out the particle packing. This is something which the new methodology presented in Section 6.4 attempts to overcome. Traditionally, RSA and DEM have carried out particle packing using spherical particles and the use of non-spherical particles causes these methods to become even more complex. For DEM, the different behaviour of non-spherical particles can result in a different particle packing arrangement than for spherical inclusions. While for RSA, the numerous overlap checks become even more complex. Another issue when using either of these methods is the possibility that two particles are placed very close to each other in the volume. This can causes serious issues when the domain is subsequently meshed using standard meshing programs. If two particles are

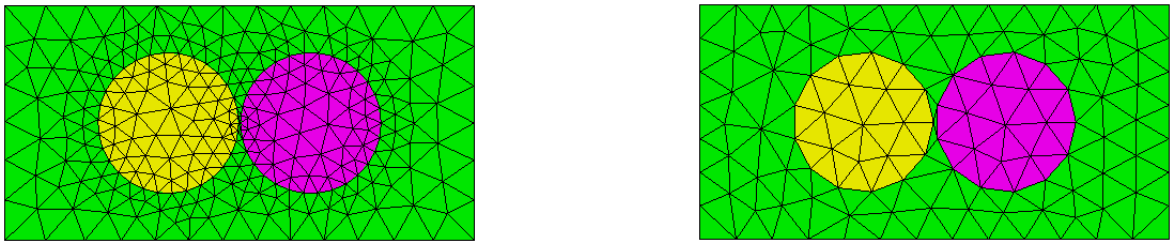

(a) Meshing using adaptive element size

(b) Meshing using constant element size

Figure 6.3: Two example meshes showing problems if particles are close together

very close together and an adaptive element size is used to ensure element quality, then the finite element mesh must be extremely fine to ensure the area between the particles is captured well. This can be seen in Figure 6.3a. However, if a constant element size was used to reduce the number of nodes in the mesh, this could result is poor quality elements being created, as demonstrated in Figure 6.3b, which can adversely affect the subsequent finite element solution.

To overcome the issues outlined, a method was developed which removed some of the computational cost of producing particle packing arrangements. The new method would also ensure particle packing arrangements were created which would result in good quality finite element meshes being created. To do this, the Maximum Level Set Method was used, where particles are placed in accordance with their relative distances to both the boundary of the volume and other particles already placed. This is the approach which will be discussed in detail in this Chapter with a detailed comparison between it and RSA being outlined. This Chapter will also include the physical considerations that must be taken into account for concrete and present some examples of the particle packing achieved using the Maximum Level Set Method.

6.2 Concrete Aggregate

Before discussing the Random Sequential Addition technique and Maximum Level Set Method used, details of how certain variables were obtained for the different methods will be discussed. These variables govern how the mesostructure for concrete is found and were developed from standard methods in the literature. Firstly, when carrying out particle packing, the

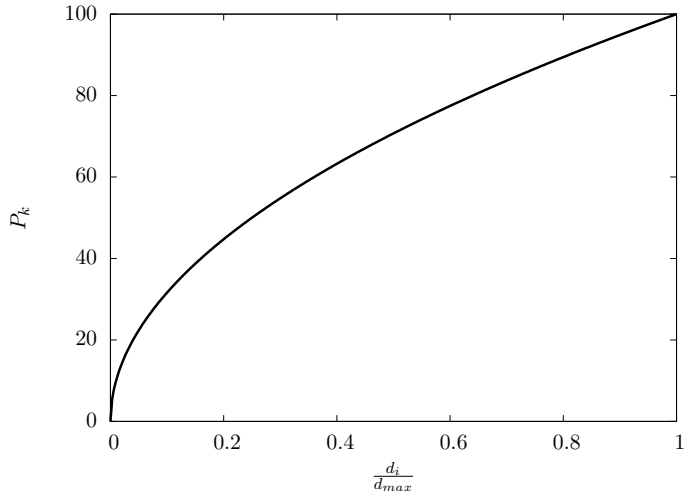

Figure 6.4: Fuller curve for concrete aggregate

requirement is to reach a specific volume fraction, VF. This volume fraction is given by:

$$VF = \frac{V_p}{V_b} \tag{6.1}$$

where V_p is the volume of all the particles placed and V_b is the volume of the entire body. In concrete, the volume fraction can generally range from 0.7 to 0.9, where the variations can be attributed to the aggregate size distribution and particle shapes which are present. The behaviour of concrete is highly dependent on the volume fraction of the specimen being analyzed so it is vitally important that the particle numbers and distributions are calculated accurately. To calculate the number of particles required to achieve the desired volume fraction, standard particle distribution functions are available to govern the number of particles of a given size in the specimen. There are various different particle distribution functions which have been used for concrete which include the Fuller curve, the Bolomey curve, the Graf curve and the Rissel curve. Of these curves the most widely used both in the literature and in practical concrete design is the Fuller curve, which has been implemented in several design codes throughout Europe. The Fuller curve allows the aggregate size distribution to be modified to take account of aggregate shape and workability of the concrete and is particularly suited to determining the particle distributions for concrete which is stiff. The other particle distribution curves mentioned are essentially modified versions of the Fuller curve, for example, it has been found that the Bolomey curve is more suitable for concrete mixes where small quantities of sand are available for the mix. As the Fuller curve is the most widely used particle distribution curve it was chosen for the analyses in this Chapter. The curve is depicted in Figure 6.4 and is given by the equation:

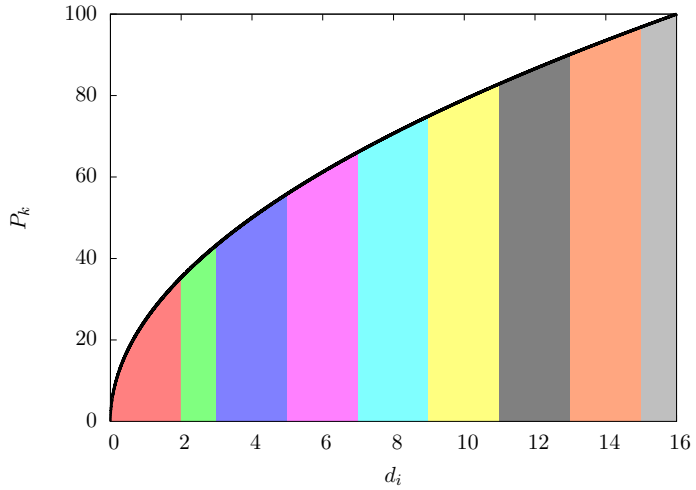

Figure 6.5: Fuller curve showing split for finite number of particle sizes

$$P_i^k = \left[\frac{d_i}{d_{max}}\right]^m \tag{6.2}$$

where P_i^k is the theoretical percentage of the total mass of the particles passing through a standard sieve for particle diameter d_i, d_{max} is the maximum diameter of all particles and m is a parameter which can be used to modify the relationship to suit particular aggregate distributions. In cases where the concrete mix is stiff and has low workability the Fuller curve gives very good results for aggregate size distribution when m is equal to 0.5. In concrete, it is assumed that at a certain value of particle diameter, d_{min}, the particles become an integral part of the matrix material and as such do not need to be explicitly represented in the particle packing algorithm. For the problems that will be modelled in this Chapter it can be assumed that $d_{min} = 2$mm. While in reality, within a given aggregate size range, there are an infinite number of diameters which can be present, a step size d_{int} must be introduced to allow a finite number of particle sizes to be placed. Using a value of $d_{int} = 2$mm, the Fuller curve would be divided as shown in Figure 6.5. Each coloured section of this graph represents a range of probabilities over which a particle in this range can occur. The red section for the particle diameters below 2mm shows that 35.35% of the volume of the total particles in the particle distribution are considered to be part of the matrix and will not be explicitly placed. This has the effect of reducing the overall volume fraction which is achieved and is given by:

$$VF_{eff} = VF\left(1 - \left[\frac{d_{min}}{d_{max}}\right]^m\right) \tag{6.3}$$

where VF_{eff} is the new effective volume fraction. The other sections of Figure 6.5 not below 2mm can be used to calculate the number of particles, N^{ps}, which must be placed for the given size. If we consider the orange section over $d_i = 14$mm, then the volume of

Aggregate Size (mm)	16	14	12	10	8	6	4	2
VF = 0.1	0	0	0	1	3	9	37	189
VF = 0.2	0	1	3	6	13	36	150	758
VF = 0.3	1	4	7	13	29	81	338	1707
VF = 0.4	2	7	12	24	52	144	601	3035
VF = 0.5	3	11	19	37	82	226	940	4742
VF = 0.6	5	16	28	54	118	326	1353	6829
VF = 0.7	7	22	39	74	161	443	1842	9295
VF = 0.8	9	29	51	96	211	579	2406	11323

Table 6.1: Inclusion numbers of volume fractions for 100mm x 100mm x 100mm cube

particles which are assumed to have a diameter of 14mm can be described by the area under this curve. It is assumed that any particle with a diameter in the range of the orange section (in this case 13mm to 15mm) will have a diameter of 14mm. To calculate the number of particles, N^{ps}, which would be required to meet the volume calculated by this curve can be done, for a general case, using the following equations:

$$N_i^{ps} = \frac{\left(P_i^k - P_{-i}^k\right) V_b VF}{V_i} \quad \text{for } d_i = d_{max} \tag{6.4}$$

$$N_i^{ps} = \frac{\left(P_{+i}^k - P_{-i}^k\right) V_b VF}{V_i} \quad \text{for } d_{min} < d_i < d_{max} \tag{6.5}$$

$$N_i^{ps} = \frac{\left(P_{+i}^k - P_i^k\right) V_b VF}{V_i} \quad \text{for } d_i = d_{min} \tag{6.6}$$

where P_{+i}^k and P_{-i}^k are the theoretical percentages of particles passing through a sieve of diameter $d_i + 0.5d_{int}$ and $d_i - 0.5d_{int}$ respectively and V_i is the volume of the single particle under consideration. If it is calculated that, for example, 12.3 particles are to be placed at this particular size increment, then 12 particles will be packed in the subsequent analysis. For a simple cube of 100mm x 100mm x 100mm, the number of inclusions for different volume fractions can be seen in Table 6.1.

6.3 Random Sequential Addition

Random Sequential Addition (RSA) has been the most widely used method for particle packing. This method has always had a high computational cost when a high volume fraction is required. A brief overview of its methodology is presented and the method outlined in this Section closely follows the work presented by Talbot *et. al* [89]. In the RSA method, inclusions are inserted in order of size, with larger particles being inserted first. This ensures that the small particles are not randomly inserted leaving no areas large enough for the bigger particles to fit into the body [42]. The computational procedure for RSA can be seen in Algorithm 6.1 which describes the full run through for each size of particle being placed.

input : $d_{max}, d_{min}, d_{int}, VF, m$
output: Location of All Particles in Body

Find the Number of Particles at Each Size Increment;

for *Particle Size i* **do**

  Randomly create X, Y and Z coordinates of a Point, j;

  Perform Check to see whether Particle is outside the Body;
  if *Partcle outside Body* **then**
    Reject Point and Restart Loop;
  end

  Perform Distance check to boundary of Body;
  if *Partcle too close to Boundary* **then**
    Reject Point and Restart Loop;
  end

  for *Every Particle previously placed* **do**
    Find distance from Point j to Centre of Particle;
  end

  if *Distance between Point j and all Particles* > 0 **then**
    Record Point j as centre of New Particle;
    Add 1 to Total Inclusion Numbers;
  else
    Reject Point and Restart Loop;
  end

  if *Particles Placed = Number needed at current Particle Size* **then**
    Move on to next Particle Size $i+1$
  end

end

Algorithm 6.1: Flow diagram of procedure for RSA method

In the RSA method there are a number of overlap checks which must be carried out before a particle is able to be placed in the body. The first two checks involve checking whether the point is within the boundary of the volume and also if it is far enough away from the

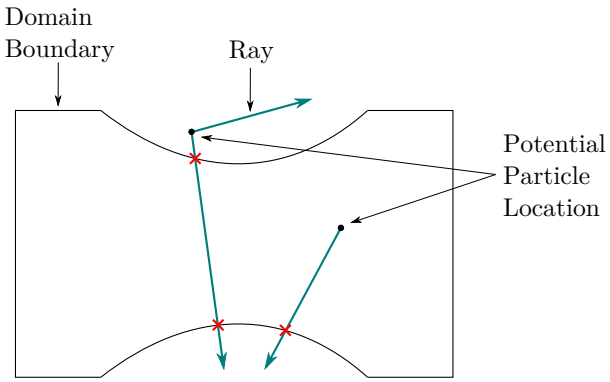

Figure 6.6: Random grid points demonstrating boundary check using rays

boundary for the size of particle being placed. As it was envisioned that this method should be able to be utilized for complex bodies, with no predetermined shape, these calculations could become extremely laborious. Therefore, a library known as CGAL (Computational Geometry Algorithms Library) [2] was utilized to allow any shape of volume to be used. CGAL allows the user to carry out geometric tests and checks on an initial finite element mesh of the surface of the body in both 2D and 3D in a computationally efficient manner. When creating the random particle location, the "ray" function was used to check whether the random location was inside or outside the volume being analyzed. Figure 6.6 demonstrates how a simple logic test was able to be employed to do this. The ray, which is a vector with an infinite length and with a direction chosen at random, would intersect the boundary an odd number of times if the particle location was within the body and an even number, or not at all, if the location was outside the body.

CGAL was further utilized to calculate the distance of the particle location to the surface of the body in an efficient manner by implementing a k-d tree in the calculation. A k-d tree is a useful computational tool, which allows the user to perform complex nearest neighbour checks in an efficient manner by implementing a space-partitioning data structure. When using a k-d tree, the volume being analyzed is essentially split into sub-cells, which are known as leaf cells, to allow searching of the data structure to be more efficient. The first split is carried out at the root node, conventionally splitting the volume using an x-plane first. The selection of the root node is done by choosing the node with the median x-coordinate of all the nodes in the database. If there are an even number of nodes then the root node is chosen as one of the two points closest to the geometric median value. This means the root node has two leaf cells, one which contains all points which have an x-value greater than the root node and the other contains all points with x-values less than the root node. These leaf cells are then further split through their median nodes by a y-plane to produce subsequent

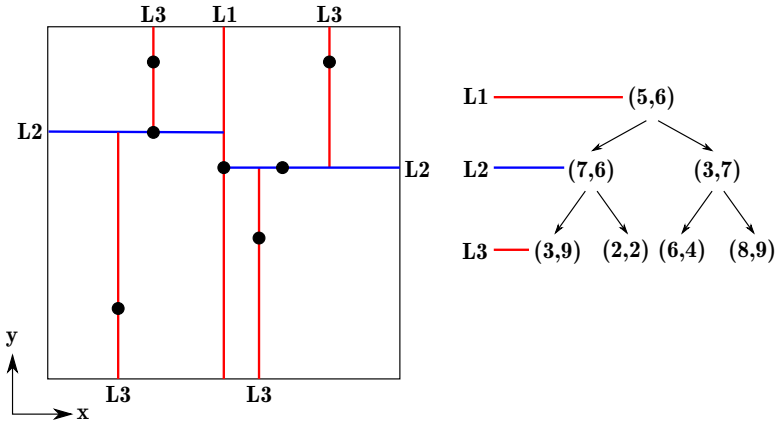

Figure 6.7: Simple k-d tree example showing how the domain was split for Points (2,2), (3,7), (3,9), (5,6), (6,4), (7,6) and (8,9) and the resulting k-d tree

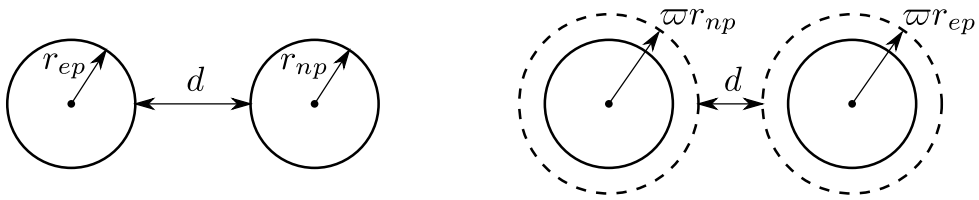

(a) $\varpi = 1.0$ (b) $\varpi > 1.0$

Figure 6.8: Visualisation of value of d

leaf cells. If the problem is 3D then the next split would be carried out using a z-plane, before the x, y and z direction of planes for splitting is repeated until the k-d tree is complete. When the k-d tree is complete, it allows the user to perform a series of computationally cheap logic tests on a given point to travel down the k-d tree to reduce the number of nodes that need to be evaluated to find the nearest neighbour to the point in question found. An example of a 2D k-d tree for 7 points is shown in Figure 6.7.

When a particle was created a final check was then required was to ensure that the newly created particle location does not overlap with any existing particles. This was done using the following equation:

$$d = \left\| \mathbf{x}_{np} - \mathbf{x}_{ep} \right\| - (r_{np} - r_{ep})\varpi \tag{6.7}$$

where $\mathbf{x}_{np}$ and $\mathbf{x}_{ep}$ are the centre coordinates of the new particle and existing particle being examined and r_{np} and r_{ep} are the radii of the particles in question. The constant ϖ was used to control the relative distance between the boundaries of the particles as a proportion of the radius, as demonstrated in Figure 6.8, which shows how d changes as a result of applying a value of ϖ greater than 1. For the simple case of a circular inclusion, this equation was

judged to be the most computationally efficient procedure for finding the distances between two particles. However, if non-circular inclusions were used in the future, CGAL could be used to calculate whether the new particle overlapped with any existing ones. This could be done by using the ray function outlined previously with an odd number of intersections with particles and the outer boundary indicating the particle was not overlapping with anything.

The classical RSA method clearly has limitations in its methodology due to the numerous checks which must be performed before a particle can finally be placed. The distance checks can be considered computationally expensive, even with the use of libraries such as CGAL. It has been found that the overall computational cost does not rise proportionally to the target volume fraction but is a function of the number of rejected particles and as such increases exponentially with an increased target volume fraction [89]. To overcome the inefficient approach of RSA, the Maximum-Level Set method was developed. This will be discussed in the following section.

6.4 Maximum Level Set Method

The Maximum Level Set (M-LS) method was developed to allow faster and more efficient representation of a body containing a random heterogeneous mesostructure with a high particle volume fraction. To overcome the inefficient approach of the RSA method, the M-LS method prevents any rejection by *a priori* selecting points which are both inside the boundary and that do not overlap with any existing particles. However, there are still certain procedures which are carried out in a similar manner to above. First, the particle numbers for each size are once again obtained using the Fuller Curve and, second, the particles are placed in order from largest to smallest.

The basis for the M-LS method is the use of Level Sets to place the particle in a pseudo-random manner. The concept of Level Sets essentially defines a curve (in 2D), or a surface (in 3D), by the iso-contour of a function where $\phi \equiv \mathrm{LS}(\mathbf{x},...) = k$. The level set function $\mathrm{LS}(\mathbf{x},...)$ can be designed to take account of different parameters within the model being investigated and, for the particle packing scenario, may develop based on the mesostructure of the representative volume being investigated. Initially, the representative volume with a domain Ψ can be subdivided into two sub-domains Ψ^+ and Ψ^- by a function ϕ. This allows

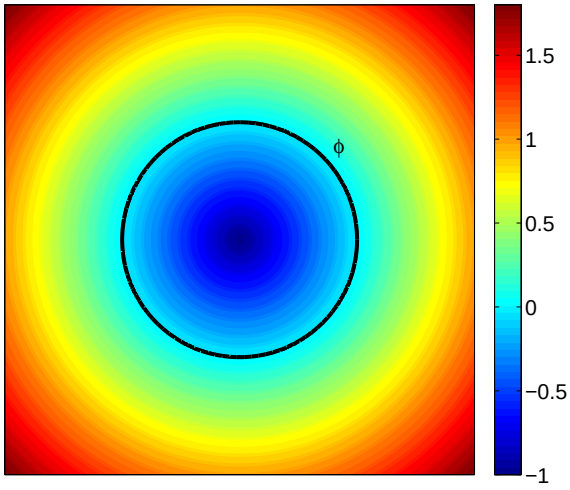

Figure 6.9: Contour plot of level sets for circular particle

a distinction to be made between the two sub-domains, as the Level Set of the function, $\mathrm{LS}_\phi(\mathbf{x})$, will be negative within the domain Ψ^- and positive within the domain Ψ^+ for a point with coordinates $\mathbf{x}$. If the function ϕ is closed, as is the case for the equation of the surface of a particle, then the domain Ψ^- will represent the volume enclosed by the particle itself and, as such, Level Sets can be used to check for overlapping of particles. For spherical particles, which are used here, $\mathrm{LS}_\phi(\mathbf{x})$ depends on both the centre coordinate, $\mathbf{x}_c$, of the particle and its radius, r and takes the form:

$$\mathrm{LS}_\phi(\mathbf{x}) = \|\mathbf{x} - \mathbf{x}_c\| - r \tag{6.8}$$

This equation allows a Level Set value to be found for any point with coordinates $\mathbf{x}$ and results in the contour plot shown in Figure 6.9 for a circular 2D particle with surface ϕ. Similar to Sonon *et. al* [86], a process called "adaptive level set refreshing" is performed where the Level Set for every grid point at time t is updated (i.e. when a particle is added) to reflect the new boundary of the body which includes the existing particles. This is done using the following equation:

$$\mathrm{LS}_\phi(\mathbf{x})^{\mathrm{t}} = \min[\mathrm{LS}_\phi(\mathbf{x})^{\mathrm{t}-1}, \mathrm{LS}_\phi(\mathbf{x})^{\mathrm{t}}] \tag{6.9}$$

The use of Level Sets in the formulation allows minimum distances between particles to be easily implemented but also allows the radius to be scaled by a certain value in a similar procedure to that in (6.7). This is helpful in further ensuring that there is a minimum distance between particles.

The basic procedure for the M-LS method begins by over saturating the body with random grid points, which represent the centre points of the potential spherical particles. Initially, the number of grid points created was assumed to be user defined but this was further developed to be dependant on the Volume Fraction required and the mean size of all the particles to be packed as follows:

$$N_{GP} = OSR\frac{VF}{V_{ave}} \tag{6.10}$$

where OSR is the Over-Saturation Ratio, VF is the required Volume Fraction and V_{ave} is the volume of a particle with the an average radius. The Level Set value for every random grid point is then calculated and the point with the largest value is chosen as the centre of the first particle to be placed. After the first particle is placed, the Level Set value of every remaining grid point is updated, using (6.8), to take account of the new boundary of the body. The next particle is then placed at the point with the largest Level Set value. This process is repeated until the required volume fraction in the body has been achieved. The full procedure for the M-LS method is briefly outlined in Algorithm 6.2.

When using the M-LS method there are two major areas of computational effort involved in the process. The first is the creation of the random grid points for possible particle centres and the other is the placement of particles and the subsequent recalculation of the Level Sets for all the remaining grid points. When creating the random grid points, the major computational effort involves deciding whether the point lies inside or outside of the domain of the boundary. As was demonstrated in Section 6.3, it was possible to use CGAL to ensure this procedure was both robust and efficient. The recalculation of Level Set values for all the remaining grid points was the dominant section of code which influenced overall performance. As such, every time a particle was placed, any grid point with a Level Set less than the radius of the smallest particle was deleted as a location for future particles. This ensured that, as more particles were placed, less calculations were carried out. As the number of random grid points had such a large effect on the performance of the M-LS method, it is important to ensure the value of the Over-Saturation Ratio is not too large. If it is, redundant calculations will have to be performed throughout the entirety of the analysis.

The selection of the OSR must also be carried out carefully to ensure the overall results produced were not adversely affected. As the OSR $\rightarrow \infty$ the grid points would eventually completely cover the volume of the specimen. This would mean that the placement of the particles would no longer be random and would be fully deterministic from the start of the analysis. Clearly, if this was the case the particle packing geometry which would be produced

input : d_{max}, d_{min}, d_{int}, VF, m
output: Location of All Particles in Body

Find the Number of Particles at Each Size Increment;

Find N_{GP} and set location of all in Body;

for *Particle Size i* **do**

  Identify Point with Maximum Level Set;
  Create Particle j of Size i;

  for *Every Grid Point k* **do**

    Find Level Set of Point k w.r.t Particle j;
    if *New Level Set* < *Saved Level Set* **then**
      Update Value in Memory;
    end

    if *Updated Level Set* < $r_{min}.\varpi$ **then**
      Remove Grid Point as Possible Location;
    end

  end

  Add 1 to Total Inclusion Numbers;

  if *Particles Placed* = *Number needed at current Particle Size* **then**
    Move on to next Particle Size $i+1$
  end

end

Algorithm 6.2: Flow diagram of procedure for M-LS method

would not be random. To ensure this issue is minimized and the time of the analysis is kept to a minimum, the OSR must be carefully selected. This is done by ensuring the number of grid points remaining at the end of the analysis is not too high, whilst also ensuring that enough grid points have been placed so that there are enough possible locations for particles.

6.5 Results

6.5.1 Comparison of RSA and M-LS

The aim of this Chapter was to demonstrate that the Maximum Level Set method is more efficient for high volume fractions than the standard Random Sequential Addition method, which has been widely used in the literature. As such this Section will compare the results

Property	Value
m	0.5
d_{max}(mm)	16
d_{min}(mm)	2
d_{int}(mm)	2
OSR	10.0

Table 6.2: Particle properties for comparison of methods

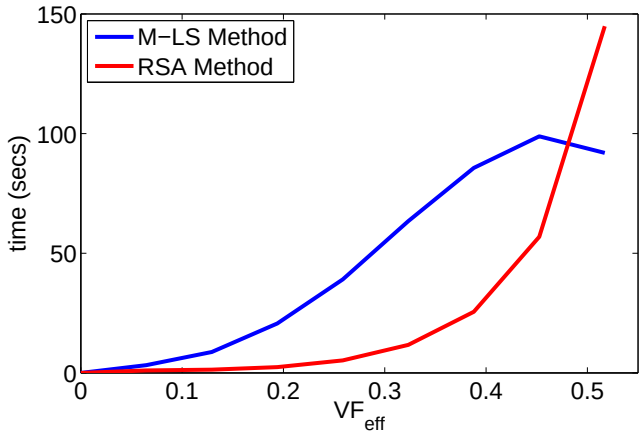

Figure 6.10: Time comparison between M-LS and RSA for different VF

obtained using RSA or M-LS to show whether this was achieved and what effect, if any, the new method had on the resulting particle arrangement. To carry out this comparison a simple 100mm x 100mm x 100mm cube was used with the particle properties shown in Table 6.2. An OSR of 10.0 was chosen to which ensured enough grid points were created to allow all particles were placed, whilst not creating a spurious number of grid points. The comparison of time taken for different volume fractions for both the M-LS method and RSA method can be seen in Figure 6.10. For the graph, the analysis was repeated five times to allow the average times for each volume fraction to be plotted. For both methods, the time taken increases as the volume fraction is increased. For the RSA method the time increases exponentially, while for the M-LS method, the time does not increase in such a dramatic fashion and eventually reduces. The reason for the decrease in time for the highest volume fraction is due to the deletion of grid points as the analysis progresses. From the time comparisons, it is clear that RSA requires much less time when carrying out particle packing for low volume fractions. The obvious reason for this is the low rejection rates when placing the particles and this method should be used in these particular situations.

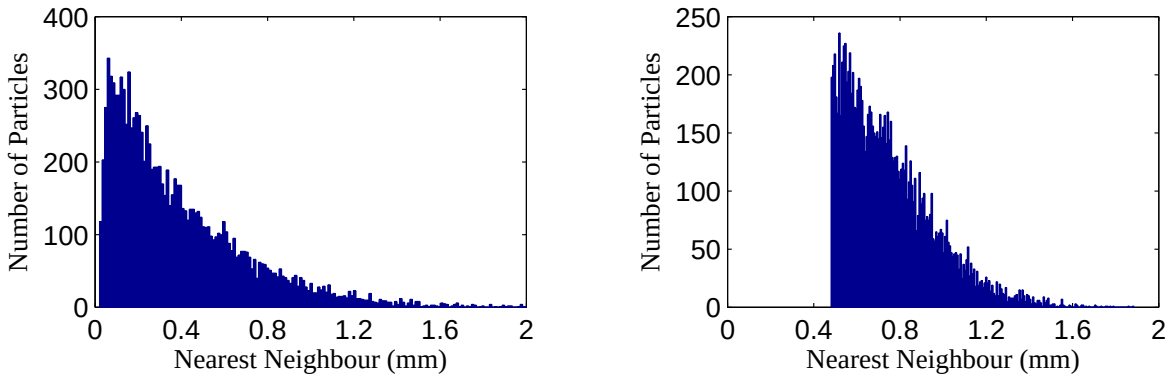

(a) Random Sequential Addition method

(b) Maximum Level Set method

Figure 6.11: Nearest neighbour distances

One of the main differences between the RSA method and M-LS method is the level of inherent randomness within each. In the RSA method the whole procedure is completely random, as the particle position is randomly generated. However, it could be suggested that the M-LS approach should be classified as pseudo-random, as the grid points used in the analysis are randomly generated but the selection of the point at which the particle is placed is not. As such there is a control present in the particle packing which influences the arrangement on the particles. Looking at the different distributions of particles within the 100mm cube for a volume fraction of 0.7, shown in Figure 6.11, it can be seen that the nearest neighbour distance differs quite considerably depending on which method is used. For the M-LS method there is a threshold distance between all particles which is the maximum Level Set value of the grid point where the last particle was placed while for the RSA method there is no minimum distance as the particle placing is random. However, it can been seen that the overall distribution takes a similar shape and the maximum value for the distance between particles is relatively similar. Due to the different distributions found, it can be seen that the M-LS method produces a more regular distribution than the RSA method, since the majority of the particles have a nearest neighbour between 0.5mm and 1.2mm. While this may not be as physically realistic as the RSA method, it is advantageous when creating a finite element mesh. If particles are very close to each other, as can happen in the RSA method, then the finite element mesh produced must either be extremely dense, to capture to very small space between particles, or contain very poor quality finite elements, which could influence the results of the finite element analysis in an adverse manner. Thus a weakness of the particle packing method developed is actually a strength for the purposes of finite element analysis.

Figure 6.12 shows the particle packing carried out using both methods for a 100mm cube

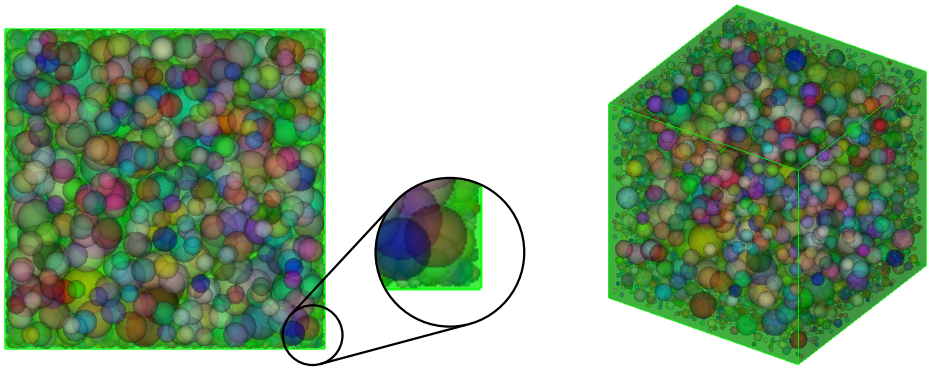

(a) Random Sequential Addition method

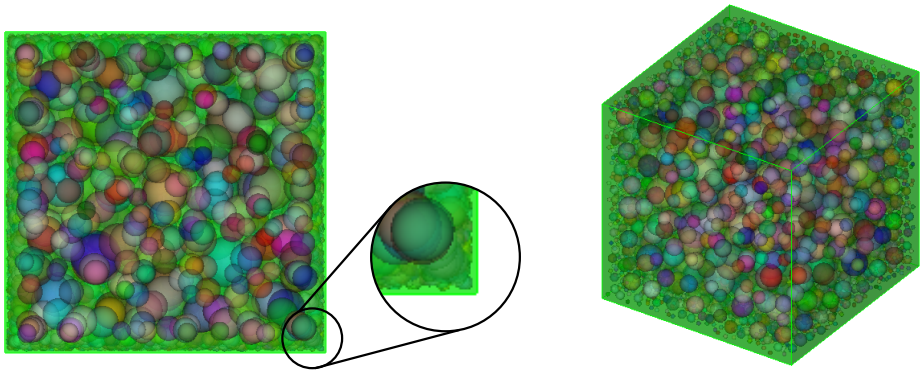

(b) Maximum Level Set method

Figure 6.12: Particle packing of test cube with volume fraction of 0.7 demonstrating the wall effect of the M-LS method

with a volume fraction of 0.7. While both methods produce an extremely dense level of packing some differences can be noted. When viewed from the front, it can be seen that towards the boundary of the cube there is a defined border where larger particles are not placed in the M-LS results compared to the RSA results. This phenomena is similar to the wall effect in concrete where the formwork used in the pouring process causes an uneven distribution of particles close to the border [108]. Since large particles are placed first, they will always be placed further from the outer walls of the body and as such will replicate this wall effect more effectively than would be the case with the RSA method. This effect is able to be observed even more clearly when lower values of volume fractions are used.

6.5.2 Maximum Level Set Method in Action

The previous section has shown that the Maximum Level Set method performed well when compared to the Random Sequential Addition method. However, the objective of this Chap-

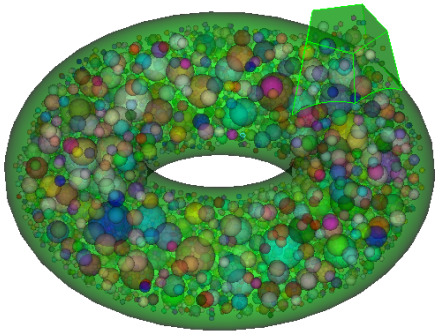

Figure 6.13: Taurus particle packing test

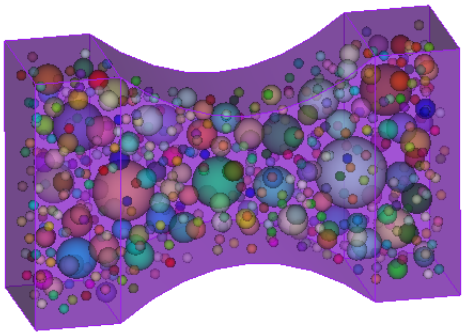

Figure 6.14: Dog bone particle packing test

ter was also to demonstrate a methodology which could be implemented for bodies of any shape and not be limited in scope to simple problems such as the 100mm cube shown in Figure 6.12. As such, Figures 6.13 and 6.14 present two more examples of complex shapes at different scales where particle packing was performed. As can be seen from these example, with the use of CGAL, any shape can be adequately packed using the M-LS method. CGAL is instrumental in allowing the particle packing to be carried out in these examples as it allows different geometric test to be carried out efficiently. In particular, the ability to check whether a point was within the boundary and to calculate the distance of the point to the boundary was vital.

The methodology which has been outlined above has been developed for the purpose of producing a mesostructure which can be used in a finite element analysis. To allow this mesostructure so be used the commercial meshing package Cubit was used to create the finite element mesh from the mesostructure. While performing the M-LS analysis, a script is created which allows Cubit to subsequently be used to create the finite element mesh. Within Cubit there are several different options to produce the mesh allowing the user to use tetrahedrons, cuboids, first order elements and second order elements. Cubit always tries to produce a finite element mesh with as good quality elements as possible to ensure a robust solution is found. The element size can also be specified within the Cubit script and the only limitation on this is that it must be small enough to allow the smallest particle to be resolved sufficiently into the mesh. To demonstrate the effectiveness of using Cubit, a simple analysis was performed. A cube, 10mm x 10mm x 10mm, was created and a M-LS analysis was performed to achieve a volume fraction of 0.8, where $d_{max} = 4$mm, $d_{min} = 1$mm and $d_{int} = 1$mm. The element size used to produce the finite element mesh was kept constant

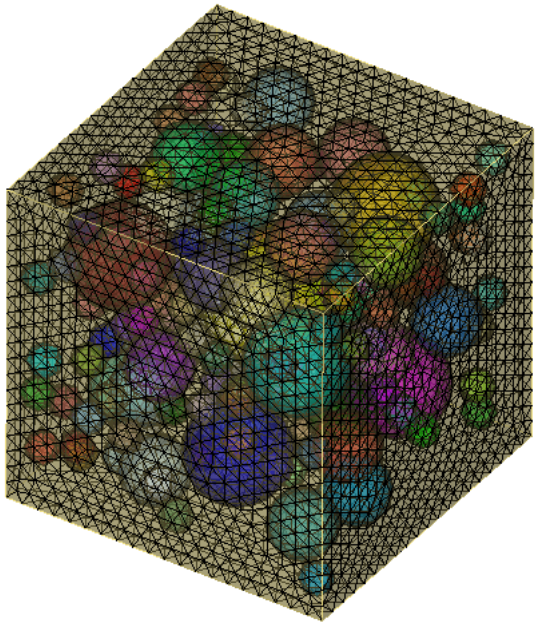

Figure 6.15: Example finite element mesh using Cubit

for the entire body at an element size of 0.5. The mesh which was produced can be seen in Figure (6.15).

6.6 Conclusions and Further Improvements

This Chapter has presented a new method for particle packing of a body using an approach known as the Maximum Level Set method. The standard method of particle packing, Random Sequential Addition, is known to be extremely inefficient when trying to achieve high volume fractions of particle packing due to the random nature of the method. The randomness causes the completion time of the method to vary exponentially with the target volume fraction which is a major obstacle for concrete where the volume fractions required are high (> 0.7). To overcome the inherent inefficiency of RSA, the M-LS method does not randomly select a position for placing particles but places them at pseudo-random locations. The proposed method over-saturates the body with randomly placed grid points and then places the first particle at the grid point with the largest Level Set value. The Level Set value of all the grid points is then updated to take account of the placed particle and the process is repeated until the required volume fraction is achieved. As has been shown, this new method is much more efficient at achieving higher volume fractions and is still relatively competitive with RSA for lower volume fractions. The proposed method also allows a better quality

finite element mesh to be produced because, in general, it will ensure that the proximity of particles to one another is not too small. Finally, the proposed method has also, somewhat serendipitously, reproduced the wall effect present in physical concrete samples.

While the newly proposed method has been demonstrated to perform particle packing in an efficient manner there are several ways in which the methodology could be further improved to make the results more realistic. The first of these would be to include non-spherical inclusions in the analysis. This modification would be of benefit because, although spherical particles are conventionally used when modelling aggregate in concrete, the use of non-spherical aggregate could have a significant effect on the overall fracture behaviour of the specimen [42]. As crack initiation and propagation are stress driven, the use of non-spherical particles would lead to additional stress concentrations. This could be accomplished in a number of ways, such as attempting to initially use Smallest Enclosing Spheres to place the particles originally before creating randomly shape particles which are enclosed by these ghost particles. Another option could be to create several pre-made randomly shaped particles, which could be inserted into the body using the M-LS method [42]. Obviously for this method to work, the Level Set calculations would be much more complex than for spherical particles. Using the k-d tree methodology outlined in this Chapter, along with the ray function in CGAL, would make the implementation of non-circular inclusions somewhat more straightforward than it otherwise may have been. The k-d tree would allow distances between non-circular particles to be calculated more easily and the ray function could be used to check for any cross-over with existing particles. It is felt that this would be an interesting area in which to expand the particle packing methodology developed in this Chapter.

A final variation that could be used in the M-LS method concerns the Level Set function used. In the analyses carried out in this Chapter using the M-LS method, a simple Level Set function was used to define the Level Set value of each randomly created grid point after the placement of every new particle. The grid point with the largest Level Set value was then chosen to be the centre of the next particle. The Level Set function used was linear with respect to r, which is the distance from the element boundary in the normal direction, as seen in Figure 6.16. This function essentially calculated the relative distance between the surface of two different particles being examined which was used to confirm if the particles overlapped. However, if we allow the Level Set function to vary in a non-linear fashion, as shown in Figure 6.17, which eventually tends to a value r_{max}, then this equation could be designed to ensure a more random distribution of particles. This would be done by selecting

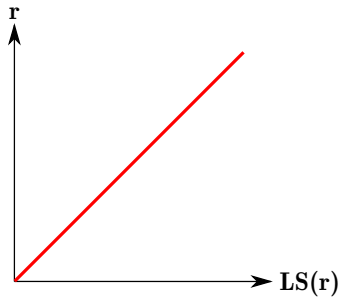

Figure 6.16: Linear variation of LS with respect to r

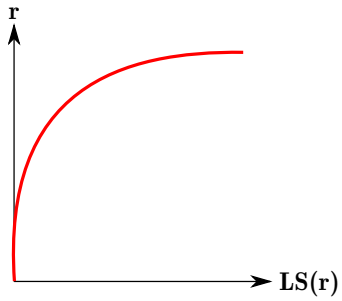

Figure 6.17: Nonlinear variation of LS with respect to r

all the possible particle locations which satisfy the condition, $\mathrm{LS}(r) = r_{max}$, then picking one at random as the location for the next particle. This would result in a more random particle distribution than for the M-LS method. This would be of particular use if extremely high values of the OSR were used, where using the M-LS method may result in overly deterministic particle packing being produced. This method of randomly selecting a particle location based on the Level Set satisfying a particular condition is the approach that was taken by Sonon *et. al* [86] in their work on particle packing.

Chapter 7

Implementation and Analysis of Overall Computational Framework

The goal of the work presented in this thesis has been to create a computational framework to model quasi-brittle fracture in heterogeneous materials, where the heterogeneities are explicitly resolved by the finite element mesh. Initially, this Chapter will focus on the computational implementation of the framework. To do this, the implementation of the non-linear analysis will be discussed and mathematical libraries that have been used, which have been optimised for computational efficiency, will be outlined. Next, the Chapter will focus on how realistic values of material properties were chosen for the constitutive laws, before moving on to numerical examples to demonstrate the performance of the overall framework. Finally, this Chapter will discuss how the framework could be further enhanced.

7.1 Computational Implementation of Overall Framework

This section will outline how the various components of the overall framework are brought together to allow detailed analyses to be performed. The overall aim of the work presented so far was to capture the response of concrete during fracture. When concrete is subjected to tensile loading, its response is highly non-linear, so a solution strategy was developed to capture this. It has been assumed throughout, that the work presented in this thesis is solely investigating material non-linearity in concrete and geometric non-linearity is not considered. In an implicit non-linear analysis, at the end of each load-step the body must be in

equilibrium. This is described mathematically by:

$$\mathbf{f}_{\mathbf{ext}}^{n} - \mathbf{f}_{\mathbf{int}}^{n} = 0 \tag{7.1}$$

where $\mathbf{f}_{\mathbf{ext}}^{n}$ is the vector of externally applied nodal forces at load step n and $\mathbf{f}_{\mathbf{int}}^{n}$ contains the internal nodal forces corresponding to the stresses in the element [9]. To satisfy this equation, an iterative scheme, such as the classical Newton-Rhapson technique, is used. The linearisation of the problem results in a tangent operator, known as the tangent stiffness matrix, $\mathbf{K}$, being determined. The tangent stiffness is used to find the updated value for the displacement degrees of freedom, $\mathbf{q}^{n}$, by using:

$$^{i-1}\mathbf{K}^{n}\delta\mathbf{q} = \mathbf{f}_{\mathbf{ext}}^{n} - ^{i-1}\mathbf{f}_{\mathbf{int}}^{n} \tag{7.2}$$

$$^{i}\mathbf{q}^{n} = ^{i-1}\mathbf{q} + \delta\mathbf{q} \tag{7.3}$$

where the conditions at the start of the load step are:

$$^{(0)}\mathbf{q}^{n} = \mathbf{q}^{n-1} \quad \& \quad ^{(0)}\mathbf{K}^{n} = \mathbf{K}^{n-1} \quad \& \quad ^{(0)}\mathbf{f}_{\mathbf{int}}^{n} = \mathbf{f}_{\mathbf{int}}^{n-1} \tag{7.4}$$

Here, i signifies the iteration number of the load step n and the tangent stiffness matrix is updated at every iteration of the load step. If the tangent stiffness matrix is dealt with in this manner, the convergence rate of the load step to equilibrium will be quadratic.

In the analyses which are performed in this thesis, all non-linear behaviour is restricted to the interface elements. The hybrid-Trefftz stress elements, which make up the bulk material in the mesh, are considered to be linear-elastic and as such the stiffness matrices of these elements will not change as the analysis progresses. If we consider the "stiffness" matrix of the hybrid-Trefftz stress element, $\mathbf{K}^{HTS}$, which is obtained by static condensation of the system of equations in (3.29), this can be written as:

$$\mathbf{K}^{HTS} = \mathbf{A}\mathbf{F}^{-1}\mathbf{A}^{\mathrm{T}} \tag{7.5}$$

while the stiffness matrix of the interface element, $\mathbf{K}^{INT}$, which was previously defined in (4.17), can be written as:

$$\mathbf{K}^{INT} = \int_{\Gamma_{\mathrm{cr}}} \mathbf{U}_{\Gamma}^{\mathrm{T}}\mathbf{R}^{\mathrm{T}}\mathbf{D}(\mathbf{g})\mathbf{R}\mathbf{U}_{\Gamma}\,\mathrm{d}\Gamma \tag{7.6}$$

For a simple problem, shown in Figure 7.1, which is comprised of two bulk elements which

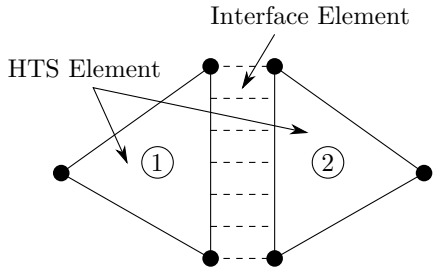

Figure 7.1: Simple visualisation example for hybrid-Trefftz stress element and interface element

are hybrid-Trefftz stress elements (1 and 2) and that are connected by an interface element, the global stiffness matrix would take the form:

$$\begin{bmatrix} \mathbf{K}_1^{HTS} & \mathbf{K}^{INT} \\ \mathbf{K}^{INT} & \mathbf{K}_2^{HTS} \end{bmatrix}$$

It can be seen that the two hybrid-Trefftz stress elements do not share any degrees of freedom and are solely connected through the interface elements. It is also important to note that during the non-linear analysis, $\mathbf{K}_1^{HTS}$ and $\mathbf{K}_2^{HTS}$ do not change and the only change (and thus non-linear behaviour) will occur in $\mathbf{K}^{INT}$. When carrying out the analysis, it is possible to calculate the element matrix $\mathbf{F}^{-1}$ for the hybrid-Trefftz stress element once at the start and save this matrix, rather than carrying out the calculations required each time the stiffness matrix is being constructed. This is possible as the matrix is constructed using terms which correspond to the number of stress degrees of freedom being used and is not altered by any changes in connectivity which can occur due to the crack insertion algorithm. There are contributions to $\mathbf{f_{int}}$ from both the hybrid-Trefftz stress elements and the interface elements which can be given by:

$$\mathbf{f}_{\mathbf{int}}^{HTS} = \mathbf{K}^{HTS}\mathbf{q} \tag{7.7}$$

$$\mathbf{f}_{\mathbf{int}}^{INT} = \int_{\Gamma_{\mathrm{cr}}} \mathbf{U}_{\Gamma}^{\mathrm{T}}\mathbf{R}^{\mathrm{T}}\mathbf{t}^{loc}\,\mathrm{d}\Gamma \tag{7.8}$$

while $\mathbf{f_{ext}}$ contains the externally applied loads. However, the numerical tests performed use prescribed displacements to capture the post-peak softening response of the concrete rather than prescribed force, the benefit of which is demonstrated in Figure 7.2. This ensures that the post-peak response is able to be captured without the the need for any sophisticated arc-

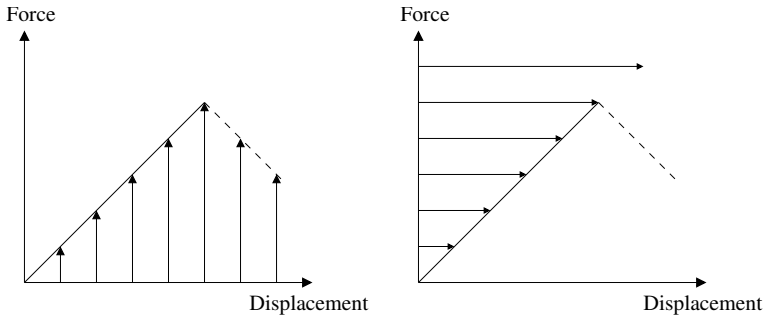

(a) Displacement Control (b) Force Control

Figure 7.2: Comparison of force control and displacement control

length control to be implemented. The implementation of prescribed displacement follows the standard procedure where the node is fixed in the direction of the prescribed displacement and the system of equations is modified to ensure the stiffness matrix remains symmetric. The entire procedure for a single load step, including the dynamic introduction of discrete cohesive cracks, is shown in Algorithm 7.1.

In Algorithm 7.1, building and solving the system of equations in the iterative procedure is the most expensive computational task. Therefore, it is important that this process is carried out in an efficient manner and, here, this was done using the computational package called PETSc [8]. In PETSc, the user creates two procedures to evaluate (7.1) and the stiffness matrix at each iteration, before the package solves the system of equations. The iterative procedure is carried out until the non-linear system of equations converges and a scalar value, given by the norm of the the residual force vector in this case, is less than a user defined tolerance. The norm of the residual force vector is given by:

$$\left\| {}^{i}\mathbf{R}^{n} \right\| = \left\| {}^{i}\mathbf{f}^{n}_{\mathbf{ext}} - {}^{i}\mathbf{f}^{n}_{\mathbf{int}} \right\| \tag{7.9}$$

In the analyses which are presented in this Chapter, the tolerance value was set at $1\text{x}10^{-6}$. PETSc also allows the user to select different methods of matrix factorisation to solve the system of equations in the non-linear solver. In the analyses presented here, LU factorisation is used for this purpose. There are several different options that can be used to increase the computational efficiency of this procedure, such as using different preconditioners, and PETSc allows the user to select different forms of factorisation, such as incomplete LU, to aid with stability and convergence. Cubic line searching has also been utilised within PETSc, which again increases the stability of the numerical solver and its ability to reach a converged state. Another obvious benefit of PETSc, which can be used to dramatically

for *Load Step n* **do**
- Set initial conditions: Iteration Number i=0, ${}^{(0)}\mathbf{q}^n = \mathbf{q}^{n-1}$, ${}^{(0)}\mathbf{K}^n = \mathbf{K}^{n-1}$, ${}^{(0)}\mathbf{f}^n_{\mathbf{int}} = \mathbf{f}^{n-1}_{\mathbf{int}}$;
- Update solution vector with prescribe displacements: ${}^{i}\mathbf{q}^n = {}^{(0)}\mathbf{q}^n + \Delta\mathbf{q}_{pre}$
- **while** ${}^{i}\mathbf{f}^n_{\mathbf{ext}} - {}^{i}\mathbf{f}^n_{\mathbf{int}} >$ *Tolerance* **do**
  - Iteration Number $i = i+1$;
  - **for** *All hybrid-Trefftz stress elements* **do**
    - Calculate element stiffness matrix, $\mathbf{K}^{HTS}$;
  - **end**
  - **for** *All Interface Elements* **do**
    - **for** *Each integration point on face* **do**
      - Carry out Closest Point Projection - **Figure 4.1**;
      - Calculate algorithmic stiffness contribution for Gauss Point;
    - **end**
    - Construct interface stiffness matrix, $\mathbf{K}^{INT}$;
  - **end**
  - Assemble global stiffness matrix for iteration, ${}^{i}\mathbf{K}^n$;
  - Solve system of equations: ${}^{i+1}\mathbf{q}^n = \left[{}^{i}\mathbf{K}^n\right]^{-1}\left[{}^{i}\mathbf{f}^n_{\mathbf{ext}} - {}^{i}\mathbf{f}_{\mathbf{int}}\right]$;
  - Using ${}^{i+1}\mathbf{q}^n$, calculate ${}^{i+1}\mathbf{f}^n_{\mathbf{ext}} - {}^{i+1}\mathbf{f}_{\mathbf{int}}$;
- **end**
- **for** *All faces* **do**
  - Check traction state to see if material law violated;
- **end**
- **if** *Faces marked For splitting >0* **then**
  - Insert discrete cohesive crack into the mesh;
  - Restart load step (i.e. $n = n$);
  - Iteration number i=0, ${}^{(0)}\mathbf{q}^n = \mathbf{q}^{n-1}$, ${}^{(0)}\mathbf{K}^n = \mathbf{K}^{n-1}$, ${}^{(0)}\mathbf{f}^n_{\mathbf{int}} = \mathbf{f}^{n-1}_{\mathbf{int}}$;
- **else**
  - Move onto next loadstep (i.e. $n = n+1$);
- **end**

end

Algorithm 7.1: Entire load step procedure

decrease the computational cost of analyses, is its ability to perform analyses while taking advantage of parallel processing. This feature has not been utilised in the analyses presented, but a discussion on this will be undertaken in Section 7.4.

7.2 Material Parameters

At the mesoscale, concrete can be split into three distinct regions. First, there are the aggregate pieces which are generally made up of crushed rock. Second, there is the softer matrix of cement surrounding these aggregate pieces and third, there is the interfacial transition zone (ITZ) between the cement matrix and aggregate pieces. Separate material properties had to be set for these three distinct regions and those used for the cement and aggregate can be seen in Table 7.1. It has been found that the bonding strength in the ITZ in concrete is weaker than the strength of a cement-cement bond. To reflect this, the yield strength of the bond in the ITZ was set at $2\text{N}/\text{mm}^2$ while the yield strength of the cement bond was $5\text{N}/\text{mm}^2$.

In all the analyses carried out in this Chapter, it was assumed that the normal and shear strengths of the materials were equal and used the relevant values stated above. This was done for simplicity, but these values could easily be different in future tests. As was highlighted in Chapter 4, the Winnicki constitutive law was somewhat phenomenological in nature, as there were variables in the softening laws which were user defined. The equations used in the constitutive law to capture the softening behaviour of the material are repeated here for convenience:

$$C(\kappa) = (C_0 - C_u)\exp\left(-(\alpha\kappa)^{\gamma_1}\right) + C_u \tag{7.10}$$

$$B(\kappa) = (B_0 - B_u)\exp\left(-(\beta\kappa)^{\gamma_2}\right) + B_u \tag{7.11}$$

If we consider the concept of fracture energy, G_f, it can be accurately defined as the energy required to produce a full crack of unit area. This can be related to the load-displacement curve by stating the fracture energy is equal to the area encompassed by this curve [28]. If we consider the equation above, which is used to capture the tensile response of the material, then the equation for the fracture energy can be written as:

$$G_f = \int_0^\infty C(\kappa)\,\partial\kappa = \int_0^\infty (C_0 - C_u)\exp\left(-(\alpha\kappa)^{\gamma_1}\right) + C_u\,\partial\kappa \tag{7.12}$$

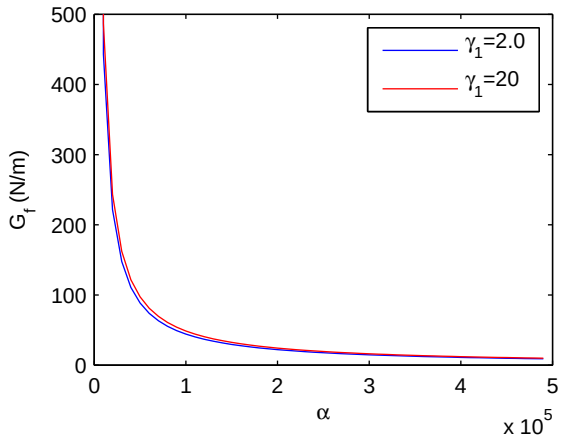

Figure 7.3: Relationship between G_f and α used in softening law

where κ is the degradation parameter and α and γ_1 are the user defined parameters. Due to the inclusion of γ_1, this equation is not able to be integrated exactly. However, if we assume that $C_0 = 5\text{N/mm}^2$ and $C_u = 0\text{N/mm}^2$, then we can numerically integrate this equation to investigate what effect varying α and γ_1 has on the relationship between κ and G_f. A graph showing this can be seen in Figure 7.3. There are two interesting points that can be noted from this graph. First, there is an obvious relationship between the value of G_f and α, which means that α can be chosen to reflect the value of fracture energy for the type of concrete being analysed. Second, the relationship between G_f and α is largely independent of the value of γ_1. In the graph, the change in the relationship from $\gamma_1 = 2$ to $\gamma_1 = 20$ is almost negligible, even though a change of this magnitude has a dramatic effect on the load-displacement response. Therefore, it can be concluded that γ_1 controls the brittleness of the concrete only, with no dramatic effect on the amount of energy being dissipated in the body, while α can be considered a pseudo-material parameter which is related to the fracture energy, G_f. In the analyses carried out in this Chapter, $\alpha = 60,000$ (60) which corresponds to $G_f = 100\text{N/m}$ (0.1N/mm). This value of fracture energy is in the correct range for an average type of concrete, as defined experimentally by Cifuentes *et al.* [24].

7.3 Numerical Examples

In this section, results from numerical test will be shown, where heterogeneities have been explicitly resolved by the finite element mesh. The results presented will show that the framework developed works well, although computational efficiency remains an issue. The geometry of the 3D body used in the subsequent numerical test is shown in Figure 7.4, where

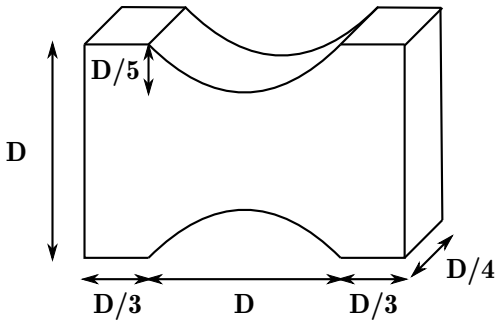

Figure 7.4: Geometry of Dog Bone Specimen

D = 50mm. The computational framework outlined, has been developed to analyse complex problems in 3D with a detailed heterogeneous structures. To analyse problems with thousands of heterogeneities, very fine meshes with a large numbers of elements and degrees of freedom are required. However, due to the computational cost of these types of analyses, the topology of the problem and the mesostructure being analysed was simplified. This allowed problems to be assessed in a realistic time frame. The dog bone specimen used is useful for this purpose, as the stress concentrations will occur in the centre portion of the body (i.e. the curved section). This allows a finer mesh to be used in this area only, thus reducing the computational cost. As the stress is concentrated in this region, the heterogeneities will be explicitly resolved in this area only, as it can be correctly assumed that cracking will initiate, propagate and coalesce here.

In the overall framework, one advantage of using the hybrid-Trefftz stress elements was their ability to approximate stresses extremely accurately. As crack propagation can be considered to be a stress driven problem, for all the numerical tests presented here, the stresses were approximated to the fourth order. The approximation matrices, $\mathbf{S_v}$, containing the Trefftz functions up to this order can be seen in Appendix A. Using an approximation of stresses up to the fourth order also ensured that the number of stress approximation functions was greater than the number of displacement approximation functions, which was a requirement for the hybrid-Trefftz stress element to produce a unique solution. All the analyses also used 10-noded tetrahedrons for the finite elements and 6-noded triangles for the interface elements. As before, isoparametric shape functions were used to approximate the displacements on the element boundaries. Gaussian integration was used for all numerical integration throughout, where a sufficient number of integration points were used to ensure accurate integration was achieved. Finally, an adaptive load step was employed in all analyses to ensure a consistent

$E^{INCLUSION}$	53GPa
E^{CEMENT}	20GPa
$E^{INTERFACE}$	2000GPa/m
ν	0.25
C_0^{ITZ} & B_0^{ITZ}	2.0MPa
C_u^{ITZ} & B_u^{ITZ}	0.0MPa
C_0^{CEMENT} & B_0^{CEMENT}	5.0MPa
C_u^{CEMENT} & B_u^{CEMENT}	0.0MPa
α & β	60.0
γ_1 & γ_2	2.0
Non-linear tolerance	$1x10^{-6}$
CPP tolerance	$1x10^{-9}$
$\bar{u}_{initial}$	0.01mm
its_{req}	15

Table 7.1: Material properties and numerical values used for numerical examples

number of iterations per load step was achieved. This was done using the following equation:

$$\bar{u}_{new} = \bar{u}_{old}\left(\frac{its}{its_{req}}\right) \tag{7.13}$$

where $\bar{u}$ is the value of prescribed displacement for the load step, its is the number of iterations of the previous load step and its_{req} is the user-defined variable for the required number of iterations. In all the analyses carried out $its_{req} = 15$. This ensured that the analysis remained stable and was able to converge, whilst also ensuring the number of load steps required was kept to a minimum. To summarise, the subsequent numerical examples all used the same material properties and values required for the non-linear solver. These values are given in Table 7.1. In this Table, the value of $\bar{u}_{initial}$ was used for the first load step and was the biggest value of prescribed displacement which could be applied in a single load step. The adaptive load stepping was limited to not being able to allow the prescribed displacement to be bigger than this value to ensure numerical stability.

7.3.1 First Numerical Example

The topology of the finite element mesh used in the first numerical test can be seen in Figure 7.5 along with the boundary conditions that were applied to the corner nodes of the end

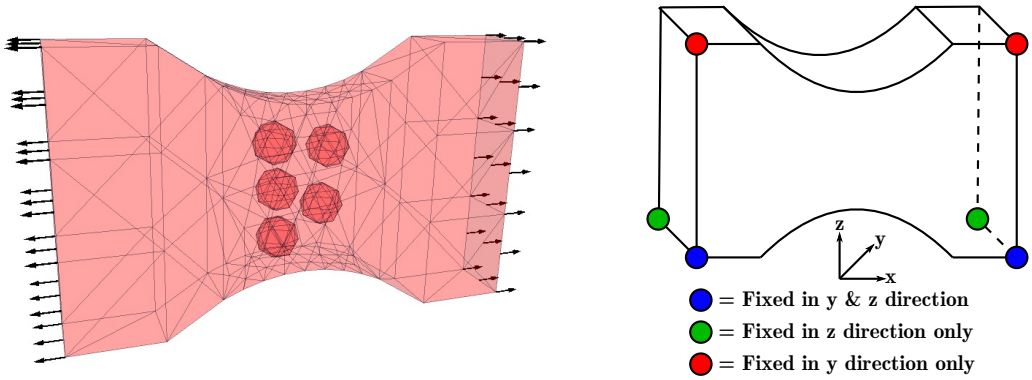

(a) Mesh topology showing heterogeneities (b) Nodal boundary conditions

Figure 7.5: First numerical test setup with prescribed displacement applied in the x-direction only and boundary conditions applied to corner nodes of the mesh highlighted

faces. The Figure demonstrates the simplifications applied to the problem, as a small number of heterogeneities have been resolved by the finite element mesh in the central region. A constant radius of 4mm for the radius of the heterogeneities was used in this test. This ensured that the number of finite elements required in the mesh was kept to a minimum. It was found that, when meshing the central portion of the body, to sufficiently capture the shape of the heterogeneities in Cubit, an element size similar to the radius of the heterogeneities had to be used. This also ensured, for this distribution of heterogeneities, that a good quality finite element mesh was created and the mesh between the heterogeneities was sufficiently fine. Figure 7.5 also demonstrates how the prescribed displacements were applied to the model to enable the tensile response of the concrete specimen to be captured. The initial mesh topology mesh also shows that, outwith the central portion of the specimen, the mesh is much more coarse. This, again, was done to reduce the number of elements to ensure the solution was solved in an acceptable time-frame.

The load-displacement curve for the end face showing the behaviour of the full analysis can be seen in Figure 7.6. As can be seen, the exponential softening of the concrete has been captured and the specimen has been tested to almost complete failure. Figure 7.7 shows the results at Sample Point 1 on the load-displacement graph, where it can be seen that cracks have initiated around the heterogeneities. The graph in Figure 2.1, which shows the theoretical stages of the cracking process in an concrete specimen subject to tensile loading, demonstrates that microcracking in concrete occurs in the early stages of loading, when the overall response of concrete at the macroscale is still considered to be linear-elastic. The results presented at this Sample Point demonstrate that this behaviour is being captured. Microcracks have formed around the inclusions in the specimen but the overall response

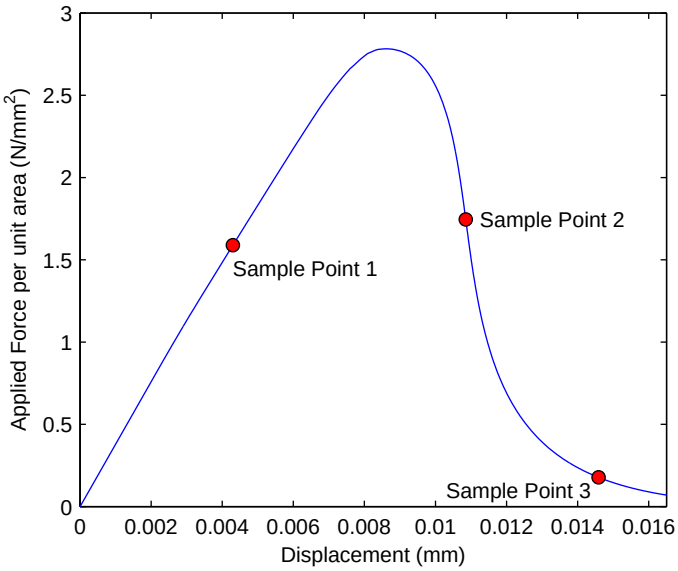

Figure 7.6: Load-displacement curve of end face for first numerical test

of specimen can be considered to be very close to linear elastic, as the non-linear response is not large enough to be seen in the load-displacement graph. From the beginning of the analysis, the presence of heterogeneities led to stress concentrations to occur which are still present after initial cracks appear, as demonstrated in Figure 7.7b. It was found that, as the analysis progresses, the location of these stress concentrations was where the cracks began to propagate out from the ITZ into the cement matrix. These stress concentrations either appeared at points where the heterogeneities were close to the boundary of the body, as was the case for the initial crack propagation into the cement in this analysis, or in areas where two heterogeneities were very close together. The crack initiation in the ITZ around the stiff inclusion propagating out into the cement was the behaviour which was expected.

In concrete, the microcracks at the ITZ eventually propagate into the cement and coalesce into a single macrocrack. These microcracks coalescing into the macrocrack is the point where the softening response of the overall body becomes apparent. If we look at the results for Sample Point 2, shown in Figure 7.8, we can see that the macrocrack has developed and softening is being captured in the load-displacement curve. This is in line with the expected behaviour. The XX stress state, shown for Sample Point 2, has reduced from the peak stress value as the cracks have propagated into the cement matrix and softening has occurred in the specimen. The stresses around the heterogeneities have also reduced from their peak to a lower level at this Sample Point. Sample Point 3, shown in Figure 7.9, shows the development of the macrocrack further into the analysis. As the analysis continued, the stress state in the specimen continued to drop as the macrocrack developed. Figure

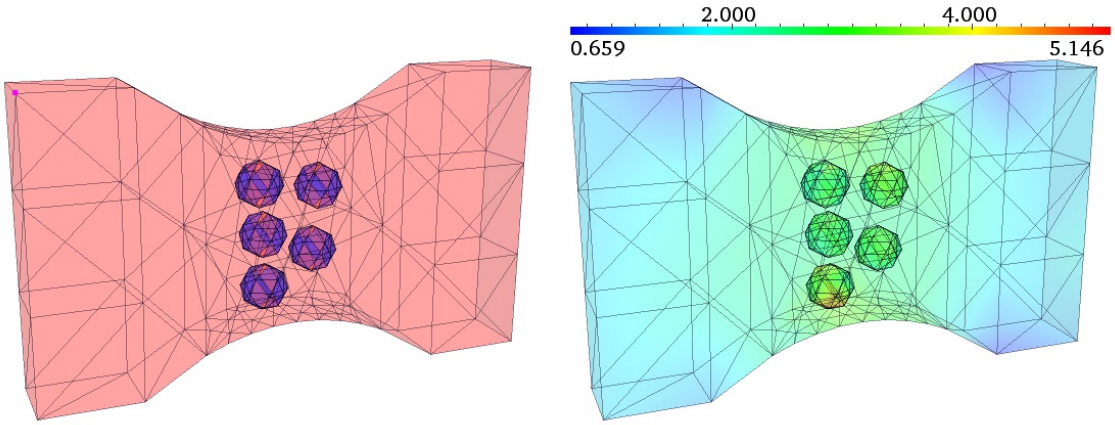

(a) Cracks around inclusions (interface elements represented by blue faces)

(b) XX stress state $\left(\mathrm{N/mm^2}\right)$

Figure 7.7: First numerical test at Sample Point 1 - displacement magnification x 500

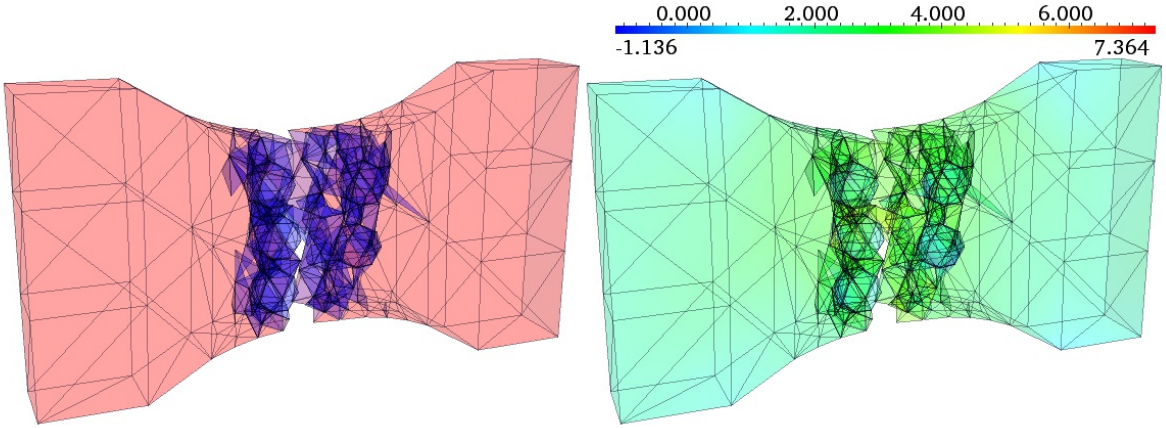

(a) Crack propagation in model (interface elements represented by blue faces)

(b) XX stress state $\left(\mathrm{N/mm^2}\right)$

Figure 7.8: First numerical test at Sample Point 2 - displacement magnification x500

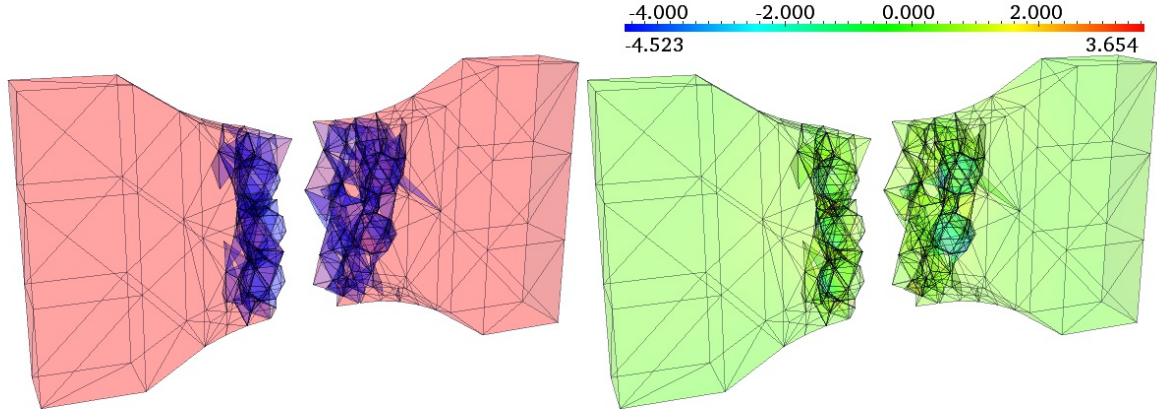

(a) Final macrocrack in model (interface elements represented by blue faces)

(b) XX stress state $\left(\mathrm{N/mm^2}\right)$

Figure 7.9: First numerical test at Sample Point 3 - displacement magnification x500

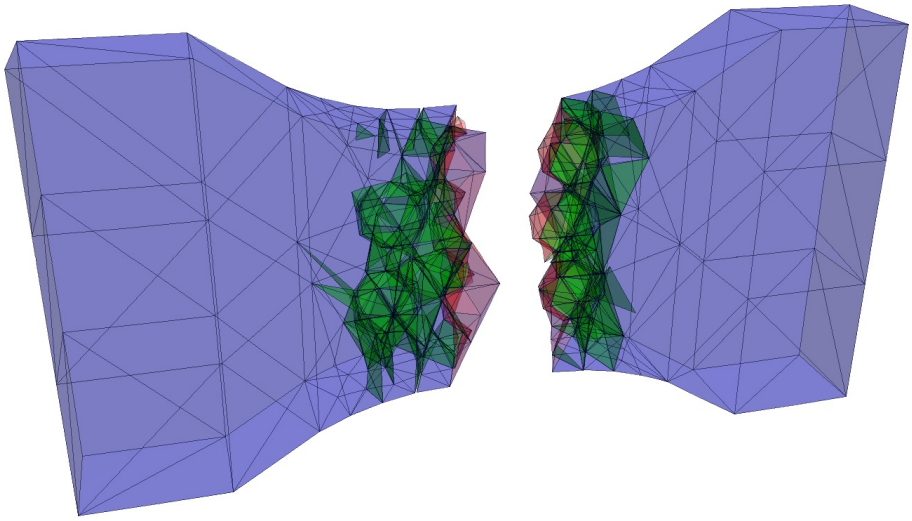

Figure 7.10: First Numerical Test at Sample Point 3 showing active cracks - blue signifies no interface, green signifies elastic interface element, red signifies plastic flow in interface element

7.9a demonstrates an interesting phenomena, which supports one of the major reasons for carrying out analyses with the methodology which has been presented in this thesis. Due to heterogeneities being explicitly resolved by the finite element mesh, the issue of mesh dependence is largely avoided because the heterogeneities will govern the crack path more than the underlying finite element mesh. The results in Figure 7.9a indicate that this theory holds for 3D analyses. In the results presented, the macrocrack has followed the edge of the left three heterogeneities very closely and this has governed, to a large extent, the overall shape of the macrocrack. This phenomena would be even more pronounced if a higher number of heterogeneities were included in the initial mesh.

If we consider the development of the macrocrack throughout the analysis, it can be seen from Figure 7.9 that there is a defined crack where most, if not all, of the non-linear softening behaviour is taking place. Figure 7.10 demonstrates where the active interface elements are located in the mesh at Sample Point 3. As can be seen, the inactive (green) interface elements are still present in the analysis, but are behaving elastically by using the penalty stiffness. The non-linear behaviour is occurring on the surface of the macrocrack (red elements) and the areas outwith the macrocrack have unloaded. This, again, is in line with the expected behaviour. In Chapter 5, a crack insertion methodology was developed to overcome some of the computational inefficiencies of using interface elements. Traditionally, interface

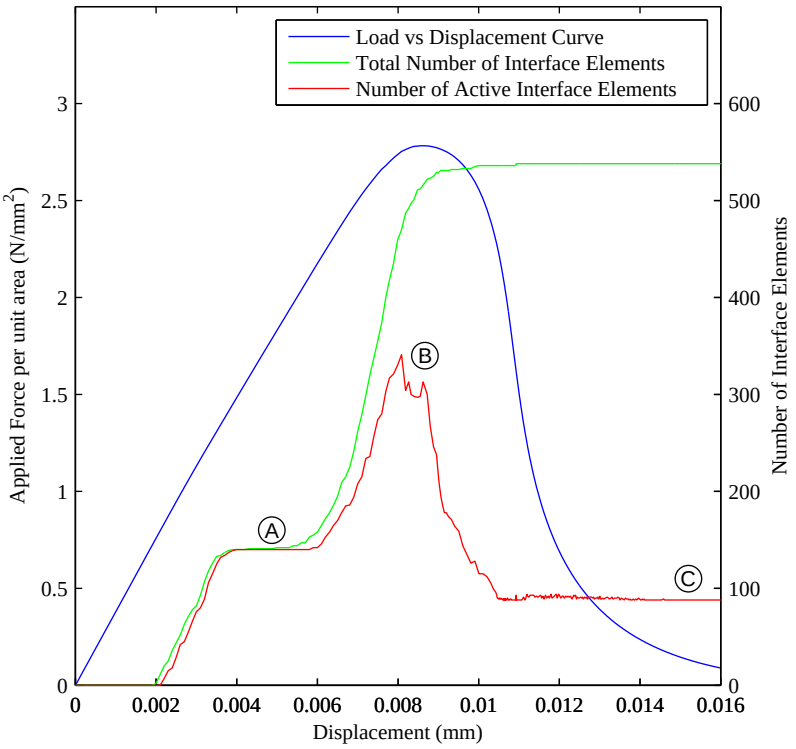

Figure 7.11: Variation in number of interface elements as test progresses

elements would have been inserted into the initial mesh in the central portion of the specimen to ensure any crack propagation was captured. Figure 7.11 demonstrates the number of interfaces elements which have been added to the mesh as the analysis progressed and how the number of active interface elements varies over the course of the analysis. The plateau in the number of interfaces (both total and active) at Point A is the stage in the analysis where discrete cracks have been inserted around the heterogeneities. All of the interface elements are active at this stage as the cracking has initiated in the ITZ without having localised into a macrocrack. Point B is the most computationally intensive time in the entire analysis. Here, the largest number of interface elements in the mesh are active. This is the stage where the cracks are propagating out from the ITZ into the cement matrix. This is demonstrated by this being the time where the rate of increase in the total number of interface elements being inserted into the mesh is greatest. As the analysis progresses, fewer interface elements are active, which is supported by the development of the macrocrack shown earlier. At Point C, towards the end of the analysis, 88 out of 538 (approximately 16%) of the interface elements present in the mesh are active. This supports the use of the crack insertion methodology as it shows that the majority of the interface elements present in an analysis, such as this, will not be required to capture the non-linear behaviour after the formation of a macrocrack.

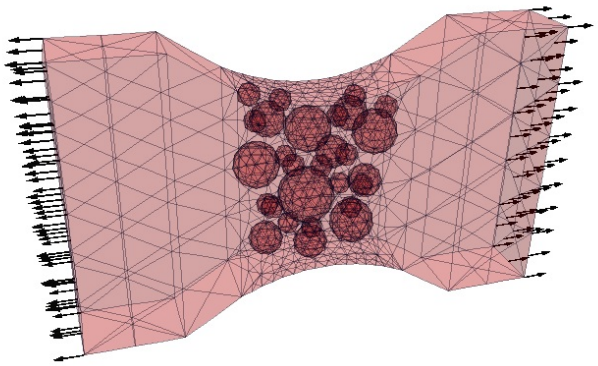

Figure 7.12: Mesh topology showing heterogeneities for second numerical test

Over the course of this analysis, 538 interface elements were inserted into the mesh using the methodology outlined. This caused the total number of nodes in the mesh to increase from 1954 nodes, at the beginning of the analysis, to 7014 nodes by the end of the analysis. Clearly, there has been a substantial increase in the number of nodes, which effects the overall computational cost of a load step. However, it is felt that the proposed methodology still has advantages over the traditional methodology employed for interface elements, where they are included in the analysis from the beginning.

7.3.2 Second Numerical Test

The geometry for the structure of the heterogeneities, as well as the topology of the finite element mesh, for the second numerical test can be seen in Figure 7.12. The boundary conditions applied to the mesh were the same as those for the first numerical test which are outlined in Figure7.5. In this test, a more complex structure has been used to investigate whether the results are consistent with those found for the first numerical test and the methodology performs in a satisfactory manner for larger scale problems. In this test, the heterogeneities were, once again, limited to the central portion of the specimen. Unlike the first numerical test, where the heterogeneities were explicitly placed at their locations, the new structure for the heterogeneities was created using the procedures outlined in Chapter 6. For this structure, the diameter of the heterogeneities range from 3mm to 10mm in 1mm increments, where any particle smaller than 3mm was assumed to be part of the surrounding cement matrix. The volume fraction for the specimen was assumed to be 0.75. The load-displacement graph for the analysis can be seen in Figure 7.14. Considering the results of Sample Point 1, shown in Figure 7.14, we can see that microcracks have initiated around the inclusions at the interfacial transition zone in the expected manner. As with the first numeri-

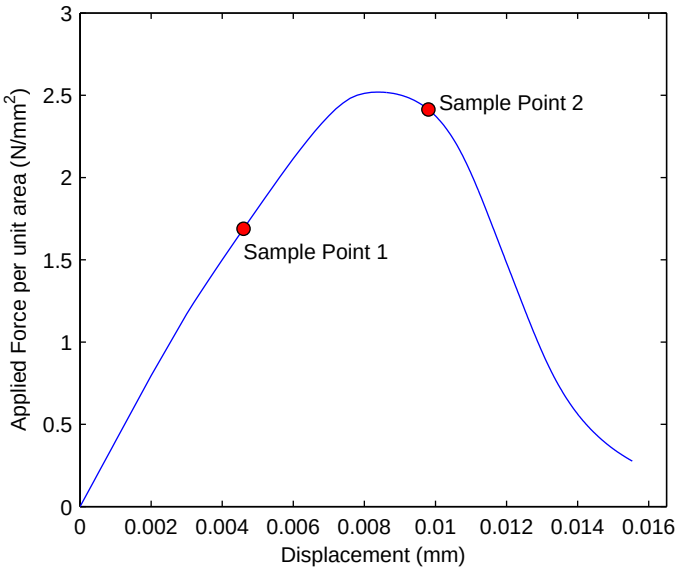

Figure 7.13: Load-displacement curve for second numerical test

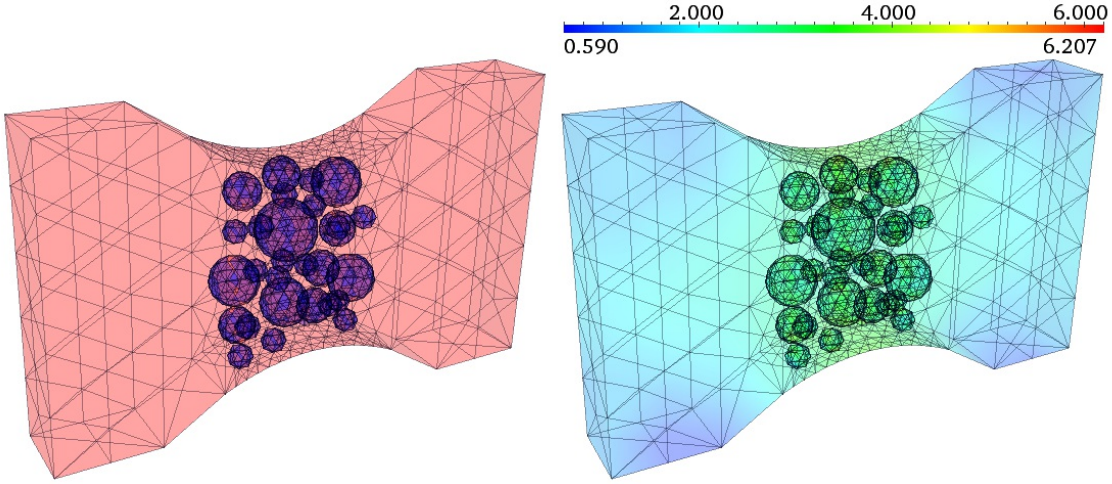

(a) Cracking in the ITZ (interface elements represents by blue faces)

(b) XX stress state $\left(\mathrm{N/mm^2}\right)$

Figure 7.14: Second numerical test at Sample Point 1 - displacement magnification x 1000

cal test, stress concentrations have again appeared at areas where the two heterogeneities are close together and where a heterogeneity and the boundary of the specimen are close. It was in these areas of the cement matrix where cracks then propagated to start the process of the macrocrack formation. Figure 7.15, which is a snapshot of Sample Point 2, demonstrates the macrocrack which has formed in the central region of the specimen. The formation of the macrocrack was preceded by extensive crack propagation into the cement matrix from the ITZ as expected. In this test the macrocrack again closely followed the heterogeneous mesostructure that was present in the specimen. This reinforces the theory that limiting

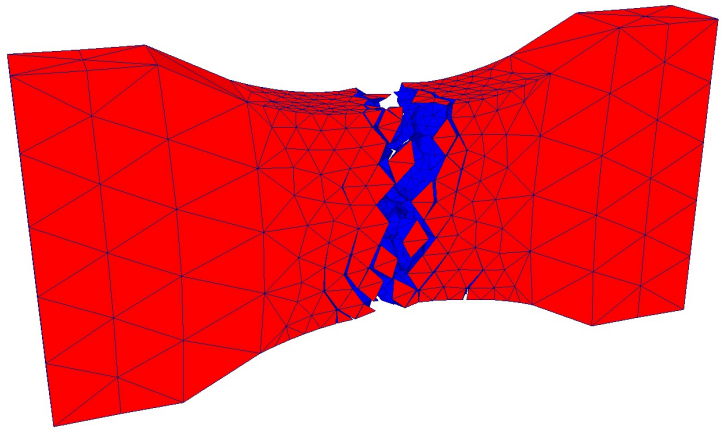

(a) Macrocrack in Model

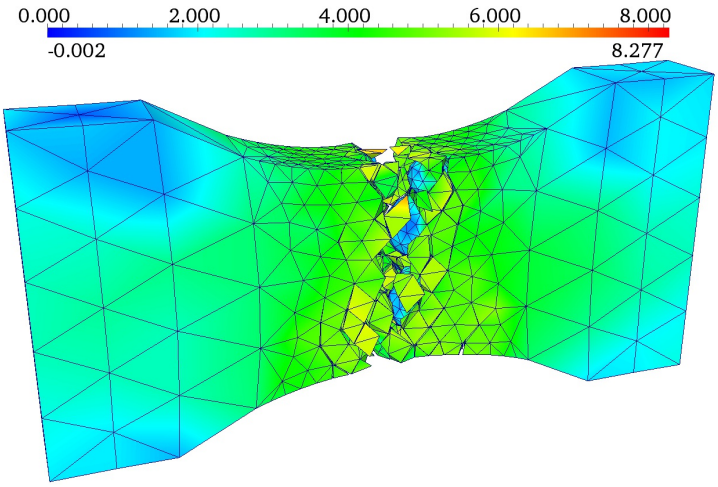

(b) XX stress state $\left(\mathrm{N/mm^2}\right)$

Figure 7.15: Second numerical test at Sample Point 2 - displacement magnification x 1000

cracks to element boundaries is acceptable if the heterogeneities are explicitly resolved by the finite element mesh. In fact, compared to the first numerical test this behaviour was even more pronounced as more heterogeneities were present. Over the course of this analysis, the number of nodes in the mesh increased from 17,000 nodes to 56,000 nodes at Sample Point 2 due to the insertion of 4100 interface elements. This clearly demonstrates the issues with computational efficiency for problems of this size. However, the results provided for the second numerical test show that the computational framework is able to capture the expected phenomenological behaviour of concrete when a more complex heterogeneous structure is used. There are issues with computational time which will need to be solved to allow even more detailed analyses to be performed.

Whilst no direct comparison was able to be made with experimental results, the trends found in the results were able to be compared to the experimental work carried out by van Vliet and van Mier [101], where the tensile response of a dog bone specimen of a similar size to those analysed here was measured. In their work the smallest test specimen was a dog bone with D = 50mm which is the same as the specimens analysed here. However, in their tests the thickness of the specimen was kept constant at 100mm for all sizes investigated, while here it was limited to 25mm due to computational limitations. Even with this difference in specimen properties there are similarities and differences between the results found by the analyses carried out here and their work. In their work, two concrete samples were tested which were cured in dry and wet conditions and gave peak load values of $2.54\text{N}/\text{mm}^2$ and $2.17\text{N}/\text{mm}^2$ respectively. As can be seen from Figure 7.6 and Figure 7.13, this value broadly agrees with the value of peak load that was found when carrying out the numerical tests in this Chapter. It is believed that if further numerical tests were carried out where more inclusions were included in the topology the peak loads found would reduce further to be more in line with the experimental values.

When comparing the post peak response between the numerical tests and experimental results it was found that the numerical tests showed the material to be more brittle than was the case in reality. Van Vliet and van Mier suggested that most of the residual capacity of the dog bone specimen was lost when the end face displacement reached a value of roughly 0.150mm, while in the numerical tests a similar stage was reached at a value of 0.016mm. Clearly there is a large difference between these values but it is believed that there are a number of factors in the numerical analyses which could be altered to ensure the material behaved in a less brittle manner. The major area where the analysis results could be improved in by using more representative values of α, β, γ_1 and γ_2 in the softening equations. These values control the softening response in the numerical model and could be altered to allow a more realistic response to be captured. Whilst the numerical results and experimental results do have some differences it is felt that this is down to the numerical values which have been used in the analysis and improvements could be made by further investigation of the material parameters being used. It is also felt that the comparison with experimental results is initially encouraging and reinforces that the computational framework that has been outlined is sufficient to capture the post-peak behaviour of concrete at the mesoscale.

7.4 Future Improvements to Overall Framework

The results presented in this Chapter have demonstrated the effectiveness of the overall methodology which has been outlined through this entire report. While the results have been promising, it is felt that there are some readily apparent areas in which the implementation could be improved upon to improve the computational efficiency.

The first major improvement which could be made, on a general level, would be to take advantage of parallel processing. The entire framework, which has been outlined throughout this thesis, contains different elements which are suited to parallel implementation. First, the hybrid-Trefftz finite elements, which were outlined, are ideally suited to parallel implementation [52] and the calculation of the stress degrees of freedom lends itself particularly well to parallel processing. Second, the programs which have been used to carry out the non-linear analyses, such as MOAB and PETSc, are both optimised for parallel processors. In the analyses performed, a majority of the computational time was spent either solving the system of equations or building the global stiffness matrix, both of which are processes required by PETSc. Therefore, utilising the support within PETSc for parallel processing could dramatically reduce the amount of time required for the analyses to be performed. This would then allow much larger problems to be analysed where much more complex heterogeneous structures are resolved by the finite element mesh. It would also allow analyses to be performed on problems of larger dimensions. To further implement parallel processing some thought would need to be given on how to accurately partition the mesh. This would involve assigning sections of the mesh to different processors to allow the computational effort to be equally divided between processors.

7.5 Conclusions

This Chapter has presented the numerical results obtained by combining the work carried out in the previous Chapters. The methodology for carrying out a single load step was presented and the material properties used in the analyses were outlined. In particular, the variables used in the constitutive law for the interface element were related to the fracture energy of the material being analysed. Two different numerical tests were presented. These tests presented the tensile response of concrete in a realistic manner by showing how cracking initiated and developed in the specimen. As was the case in physical experiments, the cracks initiated

around the heterogeneities resolved by the finite element mesh, before propagating out into the cement matrix to produce a macrocrack. The theory of heterogeneities in the mesh playing a more important role in the propagation of cracks than the underlying mesh was also supported by these tests. There is a realisation by the author that the results presented in this Chapter are a proof of concept for the methodology. Clearly, work needs to be carried out to further increase the computational efficiency to allow larger problems to be examined, which would allow the methodology to be validated against experimental results.

Chapter 8

Conclusions

The work in this thesis has presented a computational framework for analysing fracture in heterogeneous material at the mesoscale in three dimensions. In developing this framework, a wide range of issues have been investigated to ensure a solution scheme was produced which gives robust and realistic results. There were several distinct novel aspects to the work that was presented in this thesis. First, the use of hybrid-Trefftz stress elements enabled an accurate description of the complex stress state to be obtained, which is of paramount importance for capturing crack initiation. The use of these elements also overcame the issue of traction oscillations when using interface elements. Second, a new crack insertion methodology was presented, which utilises properties of the hybrid-Trefftz finite elements and insert discrete cracks into the mesh as the analysis progresses. Finally, to produce an efficient procedure which created mesostructure geometries which produced good quality finite element meshes, a new particle packing method was developed called the Maximum Level Set method.

The initial work focused on the derivation of the hybrid-Trefftz stress element which are used for the bulk elements in the mesh. As fracture is a stress-driven process, an accurate approximation of the stress state in the model was vitally important. The hybrid-Trefftz stress element approximates the stresses over the domain of the element, while the displacements are approximated over the boundary. The stresses can be approximated to a much higher order by using specially designed Trefftz functions which satisfy equilibrium *a priori*. Furthermore, an additional benefit of using the hybrid-Trefftz stress elements was its ability to overcome the issue of inconsistencies in the traction field when using interface elements for the discrete cracks in the material. The full derivation of the hybrid-Trefftz stress element

was presented from first principles, a demonstration was given on how to construct the Trefftz functions and simple three dimensional numerical tests were performed, which showed the element formulation produces the expected results.

To model the discrete cracking, interface elements were used with all cracks being restricted to element boundaries. This is justified for the problems being analysed because the heterogeneous mesostructure will play a much more important role in the crack initiation and propagation than the underlying finite element mesh. All non-linear behaviour was restricted to the interface elements, which meant the hybrid-Trefftz stress elements were assumed to be linear-elastic throughout the analysis. The formulation of the continuous interface element was presented and its incorporation with the hybrid-Trefftz stress elements was outlined showing how compatibility between elements was achieved. In interface elements, the tractions transmitted across the crack are related to the relative displacements of the crack by a constitutive law. Here, a plasticity-based constitutive law, formulated by Winnicki, was investigated to capture the non-linear softening behaviour and mixed mode fracture of concrete. Its computational implementation using an implicit stress return algorithm was outlined and the associated algorithmic stiffness was derived, which was necessary to ensure quadratic rates of convergence for the non-linear system of equations. Simple three dimensional numerical results illustrating the performance of the interface element were presented. These results showed that the expected softening response and Mode I and Mode II fracture were able to be captured and quadratic convergence was achieved.

Rather than including interface elements from the start of an analysis, a new methodology was developed to dynamically insert interface elements into a 3D mesh as the analysis progresses. This exploited the fact that the displacement field for hybrid-Trefftz stress elements are approximated separately on adjacent faces, which is a consequence of element compatibility being enforced in the weak sense. The full computational implementation was outlined for the crack insertion methodology, with both the computational procedures and data storage issues being discussed. To ensure the data storage was handled efficiently and robustly, the computational package MOAB was used. It is noted that the crack insertion methodology outlined, creates large numbers of degrees of freedom as faces are treated independently. This large increase has an effect on the computational efficiency of the resulting framework, but there are clear advantages in the accurate modelling of crack initiation. Results were presented for three numerical problems of varying complexity which showed the crack insertion algorithm produced acceptable results.

To create a mesostructure which produced good quality finite element meshes, whilst also being efficient, a novel particle packing method, known as the Maximum Level Set method, was presented. This method initially over saturated the volume of the specimen with random grid points. It then inserted particles, in a sequential manner, at the random grid point with the largest Level Set value. The Level Set values were then updated at the remaining grid points to take account of the new mesostructure. This method was compared to the conventional method, Random Sequential Addition, and showed that is was more efficient for creating mesostructures if a high Volume Fraction was required. It also ensured there were greater minimum distances between particles, which would generally ensure better quality meshes were produced. Results were presented showing the methodology was able to produced heterogeneous structures for arbitrary shaped volumes by utilising the computational packages Cubit and CGAL. It was also noted that the use of these packages could allow the use of non-spherical inclusions to be implemented into the formulation to further improve the mesostructures produced.

Finally, the full computational framework was applied to larger scale problems. The procedure for carrying out an entire load step and combining both the hybrid-Trefftz stress elements and interface elements was discussed. The procedure for how the crack insertion algorithm was integrated into the framework was also presented. In the Winnicki law, used in the interface elements, there were certain variables which were user defined. However, it was shown that the values α and β could be related to the fracture energy of the material to ensure realistic values were used. Numerical tests were presented using simplified mesostructure geometries, which ensured the analyses were completed in a suitable time frame. The results presented show proof of concept for the computational framework with non-linear softening occurring in the expected manner and the correct behaviour for the propagation and evolution of cracks being observed. The cracking initiated around the stiff inclusions in the mesh, then propagated out through the surrounding cement matrix, before finally forming a macrocrack where all active interface elements were present. It was found that the crack path was largely determined by the stiff inclusions in the mesh. This suggested that limiting the cracks to element boundaries was acceptable in cases where heterogeneities are explicitly resolved by the finite element mesh.

The work presented in this thesis has produced a computational framework which is suitable for analysing problems of fracture in heterogeneous materials. While the result presented demonstrate the overall formulation has been effective, further work could be carried out to

improve it. The majority of the work required should be focused on making the implementation more computationally efficient by utilising parallel processing and high performance computing. This would then allow more realistic problems to be studied and full validation of the methodology against experimental results to be undertaken.

As a final note, the framework presented is suitable for modification to allow dynamic analysis to be undertaken. Work has been carried out to develop hybrid-Trefftz stress elements so they can be used in dynamic analyses, these elements are usually known as hybrid-mixed elements, but this work requires more research for 3D problems to ensure robust solutions are obtained. The crack insertion algorithm, and the use of interface elements, could still be used in these cases and it is believed that this would be an interesting area of future research. A further improvement would be to modify the methodology to allow problems involving large displacements to be analysed. Work has been carried out in this area by different authors [43, 52, 84] where different methods, such as the corotational formulation, have been proposed to take account of this issue and it would be interesting to incorporate these methods into the proposed framework.

Appendix A

Trefftz Functions for $\mathbf{S_v}$

In the following matrices λ and μ are the standard Lamé coefficients.

1st Order terms for $\mathbf{S_v}$ matrix:

$$\mathbf{S_v^T} = \begin{bmatrix} \lambda+2\mu & \lambda & \lambda & 0 & 0 & 0 \\ \lambda & \lambda+2\mu & \lambda & 0 & 0 & 0 \\ \lambda & \lambda & \lambda+2\mu & 0 & 0 & 0 \\ 0 & 0 & 0 & 2\mu & 0 & 0 \\ 0 & 0 & 0 & 0 & 2\mu & 0 \\ 0 & 0 & 0 & 0 & 0 & 2\mu \end{bmatrix} \tag{A.1}$$

2nd Order terms for $\mathbf{S_v}$ matrix:

$$\mathbf{S_v^T} = \begin{bmatrix} 2\lambda x+4\mu x & 2\lambda x & 2\lambda x & -2\lambda y-4\mu y & 0 & 0 \\ \lambda y+2\mu y & \lambda y & \lambda y & -\lambda x & 0 & 0 \\ \lambda z+2\mu z & \lambda z & \lambda z & 0 & 0 & -\lambda x \\ 0 & 0 & 0 & -2\mu y & 0 & 2\mu z \\ \lambda x & \lambda x+2\mu x & \lambda x & -\lambda y & 0 & 0 \\ 2\lambda y & 2\lambda y+4\mu y & 2\lambda y & -2\lambda x-4\mu x & 0 & 0 \\ \lambda z & \lambda z+2\mu z & \lambda z & 0 & \mu y & -\mu x-\lambda x \\ 0 & 0 & 0 & -2\mu x & 2\mu z & 0 \\ \lambda x & \lambda x & \lambda x+2\mu x & -\mu y-\lambda y & 0 & \mu z \\ 0 & 0 & 0 & 0 & 2\mu y & -2\mu x \\ \lambda y & \lambda y & \lambda y+2\mu y & -\mu x-\lambda x & \mu z & 0 \\ 2\lambda z & 2\lambda z & 2\lambda z+4\mu z & 0 & 0 & -2\lambda x-4\mu x \end{bmatrix} \tag{A.2}$$

3rd Order terms for $\mathbf{S_v}$ matrix:

$$\mathbf{S_v^T} = \begin{bmatrix}
0 & 0 & 0 & t_4 & 0 & -t_5 \\
0 & 0 & 0 & -t_5 & 0 & t_4 \\
t_6 t_{164} & -t_{21} & \lambda t_6 t_{165} & -t_{27} & 0 & 2\lambda t_6 t_{29} t_{28} \\
t_{31} & t_{27} & t_{27} & t_{12} - t_{32} - t_{33} & t_{35} & -t_{36} \\
t_{37} - 9t_{16} + 6t_{12} - 12t_{24} & 3t_{38} & t_{37} + t_{39} + 6t_{24} & 0 & 0 & -6t_{29} t_{28} \\
t_{40} & t_{34} & t_{34} & -t_{36} & -t_{42} & t_{12} - t_{43} - t_{44} \\
0 & 0 & 0 & t_{46} & -t_{47} & 0 \\
t_{27} & t_{31} & t_{27} & -t_{33} - t_{32} + t_{22} & -t_{40} & -t_{48} \\
3t_6 t_{166} & 3t_6 t_{167} & 3t_6 t_{168} & 6t_{26} + 12t_{30} & 0 & 6t_6 t_{28} t_{171} \\
t_{53} & t_{54} & t_{53} & -t_{40} & -t_{55} - t_{45} + t_{22} & -t_{42} \\
-t_{56} + t_{39} + t_{25} & -t_{56} + t_{16} - t_{57} + t_{25} & -t_{56} - t_{16} - t_{25} & -t_{58} & t_{59} & 2t_{41} t_{28} \\
0 & 0 & 0 & -t_{47} & -t_{46} & 0 \\
0 & 0 & 0 & 0 & -t_{60} & t_{61} \\
t_{23} - t_{39} - t_{25} & t_{38} & t_{23} + t_{16} + t_{57} & 0 & 0 & -t_{34} \\
t_6 t_{170} & -t_{21} & t_6 t_{169} & -t_{27} - t_{58} & t_{59} & 2t_6 t_{28} \left[t_{14} + 2t_{52} + t_8 \right] \\
0 & 0 & 0 & 0 & -t_{61} & -t_{60} \\
t_{34} & t_{34} & t_{40} & -t_{48} & -t_{62} & -t_{44} - t_{43} + t_{24} \\
t_{53} & t_{53} & t_{54} & t_{35} & -t_{55} - t_{45} + t_{24} & -t_{62}
\end{bmatrix} \tag{A.3}$$

$t_1 = yy$
$t_2 = zz$
$t_3 = t_2$
$t_6 = 3\mu(t_1 - t_3)$
$t_8 = \mu yz$
$t_9 = 6t_8$
$t_{10} = 1/\mu$
$t_{11} = \lambda t_1$
$t_{13} = \mu t_{11}$
$t_{14} = \lambda\lambda$
$t_{15} = t_{14}t_2$
$t_{16} = 3t_{15}$
$t_{17} = xx$
$t_{18} = t_{14}t_{17}$
$t_{19} = \mu t_{17}$
$t_{20} = \lambda t_{19}$
$t_{21} = \mu\mu$
$t_{23} = 2t_{21}t_1$
$t_{24} = \lambda t_2$
$t_{25} = \mu t_{24}$
$t_{26} = 4t_{25}$
$t_{30} = t_{15}$
$t_{32} = t_{21}t_{17}$
$t_{36} = t_{10}(-t_{13} - t_{30} + t_{18}3t_{20}2t_{32})$
$t_{38} = \mu t_1$
$t_{40} = \lambda t_{17}$
$t_{41} = \mu t_2$
$t_{42} = 2t_{41}$
$t_{46} = xy$
$t_{47} = \lambda t_{46}$
$t_{48} = 2t_{47}$
$t_{49} = xz$
$t_{51} = \lambda + 2\mu$
$t_{56} = \mu t_{46}$
$t_{58} = t_{48} + 4t_{56}$
$t_{59} = 3t_{41}$
$t_{60} = 2t_{24}$
$t_{62} = \mu t_{49}$
$t_{65} = 2\lambda t_{49}$
$t_{66} = -2t_{62} - t_{65}$
$t_{67} = yz$
$t_{69} = 2t_{51}t_{67}$
$t_{70} = 3t_{40}$
$t_{76} = (t_{17} - t_3)\lambda$
$t_{78} = 3t_{24}$
$t_{84} = t_{65} + 4t_{62}$
$t_{85} = \lambda + \mu$
$t_{87} = 2t_{85}t_{46}$
$t_{88} = 3t_{38}$
$t_{89} = 2t_{11}$
$t_{91} = 3t_{19}$
$t_{92} = t_{91} - t_{59}$
$t_{93} = 6t_{62}$
$t_{96} = 2t_{85}t_{67}$
$t_{98} = 2t_{20}$
$t_{99} = t_2t_{21}$
$t_{111} = 2t_{99}$
$t_{119} = \mu\lambda$
$t_{127} = 2\lambda yz$
$t_{129} = t_{127} + 4t_8$
$t_{130} = 2t_{40}$
$t_{132} = t_{40}$
$t_{134} = 2t_{19}$
$t_{138} = 2t_{56}$
$t_{139} = 2t_8$
$t_{142} = 6t_{56}$
$t_{146} = 3\mu(-t_1 + t_{17})$
$t_{163} = 2t_{51}t_{46}$
$t_{164} = t_7 + t_{10} - t_{11} - t_{13} + t_{15} + t_{18}$
$t_{165} = t_{22} - t_{16} - t_{23} - t_{12} - t_{25}$
$t_{166} = 7t_{17} + t_{10} - t_{11} - t_{49} + t_7 + 4t_{50}$
$t_{167} = t_{17} + t_{19} - t_{11} - 4t_{13} + t_7 - 4t_{20} + t_{15}$
$t_{168} = -3t_{17} - t_9 - t_{11} - t_{49} + t_7 - t_{51}$
$t_{169} = t_7 - t_9 - t_{11} - t_{13} - t_{51} + t_{15} + 2t_{17}$
$t_{170} = t_7 + t_{10} - t_{11} - t_{13} + t_{51} + t_{18}$
$t_{171} = 2t_{14} + t_8 + 3t_{52}$

4th Order terms for $\mathbf{S_v}$ matrix:

$$\mathbf{S_v^T} = \begin{bmatrix}
\frac{2}{3}t_7 & \frac{2}{3}z[-t_{10}+t_{12}-t_{14}] & \frac{2}{3}t_{21} & \dots \\
-t_{44} & y[t_{11}+t_{10}+t_{46}] & y[-t_{12}+t_{10}+t_{49}-t_{50}] & \dots \\
-\frac{2}{3}t_{44} & \frac{2}{3}y[t_{11}+t_{10}+t_{49}] & \frac{2}{3}y[-t_{12}+t_{10}-t_{46}] & \dots \\
y[-t_{12}+t_{65}-t_{50}+t_{66}] & y[t_{11}+t_{65}+t_{46}] & t_{74} & \dots \\
z[-t_{10}+t_{65}-t_{87}+t_{66}] & t_{91} & t_{93} & \dots \\
\frac{2}{3}x[t_{12}+t_{26}+t_{19}] & \frac{2}{3}x[t_{12}-t_{65}-t_{25}] & -\frac{2}{3}t_{105} & \dots \\
\frac{2}{3}t_{95} & -\frac{2}{3}t_{120} & \frac{2}{3}x[t_{10}-t_{65}-t_{25}] & \dots \\
0 & 0 & 0 & \dots \\
0 & 0 & 0 & \dots \\
0 & 0 & 0 & \dots \\
\frac{2}{3}y[-t_{12}+t_{65}-t_{46}] & \frac{2}{3}y[t_{11}+t_{65}+t_{66}] & \frac{2}{3}t_{74} & \dots \\
x[t_{12}+t_{26}+t_{25}] & x[t_{12}-t_{65}+t_{19}-t_{163}] & -t_{105} & \dots \\
0 & 0 & 0 & \dots \\
t_7 & z[-t_{10}+t_{12}+t_{19}-t_{87}] & t_{63} & \dots \\
\frac{2}{3}z[-t_{10}+t_{65}-t_{14}] & \frac{2}{3}t_{91} & \frac{2}{3}t_{192} & \dots \\
0 & 0 & 0 & \dots \\
t_{195} & -t_{120} & x[t_{10}-t_{65}+t_{49}-t_{163}] & \dots \\
0 & 0 & 0 & \dots
\end{bmatrix}$$

$$
\begin{bmatrix}
0 & -2y\left[t_9+t_{25}+t_{26}\right] & -4t_{31}+\frac{2}{3}t_{36}+\frac{1}{6}t_{38} \\
0 & -t_{21} & 0 \\
0 & -\frac{2}{3}t_{65} & 0 \\
x\left[-t_{19}+t_{24}-t_{12}-t_{10}-t_{75}\right] & t_{79}-t_{82}-3t_{83}+t_{85} & 0 \\
0 & 0 & -t_{95} \\
2y\left[-t_{14}-t_9-t_{26}\right] & 0 & -4t_{111}-2t_{113}+t_{115}+t_{116} \\
0 & 0 & -\frac{2}{3}t_{93} \\
t_{128}-12t_{130} & 0 & t_{133}-12t_{111} \\
t_{136}-t_{79} & 0 & t_{127}-3t_{130} \\
t_{141}-12t_{143} & t_{133}-12t_{81} & 0 \\
2x\left[-t_{11}-t_{14}-t_9\right] & t_{115}+t_{116}-2t_{83}-4t_{81} & 0 \\
y\left[-t_{75}-t_{10}+t_{168}-t_{66}-t_{65}\right] & 0 & t_{79}+t_{85}-3t_{113}-t_{136} \\
-t_{82}+t_{79} & -t_{175}+3t_{143} & 0 \\
0 & y\left[t_{168}-t_{10}-t_{49}-3t_{24}-t_{65}\right] & -3t_{36}-t_{185}+t_{38}+t_{34} \\
0 & 0 & -\frac{2}{3}t_{195} \\
0 & t_{185}-t_{175} & t_{127}-3t_{199} \\
0 & 0 & -t_{192} \\
0 & -12t_{199}+t_{128} & t_{141}-12t_{31}
\end{bmatrix}
\tag{A.4}
$$

$t_1 = \lambda z$
$t_2 = z^2$
$t_3 = t_2$
$t_4 = y^2$
$t_5 = 3t_4$
$t_7 = (-t_3 + t_5)t_1$
$t_9 = \lambda t_2$
$t_{10} = 3t_9$
$t_{11} = t_4\lambda$
$t_{12} = 3t_{11}$
$t_{13} = \mu t_2$
$t_{14} = 2t_{13}$
$t_{18} = t_4\mu$
$t_{19} = 6t_{18}$
$t_{21} = z(t_9 + t_{12} + t_{19})$
$t_{23} = x^2$
$t_{24} = \mu t_{23}$
$t_{25} = t_{24}$
$t_{26} = \lambda t_{23}$
$t_{30} = xt_4$
$t_{31} = \mu t_{30}$
$t_{33} = xt_{23}$
$t_{34} = \lambda t_{33}$
$t_{36} = \lambda t_{30}$
$t_{38} = \mu t_{33}$
$t_{41} = \lambda y$
$t_{42} = 3t_2$
$t_{44} = t_{41}(t_4 - t_{42})$
$t_{46} = 2t_{18}$
$t_{49} = 6t_{13}$
$t_{50} = 4t_{18}$
$t_{63} = z(t_{14} + t_9 + t_{12})$
$t_{65} = 3t_{26}$
$t_{66} = 6t_{24}$
$t_{72} = 3t_{23}$
$t_{74} = t_{41}(-t_4 + t_{41})$
$t_{75} = 3t_{13}$
$t_{78} = zt_2$
$t_{79} = \mu t_{78}$
$t_{80} = zt_{23}$
$t_{81} = \mu t_{80}$
$t_{82} = 3t_{81}$
$t_{83} = \lambda t_{80}$
$t_{85} = \lambda t_{78}$
$t_{87} = 4t_{13}$
$t_{91} = t_1(-t_3 + t_{72})$
$t_{93} = z(t_9 + t_{65} + t_{14})$
$t_{95} = x(t_{49} + t_{10} + t_{26})$
$t_{103} = x\lambda$
$t_{105} = t_{103}(-t_5 + t_{23})$
$t_{110} = zt_4$
$t_{111} = \mu t_{110}$
$t_{113} = \lambda t_{110}$
$t_{115} = \frac{2}{3}t_{85}$
$t_{116} = \frac{1}{8}t_{79}$
$t_{120} = t_{103}(-t_{42} + t_{23})$
$t_{127} = \mu t_4 y$
$t_{128} = 4t_{127}$
$t_{130} = \mu t_2 y$
$t_{133} = 4t_{79}$
$t_{136} = 3t_{111}$
$t_{141} = 4t_{38}$
$t_{143} = \mu t_2 x$
$t_{163} = 4t_{24}$
$t_{168} = t_{18}$
$t_{175} = t_{38}$
$t_{185} = 3t_{31}$
$t_{192} = z(t_9 + t_{65} + t_{66})$
$t_{195} = x(t_{10} + t_{26} + t_{25)}$
$t_{199} = \mu y t_{23}$

Appendix B

Closest Point Projection Derivation

Taking the two linearized equations:

$$\mathbf{R_1}^{n+1} = \mathbf{R_1}^n + \frac{\partial \mathbf{R_1}}{\partial \mathbf{t}}\delta\mathbf{t} + \frac{\partial \mathbf{R_1}}{\partial \Delta\lambda}\delta\lambda = 0 \tag{B.1}$$

$$R_2^{n+1} = R_2^n + \frac{\partial F}{\partial \mathbf{t}}\delta\mathbf{t} + \frac{\partial F}{\partial \Delta\lambda}\delta\lambda = 0 \tag{B.2}$$

An equation for $\delta\mathbf{t}$ can be found using B.1:

$$\delta\mathbf{t} = \left[\frac{\partial \mathbf{R_1}}{\partial \mathbf{t}}\right]^{-1}\left[-\mathbf{R_1}^n - \frac{\partial \mathbf{R_1}}{\partial \Delta\lambda}\delta\lambda\right] \tag{B.3}$$

which can then be substituted into B.2to give:

$$R_2^n - \frac{\partial F}{\partial \mathbf{t}}\left[\frac{\partial \mathbf{R_1}}{\partial \mathbf{t}}\right]^{-1}\mathbf{R_1}^n - \frac{\partial F}{\partial \mathbf{t}}\left[\frac{\partial \mathbf{R_1}}{\partial \mathbf{t}}\right]^{-1}\frac{\partial \mathbf{R_1}}{\partial \Delta\lambda}\delta\lambda + \frac{\partial F}{\partial \Delta\lambda}\delta\lambda = 0 \tag{B.4}$$

This equation can then be rearranged to find an equation for the iterative change in plastic multiplier, $\delta\lambda$ which is shown in Chapter 4. In the Chapter there are various terms which are outlined. These are detailed in full below to demonstrate where the final equations have been calculated from.

$$\frac{\partial \mathbf{R_1}}{\partial \mathbf{t}} = \mathbf{I} + \Delta\lambda\mathbf{D^e}\frac{\partial}{\partial \mathbf{t}}\mathbf{m} = \mathbf{I} + \Delta\lambda\mathbf{D^e}\frac{\partial^2 F}{\partial \mathbf{t}^2} = \Xi \tag{B.5}$$

$$\frac{\partial \mathbf{R_1}}{\partial \dot{\lambda}} = \mathbf{K_e}\frac{\partial F}{\partial \mathbf{t}} = \mathbf{K_e}\mathbf{m} \tag{B.6}$$

$$\frac{\partial R_2}{\partial \mathbf{t}} = \mathbf{m} \tag{B.7}$$

$$\frac{\partial R_2}{\partial \Delta\lambda} = \frac{\partial R_2}{\partial \kappa}\|\mathbf{m}\| = \frac{\partial F}{\partial \kappa}\|\mathbf{m}\| = -h \tag{B.8}$$

$$\mathbf{m} = \frac{\partial F}{\partial \mathbf{t}} = \begin{bmatrix} \frac{\partial F}{\partial t_n} \\ \frac{\partial F}{\partial t_{s_1}} \\ \frac{\partial F}{\partial t_{s_1}} \end{bmatrix} = \begin{bmatrix} 1 \\ \frac{2C_0 t_{s_1}}{B^2(\kappa)} \\ \frac{2C_0 t_{s_2}}{B^2(\kappa)} \end{bmatrix} \tag{B.9}$$

$$\frac{\partial^2 F}{\partial \mathbf{t}^2} = \begin{bmatrix} 0 & 0 & 0 \\ 0 & \frac{2C_0}{B^2(\kappa)} & 0 \\ 0 & 0 & \frac{2C_0}{B^2(\kappa)} \end{bmatrix} \tag{B.10}$$

Appendix C

Algorithmic Stiffness Derivation

$$\delta \mathbf{t}^{n+1} = \mathbf{D}^{\mathbf{e},n+1}\left[\delta \mathbf{g}^{n+1} - \delta \mathbf{g}_{\mathbf{p}}^{n+1}\right] \tag{C.1}$$

where

$$\delta \mathbf{g}_{\mathbf{p}}^{n+1} = \Delta\lambda^{n+1}\mathbf{m}^{n+1} \tag{C.2}$$

where

$$\mathbf{m} = \frac{\partial F}{\partial \mathbf{t}} = \begin{bmatrix} \frac{\partial F}{\partial t_n} \\ \frac{\partial F}{\partial t_{s_1}} \\ \frac{\partial F}{\partial t_{s_1}} \end{bmatrix} = \begin{bmatrix} 1 \\ \frac{2C_0 t_{s_1}}{B^2(\kappa)} \\ \frac{2C_0 t_{s_2}}{B^2(\kappa)} \end{bmatrix} \tag{C.3}$$

If the increment of plastic relative displacements are linearized then the following equation is found:

$$\delta \mathbf{g}_{\mathbf{p}}^{n+1} = \frac{\partial \mathbf{g}_{\mathbf{p}}^{n+1}}{\partial \mathbf{t}}\delta \mathbf{t} + \frac{\partial \mathbf{g}_{\mathbf{p}}^{n+1}}{\partial \Delta\lambda}\delta\lambda = \Delta\lambda^{n+1}\frac{\partial \mathbf{m}^{n+1}}{\partial \mathbf{t}^{n+1}}\delta \mathbf{t}^{n+1} + \delta\lambda^{n+1}\mathbf{m}^{n+1} \tag{C.4}$$

This can then be substituted back into C.1 to give:

$$\delta \mathbf{t}^{n+1} = \mathbf{D}^{\mathbf{e}}\delta \mathbf{g}^{n+1} - \mathbf{D}^{\mathbf{e}}\Delta\lambda^{n+1}\frac{\partial \mathbf{m}^{n+1}}{\partial \mathbf{t}^{n+1}}\delta \mathbf{t}^{n+1} - \mathbf{D}^{\mathbf{e}}\mathbf{m}^{n+1}\delta\lambda^{n+1} \tag{C.5}$$

This equation then be rearranged for $\delta \mathbf{t}^{n+1}$ and divided through by $\mathbf{D}^{\mathbf{e}}$ to give:

$$\delta \mathbf{t}^{n+1} = \left[\mathbf{D}^{\mathbf{e}-1} + \Delta\lambda^{n+1}\frac{\partial \mathbf{m}^{n+1}}{\partial \mathbf{t}^{n+1}}\right]^{-1}\left[\delta \mathbf{g}^{n+1} - \delta\lambda^{n+1}\mathbf{m}^{n+1}\right] \tag{C.6}$$

As was done in the procedure for the CPP, the yield surface can also be linearized:

$$\frac{\partial F^{n+1}}{\partial \mathbf{t}^{n+1}}\delta \mathbf{t}^{n+1} + \frac{\partial F^{n+1}}{\partial \Delta\lambda}\delta\lambda^{n+1} = 0 \;\text{ where }\; \frac{\partial F^{n+1}}{\partial \Delta\lambda} = \frac{\partial F^{n+1}}{\partial \kappa}\frac{\partial \kappa}{\partial \Delta\lambda} = \frac{\partial F^{n+1}}{\partial \kappa}\left\|\mathbf{m}^{n+1}\right\| \tag{C.7}$$

which gives the equation for $\delta\lambda^{n+1}$:

$$\delta\lambda^{n+1} = \frac{\mathbf{m}^{\mathrm{T}}\Xi\delta\mathbf{g}^{n+1}}{h+\mathbf{m}^{\mathrm{T}}\Xi\mathbf{m}} \tag{C.8}$$

where

$$h = -\frac{\partial F^{n+1}}{\partial\kappa}\|\mathbf{m}\| \quad \& \quad \Xi = \left[\mathbf{K}_{\mathbf{e}}^{-1} + \Delta\lambda^{n+1}\frac{\partial\mathbf{m}^{n+1}}{\partial\mathbf{t}^{n+1}}\right]^{-1} \tag{C.9}$$

This equation can then be substituted back into C.6 to give:

$$\delta\mathbf{t}^{n+1} = \Xi\left[\delta\mathbf{g}^{n+1} - \frac{\mathbf{m}^{\mathrm{T}}\Xi\mathbf{m}}{h+\mathbf{m}^{\mathrm{T}}\Xi\mathbf{m}}\delta\mathbf{g}^{n+1}\right] \tag{C.10}$$

So the algorithmic stiffness, which is the change in tractions due to the change in relative displacements, is given by:

$$\mathbf{D}^{\mathbf{ep}} = \left.\frac{\delta\mathbf{t}}{\delta\mathbf{g}}\right|_{n+1} = \Xi - \frac{\Xi\mathbf{m}\mathbf{m}^{\mathrm{T}}\Xi}{h+\mathbf{m}^{\mathrm{T}}\Xi\mathbf{m}} \tag{C.11}$$

References

[1] "Alkali-silica reaction in concrete".

[2] "\textsc{Cgal}, {C}omputational {G}eometry {A}lgorithms {L}ibrary".

[3] "\textsc{Cubit}".

[4] "Computing and Estimating the Rate of Convergence". Retrieved 05/08/2013 from http://www.math-cs.gordon.edu/courses/mat342/handouts/rate.pdf.

[5] "Sulfate attack in concrete and mortar".

[6] M. R. Arruda & L. M. S. Castro. "Static and dynamic physically non-linear analysis of concrete structures using a hybrid mixed finite element model". *Advances in Engineering Software*, 65:112–131 (2013).

[7] H. Askes, M. A. Guti & A. Rodr. "Novel nonlocal continuum formulations . Part 1 : gradient elasticity based on nonlocal displacements and nonlocal strains". (June) (2006).

[8] S. Balay, J. Brown, K. Buschelman, W. Gropp, D. Kaushik, M. Knepley, L. McInnes, B. Smith & H. Zhang. "PETSc Users Manual". Technical Report March, Argonne National Laboratory (2011).

[9] J. B. Bathe. *Finite Element Procedures*. 2nd edition. Prentice Hall, Upper Saddle River, New Jersey (1996). ISBN 0 13 301458 4.

[10] Z. P. Bažant. "Instability, Ductility, and Size Effect in Strain-Softening Concrete". *Journal of the Engineering Mechanics Division*, 102(2):331–344 (1976).

[11] Z. P. Bažant. "Concrete fracture models: testing and practice". *Engineering Fracture Mechanics*, 69(2):165–205 (2002).

[12] Z. P. Bažant & T.-P. Chang. "Nonlocal Finite Element Analysis of Strain-Softening Solids". *Journal of Engineering Mechanics*, 113(1):89 (1987).

[13] Z. P. Bažant & F. B. Lin. "Non-local yield limit degradation". *International Journal for Numerical Methods in Engineering*, 26(8):1805–1823 (1988).

[14] Z. P. Bažant & B. H. Oh. "Crack band theory for fracture of concrete". *Matériaux et Constructions*, 16(3):155–177 (1983).

[15] T. Belytschko, J. Fish & B. E. Engelmann. "A finite element with embedded localization zones". *Computer Methods in Applied Mechanics and Engineering*, 70(1):59–89 (1988).

[16] T. Belytschko, R. Gracie & G. Ventura. "A review of extended/generalized finite element methods for material modeling". *Modelling and Simulation in Materials Science and Engineering*, 17(4):043001 (2009).

[17] T. Belytschko, Y. Krongauz, D. Organ, M. Fleming & P. Krysl. "Meshless methods: An overview and recent developments". *Computer Methods in Applied Mechanics and Engineering*, 139(1-4):3–47 (1996).

[18] J. Bolander & N. Sukumar. "Irregular lattice model for quasistatic crack propagation". *Physical Review B*, 71(9):094106 (2005).

[19] A. Caballero, C. López & I. Carol. "3D meso-structural analysis of concrete specimens under uniaxial tension". *Computer Methods in Applied Mechanics and Engineering*, 195(52):7182–7195 (2006).

[20] A. Caballero, K. Willam & I. Carol. "Consistent tangent formulation for 3D interface modeling of cracking/fracture in quasi-brittle materials". *Computer Methods in Applied Mechanics and Engineering*, 197(33-40):2804–2822 (2008).

[21] G. Camacho & M. Ortiz. "Computational modelling of impact damage in brittle materials". *International Journal of Solids and Structures*, 33(20-22):2899–2938 (1996).

[22] I. Carol, C. M. Lopez & O. Roa. "Micromechanical analysis of quasi-brittle materials using fracture-based interface elements". *International Journal for Numerical Methods in Engineering*, 52(12):193–215 (2001).

[23] I. Carol, P. C. Prat & C. M. López. "Normal/Shear Cracking Model: Application to Discrete Crack Analysis". *Journal of Engineering Mechanics*, 123(8):765–773 (1997).

[24] H. Cifuentes, M. Alcalde & F. Medina. "Measuring the Size-Independent Fracture Energy of Concrete". *Strain An International Journal for Experimental Mechanics*, 49(1):54–59 (2013).

[25] R. T. Committee. *Interfacial Transition Zone in Concrete: State of the Art Report*. E & FN Spon, London, UK (1996). ISBN 041920010X.

[26] D. Cooper. "Random-sequential-packing simulations in three dimensions for spheres". *Physical Review A*, 38(1):522–524 (1988).

[27] R. de Borst. "Some recent developments in computational modelling of concrete fracture". *International Journal of Fracture*, (1980):5–36 (1997).

[28] R. de Borst. "Fracture in quasi-brittle materials: a review of continuum damage-based approaches". *Engineering Fracture Mechanics*, 69(2):95–112 (2002).

[29] R. de Borst, M. A. Gutiérrez, G. N. Wells, J. J. C. Remmers & H. Askes. "Cohesive-zone models, higher-order continuum theories and reliability methods for computational failure analysis". *International Journal for Numerical Methods in Engineering*, 60(1):289–315 (2004).

[30] R. de Borst, J. J. Remmers & A. Needleman. "Mesh-independent discrete numerical representations of cohesive-zone models". *Engineering Fracture Mechanics*, 73(2):160–177 (2006).

[31] J. Dujc, B. Brank & A. Ibrahimbegovic. "Stress-hybrid quadrilateral finite element with embedded strong discontinuity for failure analysis of plane stress solids". *International Journal for Numerical Methods in Engineering*, 94(12):1075–1098 (2013).

[32] E. N. Dvorkin, A. M. Cuitiño & G. Gioia. "Finite elements with displacement interpolated embedded localization lines insensitive to mesh size and distortions". *International Journal for Numerical Methods in Engineering*, 30(3):541–564 (1990).

[33] M. Elices, G. Guinea, J. Gómez & J. Planas. "The cohesive zone model: advantages, limitations and challenges". *Engineering Fracture Mechanics*, 69(2):137–163 (2002).

[34] G. Fu & W. Dekelbab. "3-D random packing of polydisperse particles and concrete aggregate grading". *Powder Technology*, 133(1-3):147–155 (2003).

[35] T. D. Gerhardt. "A Hybrid/Finite Element Approach for Stress Analysis of Notched Anisotropic Materials". *Journal of Applied Mechanics*, 51(4):804 (1984).

[36] R. E. Goodman, R. Taylor & T. L. Brekke. "A model for the mechanics of jointed rock". *ASCE J. Soil. Mech. Found. Div.*, 94:637–659 (1968).

[37] P. Grassl & C. Pearce. "Mesoscale Approach to Modeling Concrete Subjected to Thermomechanical Loading". *Journal of Engineering Mechanics*, 136(3):322–328 (2010).

[38] V. Hakim & A. Karma. "Laws of crack motion and phase-field models of fracture". *Journal of the Mechanics and Physics of Solids*, 57(2):342–368 (2009).

[39] F. Hashagen & R. de Borst. "An Interface Element for Modeling the Onset and Growth of Mixed-Mode Cracking in Aluminium and Fiber Metal Laminates". *Structural Engineering and Mechanics*, 5(6):817–837 (1997).

[40] H. He, Z. Guo, P. Stroeven, M. Stroeven & L. J. Sluys. "Strategy on Simulation of Arbitrary-Shaped Cement Grains in Concrete". *Image Analysis & Stereology*, 29(2):79–84 (2010).

[41] A. Hillerborg, M. Modeer & P. Petersson. "Analysis of crack formation and crack growth in concrete by means of fracture mechanics and finite elements". *Cement and Concrete Research*, 6(6):773–781 (1976).

[42] H. Huan. *Computational Modelling of Particle Packing in Concrete*. Ph.D. thesis, Delft University of Technology.

[43] L. Iannucci. "Dynamic delamination modelling using interface elements". *Computers & Structures*, 84(15-16):1029–1048 (2006).

[44] A. Ibrahimbegovic & S. Melnyk. "Embedded discontinuity finite element method for modeling of localized failure in heterogeneous materials with structured mesh: an alternative to extended finite element method". *Computational Mechanics*, 40(1):149–155 (2007).

[45] M. Jirásek. "Comparative study on finite elements with embedded discontinuities". *Computer Methods in Applied Mechanics and Engineering*, 188(1-3):307–330 (2000).

[46] M. Jirásek. "Modeling of Localized Inelastic Deformations". In "Short course given at the Czech Technical University", (2010).

[47] M. Jirásek & Z. P. Baz\vant. *Inelastic Analysis of Structures*. 1st editio edition. John Wiley & Sons Ltd, West Sussex, UK (2001). ISBN 0-471-98716-6.

[48] J. Jirousek & L. Guex. "The hybrid-Trefftz finite element model and its application to plate bending". *International Journal for Numerical Methods in Engineering*, 23(4):651–693 (1986).

[49] J. Jirousek & N. Leon. "A powerful finite element for plate bending". *Computer Methods in Applied Mechanics and Engineering*, 12(1):77–96 (1977).

[50] J. Jirousek & M. N'Diaye. "Solution of orthotropic plates based on p-extension of the hybrid-Trefftz finite element model". *Computers & Structures*, 34(1):51–62 (1990).

[51] J. Jirousek & A. Wróblewski. "T-elements: State of the art and future trends". *Archives of Computational Methods in Engineering*, 3(4):323–434 (1996).

[52] L. Kaczmarczyk & C. J. Pearce. "A corotational hybrid-Trefftz stress formulation for modelling cohesive cracks". *Computer Methods in Applied Mechanics and Engineering*, 198(15-16):1298–1310 (2009).

[53] V. Kompis, F. Konol & M. Vasko. "Trefftz-polynomial reciprocity based FEM formulations". *Comp. Assist. Mech. Engrg. Sci.*, 8(2/3):385–398 (2001).

[54] V. Kompiš, M. Toma, M. Žmindák & M. Handrik. "Use of Trefftz functions in nonlinear BEM/FEM". *Computers & Structures*, 82(27):2351–2360 (2004).

[55] S. Kumar & S. V. Barai. *Concrete Fracture Models and Applications*. Springer Berlin Heidelberg, Berlin, Heidelberg (2011). ISBN 978-3-642-16763-8.

[56] J. S. Lee & G. N. Pande. "Application of a homogenisation technique to a one-dimensional bar exhibiting strain-softening behaviour". *Materials and Structures*, 30(8):506–510 (1997).

[57] C. M. López, I. Carol & A. Aguado. "Meso-structural study of concrete fracture using interface elements. I: numerical model and tensile behavior". *Materials and Structures*, 41(3):583–599 (2007).

[58] H. R. Lotfi & P. B. Shing. "Interface Model Applied to Fracture of Masonry Structures". *Journal of Structural Engineering*, 120(1):63–80 (1994).

[59] J. Martin, J. Stanton, N. Mitra & L. N. Lowes. "Experimental Testing to Determine Concrete Fracture Energy Using Simple Laboratory Test Setup". *ACI Materials Journal*, (104):575–584 (2008).

[60] C. Miehe, M. Hofacker & F. Welschinger. "A phase field model for rate-independent crack propagation: Robust algorithmic implementation based on operator splits". *Computer Methods in Applied Mechanics and Engineering*, 199(45-48):2765–2778 (2010).

[61] C. Miehe, F. Welschinger & M. Hofacker. "Thermodynamically consistent phase-field models of fracture : Variational principles and multi-field FE implementations". (March):1273–1311 (2010).

[62] A. Needleman. "A Continuum Model for Void Nucleation by Inclusion Debonding". *Journal of Applied Mechanics*, 54(3):525 (1987).

[63] A. Needleman. "An analysis of decohesion along an imperfect interface". *International Journal of Fracture*, 42(1):21–40 (1990).

[64] D. Ngo & A. Scordelis. "Finite element analysis of reinforced concrete beams". *Journal of American Concrete Institute*, 67:152–163 (1967).

[65] J. Oliver. "Modelling Strong Discontinuities in Solid Mechanics via Strain Softening Constitutive Equations. Part 1: Fundamentals". *International Journal for Numerical Methods in Engineering*, 39(21):3575–3600 (1996).

[66] M. Ortiz, Y. Leroy & A. Needleman. "A finite element method for localized failure analysis". *Computer Methods in Applied Mechanics and Engineering*, 61(2):189–214 (1987).

[67] M. Ortiz & A. Pandolfi. "Finite-deformation irreversible cohesive elements for three-dimensional crack-propagation analysis". *International Journal for Numerical Methods in Engineering*, 44(9):1267–1282 (1999).

[68] A. Pandolfi & M. Ortiz. "Solid modeling aspects of three-dimensional fragmentation". *Engineering with Computers*, 14(4):287–308 (1998).

[69] A. Pandolfi & M. Ortiz. "An Efficient Adaptive Procedure for Three-Dimensional Fragmentation Simulations". *Engineering with Computers*, 18(2):148–159 (2002).

[70] C. J. Pearce, M. Mousavi Nezhad & L. Kaczmarczyk. "A Modelling Framework for Three-Dimensional Brittle Fracture". In "Computational Methods for Engineering Science", pages 193–209 (2012).

[71] T. H. Pian. "Derivation of element stiffness matrices by assumed stress distributions". *AIAA Journal*, 2(7):1333–1336 (1964).

[72] G. Pijaudier-Cabot, Z. P. Bažant & M. Tabbara. "Comparison of various models for strain-softening". *Engineering Computations*, 5(2):141–150 (1988).

[73] R. Piltner. "Special finite elements with holes and internal cracks". *International Journal for Numerical Methods in Engineering*, 21(8):1471–1485 (1985).

[74] R. Piltner. "A quadrilateral hybrid-Trefftz plate bending element for the inclusion of warping based on a three-dimensional plate formulation". *International Journal for Numerical Methods in Engineering*, 33(2):387–408 (1992).

[75] Q. H. Qin & H. Wang. *MATLAB and C Programming for Trefftz Finite Element Methods*. 1st edition edition. Taylor & Francis Group, Florida, USA (2009). ISBN 978-1-4200-7275-4.

[76] Y. Rashid. "Ultimate strength analysis of prestressed concrete pressure vessels". *Nuclear Engineering and Design*, 7(4):334–344 (1968).

[77] J. J. C. Remmers, R. de Borst & A. Needleman. "A cohesive segments method for the simulation of crack growth". *Computational Mechanics*, 31(1-2):69–77 (2003).

[78] J. G. Rots. *Computational Modelling of Concrete Fracture*. Ph.D. thesis, Delft University of Technology (1988).

[79] J. C. J. Schellekens. *Computational Strategies for Composite Structures*. Ph.D. thesis, Delft University of Technology.

[80] J. C. J. Schellekens & R. De Borst. "On the numerical integration of interface elements". *International Journal for Numerical Methods in Engineering*, 36(1):43–66 (1993).

[81] E. Schlangen & J. G. M. Mier. "Simple lattice model for numerical simulation of fracture of concrete materials and structures". *Materials and Structures*, 25(9):534–542 (1992).

[82] K. L. Scrivener. "Backscattered electron imaging of cementitious microstructures: understanding and quantification". *Cement and Concrete Composites*, 26(8):935–945 (2004).

[83] K. L. Scrivener. "Backscattered electron imaging of cementitious microstructures: understanding and quantification". *Cement and Concrete Composites*, 26(8):935–945 (2004).

[84] J. Segurado & J. LLorca. "A new three-dimensional interface finite element to simulate fracture in composites". *International Journal of Solids and Structures*, 41(11-12):2977–2993 (2004).

[85] J. D. Sherwood. "Packing of spheroids in three-dimensional space by random sequential addition". *Journal of Physics A: Mathematical and General*, 30(24):L839–L843 (1997).

[86] B. Sonon, B. François & T. Massart. "A unified level set based methodology for fast generation of complex microstructural multi-phase RVEs". *Computer Methods in Applied Mechanics and Engineering*, 223-224:103–122 (2012).

[87] M. Stroeven & P. Stroeven. "SPACE system for simulation of aggregated matter application to cement hydration". *Cement and Concrete Research*, 29(8):1299–1304 (1999).

[88] M. Suidan & W. C. Scnobrich. "Finite Element Analysis of Reinforced Concrete". *ASCE Journal of the Structural Divison*, 99:2109–2122 (1973).

[89] J. Talbot, P. Schaaf & G. Tarjus. "Random sequential addition of hard spheres". *Molecular Physics*, 72(6):1397–1406 (1991).

[90] T. J. Tautges. "Canonical numbering systems for finite-element codes". *International Journal for Numerical Methods in Biomedical Engineering*, (March 2009):n/a–n/a (2010).

[91] T. J. Tautges, R. Meyers, K. Merkley, C. Stimpson & C. Ernst. "{MOAB:} A Mesh-Oriented Database". Sand2004-1592, Sandia National Laboratories (2004).

[92] J. A. Teixeira de Freitas. "Formulation of elastostatic hybrid-Trefftz stress elements". *Computer Methods in Applied Mechanics and Engineering*, 153(1-2):127–151 (1998).

[93] J. A. Teixeira de Freitas. "Hybrid finite element formulations for elastodynamic analysis in the frequency domain". *International Journal of Solids and Structures*, 36(13):1883–1923 (1999).

[94] J. A. Teixeira de Freitas & C. Cismasiu. "Hybrid-Trefftz displacement element for spectral analysis of bounded and unbounded media". *International Journal of Solids and Structures*, 40:671–699 (2003).

[95] J. A. Teixeira de Freitas, J. P. Moitinho de Almeida & E. M. B. Ribeiro Pereira. "Non-conventional formulations for the finite element method". *Computational Mechanics*, 23(5-6):488–501 (1999).

[96] J. A. Teixeira de Freitas & Z. Wang. "Elastodynamic analysis with hybrid stress finite elements". *Computers & Structures*, 79(19):1753–1767 (2001).

[97] J. A. Teixeira de Freitas & Z. M. Wang. "Elastoplastic dynamic analysis with hybrid stress elements". *International Journal for Numerical Methods in Engineering*, 53(3):515–537 (2002).

[98] E. Trefftz. "Ein Gegenstück zum ritzschen Verfahren." *In: Proc. 2nd Int. Cong. Appl. Mech.*, pages 131–137. (1926).

[99] J. F. Unger, S. Eckardt & C. Könke. "Modelling of cohesive crack growth in concrete structures with the extended finite element method". *Computer Methods in Applied Mechanics and Engineering*, 196(41-44):4087–4100 (2007).

[100] J. Van Mier. "Mode I fracture of concrete: Discontinuous crack growth and crack interface grain bridging". *Cement and Concrete Research*, 21(1):1–15 (1991).

[101] M. R. van Vliet & J. G. van Mier. "Experimental investigation of size effect in concrete and sandstone under uniaxial tension". *Engineering Fracture Mechanics*, 65(2-3):165–188 (2000).

[102] A. Vervuurt. *Interface Fracture in Concrete*. Ph.D. thesis, Delft University of Technology.

[103] K. Willam, I. Rhee & B. Shing. "Interface damage model for thermomechanical degradation of heterogeneous materials". *Computer Methods in Applied Mechanics and Engineering*, 193(30-32):3327–3350 (2004).

[104] S. Williams & a. Philipse. "Random packings of spheres and spherocylinders simulated by mechanical contraction". *Physical Review E*, 67(5):051301 (2003).

[105] A. Winnicki. *Viscoplastic and internal discontinuity models in analysis of structural concrete*. Issn 0860-097x, Krakow University of Technology (2007).

[106] F. Wittmann, H. Mihashi & N. Nomura. "Size effect on fracture energy of concrete". *Engineering Fracture Mechanics*, 35(1-3):107–115 (1990).

[107] X. Xu & A. Needleman. "Numerical simulations of fast crack growth in brittle solids". *Journal of the Mechanics and Physics of Solids*, 42(9):1397–1434 (1994).

[108] J. J. Zheng, C. Q. Li & L. Y. Zhao. "Simulation of Two-Dimensional Aggregate Distribution with Wall Effect". *Journal of Materials in Civil Engineering*, 15(5):506–510 (2003).

[109] O. Zienkiewicz, R. Taylor & J. Zhu. *The Finite Element Method: Its Basis and Fundamentals*, volume 68. 6th edition. Elsevier Butterwith-Heinemann, Oxford (2005). ISBN 0 7506 6320 0.

[110] O. C. Zienkiewicz, D. W. Kelly & P. Bettess. "The coupling of the finite element method and boundary solution procedures". *International Journal for Numerical Methods in Engineering*, 11(2):355–375 (1977).